3-24-2016

Influence of Coolant Flow Rate Parameters in Scaling Gas Turbine Cooling Effectiveness

Connor J. Wiese

INFLUENCE OF COOLANT FLOW RATE PARAMETERS IN SCALING GAS TURBINE COOLING EFFECTIVENESS

THESIS

Connor J. Wiese, Second Lieutenant, USAF

AFIT-ENY-MS-16-M-245

DEPARTMENT OF THE AIR FORCE
AIR UNIVERSITY

AIR FORCE INSTITUTE OF TECHNOLOGY

WRIGHT-PATTERSON AIR FORCE BASE, OHIO

AFIT-ENY-MS-16-M-245

INFLUENCE OF COOLANT FLOW RATE PARAMETERS IN SCALING GAS TURBINE COOLING EFFECTIVENESS

THESIS

Presented to the Faculty

Department of Aeronautics and Astronautics

Graduate School of Engineering and Management

Air Force Institute of Technology

Air University

Air Education and Training Command

In Partial Fulfillment of the Requirements for the

Degree of Master of Science in Aeronautical Engineering

Connor J. Wiese, BS

Second Lieutenant, USAF

March 2016

AFIT-ENY-MS-16-M-245

INFLUENCE OF COOLANT FLOW RATE PARAMETERS IN SCALING GAS TURBINE COOLING EFFECTIVENESS

Connor J. Wiese, BS

Second Lieutenant, USAF

Committee Membership:

Maj James L. Rutledge, PhD, PE

Chair

Dr. Marc D. Polanka

Member

Dr. Richard J. Anthony

Member

Abstract

Film cooling scheme development for use in gas turbine engines often entails the characterization of adiabatic wall temperature distributions in order to determine the driving temperatures for the convective heat transfer processes in the engine. For convenience, adiabatic effectiveness experiments are often performed near room temperature and presumed to scale the engine condition. In order to perform these experiments, researchers elect to match the freestream Reynolds number to that of the engine. When scaling to engine temperatures, however, coolant and freestream fluid properties both change nonlinearly. Therefore the ratio of these properties does not remain constant as the temperature changes. The density ratio change has the greatest effect though dynamic viscosity, specific heats, and thermal conductivities are also temperature dependent. These changes in fluid properties result in an inability to match the freestream and coolant Reynolds numbers, the mass flux ratio, momentum flux ratio, and other parameters simultaneously between laboratory and engine conditions.

The effects of various coolant flow rate parameters and fluid transport property ratios on the adiabatic effectiveness distribution for a simulated leading edge were evaluated using both binary PSP and infrared thermography methods with a low thermal conductivity model at a freestream Reynolds number of 60,000. PSP was used to decouple the mass and momentum transport from the thermal transport in the film cooling process as well as avoid the measurement uncertainties due to conduction into the model. The coolant gases evaluated in this study were air, argon, carbon dioxide, and nitrogen. The test geometry was a semi-cylinder with flat afterbody with a single 90° compound angled cylindrical coolant hole located 21.5° from the stagnation line and

angled 20° to the surface. No single flow rate parameter was found to completely scale the effects of the coolant properties, though momentum flux ratio was found to best scale the shape and location of the adiabatic effectiveness distribution while the advective capacity ratio was found to scale the effectiveness magnitude between coolants at matched momentum flux conditions in thermal experiments. Further, comparison of the thermal and PSP results indicated that the thermal influence of the coolant plume does not necessarily follow the actual placement of the coolant jet on the model surface and is subject to more diffusive processes than the mass transfer analogy would indicate, exposing a potential flaw in the direct application of PSP results to gas turbine heat transfer evaluations.

Acknowledgments

I wish to acknowledge my research advisor Maj James Rutledge for his support throughout the process of completing this thesis project. The willingness to entertain long and often unannounced progress and guidance meetings was greatly appreciated. Further, I would like to thank Dr. Marc Polanka for applying the pressure needed for me to compose the second chapter of this document. I also wish to acknowledge 2d Lt Robert Ashby and 2d Lt Carol Bryant for their assistance in performing experiments and ensuring scientific rigor during the many hours of testing. Finally, I wish to acknowledge Dr. Andy Lethander and Natalia Posada of AFRL/RQTT and Dr. Jim Crafton and Steve Palluconi at Innovative Scientific Solutions Incorporated; without whom this research could not take place.

Connor J. Wiese

Table of Contents

Page

List of Figures

Page

List of Tables

Page

Nomenclature

a	=	initial IR calibration coefficient
A	=	final IR calibration coefficient
ACR	=	advective capacity ratio, $\frac{\rho_c c_{P,c} u_c}{\rho_\infty c_{P,\infty} u_\infty}$
Bi	=	Biot number, $\frac{h_f t_{wall}}{k_{wall}}$
c_P	=	specific heat at constant pressure, (J/kg-K)
c_V	=	specific heat at constant volume, (J/kg-K)
d	=	cooling hole diameter, (m)
D	=	leading edge diameter, (m)
$\mathcal{D}$	=	binary diffusion coefficient, (m^2/s)
DR	=	coolant-to-freestream density ratio, $\frac{\rho_c}{\rho_\infty}$
h	=	transfer coefficient, heat (W/m^2-K), or mass (m/s)
HCR	=	heat capacity ratio, $\frac{\rho_c c_{P,c}}{\rho_\infty c_{P,\infty}}$
i	=	specific enthalpy, J/kg
I	=	momentum flux ratio, $\frac{\rho_c u_c^2}{\rho_\infty u_\infty^2}$
$\mathcal{I}$	=	intensity, (counts)
k	=	thermal conductivity, (W/m-K)
$\mathcal{k}$	=	Boltzmann constant, (J/K)
l	=	arbitrary length scale, (m)
L	=	cooling channel length, (m)
Le	=	Lewis number, $\frac{\mathcal{D}}{\alpha}$ or $\frac{Pr}{Sc}$
M	=	mass flux (blowing) ratio, $\frac{\rho_c u_c}{\rho_\infty u_\infty}$

$\mathcal{M}$	=	molecular weight, (kg/kmol)
n	=	empirical exponent
$NHFR$	=	net heat flux reduction, $1 - \frac{h_f}{h_0}\left(1 - \frac{\eta}{\phi}\right)$
Nu	=	Nusselt number, $\frac{h_f l}{k}$
p	=	partial pressure, (Pa)
P	=	pressure, (Pa)
Pr	=	Prandtl number, $\frac{\mu c_P}{k}$ or $\frac{\nu}{\alpha}$
q''	=	heat flux, (W/m^2)
Re	=	Reynolds number, $\frac{\rho u l}{\mu}$ or $\frac{u l}{\nu}$
ReR	=	coolant-to-freestream Reynolds number ratio, $\frac{\rho_c u_c \mu_\infty}{\rho_\infty u_\infty \mu_c}$
S	=	entropy, (J)
Sc	=	Schmidt number, $\frac{\mu}{\rho \mathcal{D}}$ or $\frac{\nu}{\mathcal{D}}$
Sh	=	Sherwood number, $\frac{h_M l}{\mathcal{D}}$
t	=	thickness, (m)
$\cancel{t}$	=	time since experiment initialization, (s)
T	=	temperature, (K)
$\bar{T}$	=	mean temperature of T_∞ and T_c
T_{t_4}	=	combustor exit temperature
Tu	=	freestream turbulence intensity
u	=	velocity, (m/s)
VR	=	velocity ratio, $\frac{u_c}{u_\infty}$

x	=	first ordinate, (m)
$\mathcal{X}$	=	mole fraction
y	=	second ordinate, (m)
$\mathcal{Y}$	=	mass fraction
z	=	third ordinate, (m)
α	=	thermal diffusivity, $\frac{k}{\rho c_P}$, (m^2/s)
β	=	angle between coolant hole and stagnation line, (°)
γ	=	angle between coolant hole axis and model surface, (°)
δ	=	Kronecker delta function
δT	=	difference between T_{wall} and T_{est}, (K)
ΔT	=	energy separation temperature difference
ϵ	=	Lennard-Jones attractive energy, (J)
ε	=	measurement uncertainty
ζ	=	arbitrary function of measured quantities
η	=	adiabatic effectiveness, $\frac{T_\infty - T_{aw}}{T_\infty - T_c}$
$\bar{\eta}$	=	spanwise-averaged adiabatic effectiveness
Λ	=	turbulence length scale, (m)
μ	=	dynamic (absolute) viscosity, (Pa-s)
ν	=	kinematic viscosity, $\frac{\mu}{\rho}$, (m^2-s)
ξ	=	arbitrary measured quantity
π_c	=	compressor pressure ratio

ρ	=	density, (kg/m^3)
σ	=	Lennard-Jones collision diameter, (Å)
τ	=	viscous stress tensor, (Pa)
ϕ	=	overall effectiveness, $\frac{T_\infty - T_s}{T_\infty - T_{c,i}}$
χ	=	coolant warming factor, $\frac{T_\infty - T_{c,e}}{T_\infty - T_{c,i}}$
Ω	=	dimensionless collision integral

Subscripts

A	=	property of chemical species A
AB	=	property of chemical species A and B combined
air	=	experiment with air or in air
amb	=	ambient condition
app	=	apparent
aw	=	adiabatic wall
B	=	property of chemical species B
c	=	coolant
$cond$	=	conduction
D	=	with respect to the leading edge diameter
$\mathcal{D}$	=	for determination of binary diffusion coefficients
e	=	coolant hole exit plane
exp	=	experimental condition

est	=	estimate
f	=	with film cooling
FG	=	with foreign gas injection, or property of the foreign gas
i	=	coolant system entrance, model interior, or arbitrary index
IR	=	infrared camera output temperature
j	=	arbitrary index
k	=	arbitrary index, of thermal conductivity
lab	=	laboratory reference frame
M	=	mass transfer coefficient
max	=	maximum
min	=	minimum
N_2	=	of nitrogen
O_2	=	of oxygen
rad	=	radiation
$reported$	=	reported adiabatic effectiveness
ref	=	reference condition
s	=	at the surface
T	=	tracer species or total
$wall$	=	property of model or wind tunnel wall
x	=	arbitrary location
ζ	=	of an arbitrary function of measured quantities

η	=	of adiabatic effectiveness
λ	=	arbitrary chemical species index
μ	=	of the kinematic viscosity
ξ	=	of an arbitrary measured quantity
ρ	=	of the density
0	=	initial/reference condition, derivative with respect to time
1	=	first time condition
2	=	second time condition
∞	=	freestream

Acronyms

IR	=	infrared thermography
PSP	=	pressure sensitive paint
SLPM	=	Standard Liters Per Minute

INFLUENCE OF COOLANT FLOW RATE PARAMETERS IN SCALING GAS TURBINE COOLING EFFECTIVENESS

1. Introduction

Since their development, gas turbine engines have been essential to the United States Air Force, both as propulsion systems for aircraft and as ground based power generation solutions. Gas turbine engines utilize the Brayton thermodynamic cycle, as demonstrated in the temperature-entropy (T-S) diagram in Fig. 1.1. The Brayton cycle consists of a compression stage to pressurize the incoming air (1), a combustion stage to increase the thermal energy of the air (2), work is then extracted by the turbine to run the compressor (3), and any residual energy is either used for thrust by expelling the hot exhaust gases out of a nozzle, or for further work from another turbine (4). This extracted work is often used to drive a shaft in turboshaft engines or for turning a generator in the case of ground based power applications.

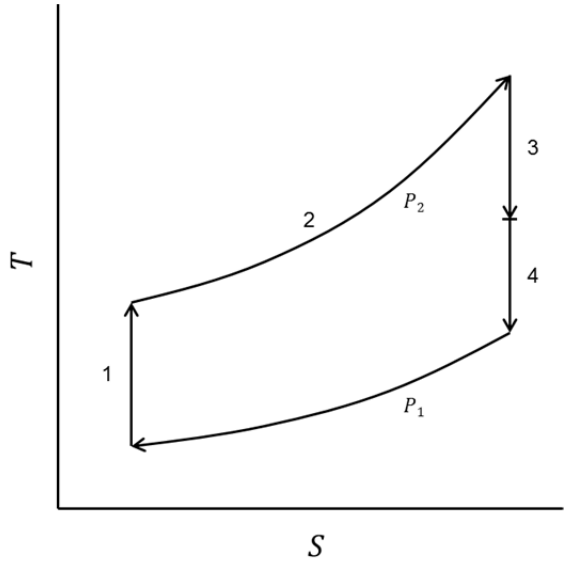

Figure 1.1. Idealized temperature-entropy diagram for a Brayton cycle engine.

A research focus since the initial development of gas turbine engines has been increasing their performance capabilities. The two methods for increasing engine performance are increasing the compressor pressure ratio, π_c, and increasing the combustor exit temperature, T_{t_4}, though increasing π_c will often result in increased T_{t_4}. Increasing π_c is linked to both the engine's specific power and its fuel efficiency. Increasing T_{t_4} is linked to the engine's specific power. Increases in T_{t_4} require enhanced turbine blade cooling schemes, since the hot gases from the combustor are often at higher temperatures than the melting temperatures of turbine blades and vanes. For this reason, the blades and vanes are cooled by relatively cool air from the compressor, both through channels cut through the interiors of the blades and by external film cooling. External film cooling is the process by which a relatively cool layer of air is ejected from the surface of the blade, into the boundary layer. This layer of air insulates the blade from the high temperature freestream gas.

There are two primary means for evaluating film cooling schemes. One is at engine conditions: high temperature, high flow velocity, and small scale hardware. While this type of setup is ideal for simulating the engine conditions, these conditions are not easily replicated in a laboratory setting, especially when minor details require fine control. As such, film cooling configurations are often performed at room temperature, with low flow velocities and large scale hardware. As a result, film cooling experiments at these conditions are easier to perform. However, some of the flow physics are lost at these scales. For example, reacting coolant flows are not possible at these conditions. Likewise, the variation in fluid properties between the coolant and freestream is not possible to fully replicate at low temperature testing conditions.

In order to make use of the results obtained at the low temperature conditions in future gas turbine film cooling schemes, the results must be scaled to the engine conditions. While

some of characteristics of the flow, in particular freestream Reynolds number, are fairly simple to match, each individual flow parameter cannot be matched between the low and high temperature test conditions simultaneously [1]. This is the case because the ratios between the coolant and freestream fluid properties are heavily reliant on temperature (and to a degree, pressure). The most commonly considered property ratio by experimentalists is the density ratio, as the gases present in a high-pressure turbine are at approximately the same pressure, but vary widely in temperature, resulting in elevated density ratios. Experimentalists achieve elevated density ratios by heating the freestream fluid, cooling the coolant gas, or using a foreign gas altogether. Each of these techniques, however, has its shortcomings. Using a foreign gas as a coolant, for example, changes the temperature dependency of the other fluid properties, such as the thermal conductivity, dynamic viscosity, and the specific heats of the coolant, changing the cooling jet dynamics and heat transfer properties.

In order to overcome these fluid property discrepancies, researchers often attempt to match particular coolant flow rate parameters between various coolants. However, there is disagreement as to which parameter to use. As a result, the first objective of this research was to determine the influence of traditional and non-traditional coolant flow rate parameters as they pertain to scaling adiabatic effectiveness results between various selected cooling gases on a simulated leading edge.

Recently, researchers have been evaluating film cooling schemes using pressure sensitive paints (PSP) and applying the heat-mass transfer analogy. This method is attractive because thermal methods used to determine adiabatic effectiveness distributions at steady state are influenced by conductive heat transfer into the test surface. However, by using these mass transfer methods, some details, such as the thermal interactions between the coolant jet and

freestream, are lost. As a result, the second objective of this work was to determine whether PSP methods are valid replacements for thermal methods in determining adiabatic effectiveness measurements and what, if any, differences result.

These objectives were accomplished by selectively matching various coolant flow rate parameters with a selection of cooling gases. Furthermore, these coolant flow rate parameters and gases were evaluated using both PSP and IR thermography at the same coolant and freestream conditions to provide method comparison conditions.

2. Literature Review

There are two primary methods by which turbine airfoil temperatures are controlled: internal cooling, where relatively cool gas is cycled through channels inside of the airfoil; and external film cooling, where the cooling gas is injected into the boundary layer of the airfoil. The present work is focused on the latter, in particular, scaling the results of low temperature experiments to the high temperature engine conditions.

2.1 General Principles

Bogard and Thole [2] provide a general summary of the film cooling process and driving parameters. Film cooling reduces the heat transfer to a turbine airfoil by decreasing the driving potential for heat transfer. This is accomplished by reducing the temperature of the gas near the surface of the blade. The reduction of the gas temperature reduces the heat transfer since heat is conducted into the surface from the gas. This process is characterized by Newton's Law of Cooling:

$$h_f = \frac{q_f''}{T_{aw} - T_s} \tag{2.1}$$

where the q_f'' and h_f represent the heat flux and the heat transfer coefficient with film cooling, respectively, T_s is the component surface temperature, and T_{aw} is the adiabatic wall temperature, or the temperature of the gas near the airfoil surface, should that surface be adiabatic. Using T_{aw} as the reference temperature for film cooling allows for the approximately linear form for convective heat flux shown in Eq. (2.1).

The ability for a given cooling scheme to decrease T_{aw} is often characterized by experimentalists as the nondimensional adiabatic effectiveness, η:

$$\eta = \frac{T_\infty - T_{aw}}{T_\infty - T_{c,e}} \tag{2.2}$$

where $T_{c,e}$ is the temperature of the coolant as it exits the cooling hole. Nondimensionalization of the adiabatic wall temperature allows for translation to the engine conditions, provided the other flow physics are scaled properly. This parameter, however, is not easily translatable to the engine conditions due to the influence of flow properties that are dependent on absolute temperatures, such as the coolant and freestream specific heats and thermal conductivities.

In addition to the adiabatic effectiveness, the overall effectiveness, defined in Eq. (2.3), relates the airfoil surface temperature to the temperature of the coolant as it enters the internal cooling channels, $T_{c,i}$ [2].

$$\phi = \frac{T_\infty - T_s}{T_\infty - T_{c,i}} \tag{2.3}$$

A third nondimensional parameter that is important to film cooling is the net heat flux reduction [2, 3]:

$$NHFR = 1 - \frac{q_f''}{q_0''} = 1 - \frac{h_f}{h_0}\left(\frac{T_{aw} - T_s}{T_\infty - T_s}\right) = 1 - \frac{h_f}{h_0}\left(1 - \frac{\eta}{\phi}\right) \tag{2.4}$$

$NHFR$, however, does not describe a physical phenomenon inside of an engine, but rather, describes the internal heat load reduction that would be achieved by adding a film cooling feature, keeping the same wall temperature. In reality, should the heat flux be reduced at a location, the wall temperature at that same location would also decrease. The ratio h_f/h_0 represents the ratio between the local heat transfer coefficients when the cooling feature is added to the airfoil surface and before the feature was added to the surface. Often, this ratio is greater than unity. This is due to the increased turbulent boundary layer mixing introduced by a film cooling jet [4]. This increase in the local heat transfer coefficient is often offset by a decrease in

the local adiabatic wall temperature. As a result, $NHFR$ is often positive, though near certain flow structures can be negative [3].

2.2 Experimental Methods

Film cooling experimentation often evaluates a given cooling scheme in terms of the adiabatic effectiveness and the heat transfer coefficient distribution. Furthermore, these two aspects of a given cooling scheme can be evaluated using either thermal or heat-mass transfer analogy methods.

2.2.1 Steady Thermal Method

The steady state thermal method for determining η is described by Baldauf et al. [5], wherein an IR camera or other thermal measurement system is used to determine the surface temperature distribution. If the wall is adiabatic, the η distribution can then be obtained by nondimensionalizing the wall temperature with the freestream and coolant temperatures as in Eq. (2.2). The complexities of this method result from the fact that no material is adiabatic, resulting in errors due to heat transfer to the model surface, so that η must actually be defined with a consideration for conduction as shown in Eq. (2.5) [6]. In order to reduce the uncertainty in η measurements due to estimating q_f'' and h_f, low thermal conductivity models are selected so as to reduce the magnitude of the heat flux into the surface. Furthermore, surface heat transfer occurs due to radiation as the model and the surrounding surfaces are not necessarily the same temperature, though near room temperature, this heat flux is small. Baldauf accounts for the conduction into the model using a finite element analysis of the heat transfer and thermocouples embedded into the model, though simple one-dimensional conduction corrections are often applied [7]. Other steady-state experiments simply utilized thermocouples placed on the surface, though the surface temperature resolution is degraded compared to the measurements taken with

an IR camera [8]. Furthermore, this methodology can be applied to conducting models for ϕ measurements, though without the corrections for conduction into the surface.

$$\eta = \frac{T_\infty - T_s}{T_\infty - T_c} - \frac{q_f''}{h_f(T_\infty - T_c)} \tag{2.5}$$

Rutledge et al. [6] describes a steady method for determining the heat transfer coefficient, h_f. An electrical heater provides a known heat flux, with arbitrarily set coolant and freestream temperatures. With a known η distribution, h_f is determined using Eq. (2.6)—which is Eq. (2.1) written in terms of η—where the q_f'' term is the heat flux from the surface due to convection, determined using Eq. (2.7). The q_T'' term in Eq. (2.7) represents the heat flux that is supplied by the electrical heater, q_{cond}'' is the heat flux into the model surface, and q_{rad}'' is the heat flux to the surrounding surfaces due to radiation. The major sources of uncertainty in this method are the η distribution, the heat flux due to conduction into the model, and the heat flux due to radiation to surrounding surfaces, since the heat fluxes are estimated by correlations. The uncertainty due to the η distribution, however, can be reduced if the freestream and coolant temperatures are matched. This methodology, along with steady state η and ϕ measurements and an uncooled experiment to determine h_0, provides the necessary measurements to determine $NHFR$ for a given cooling scheme using Eq. (2.4).

$$h_f = -\frac{q_f''}{\eta(T_\infty - T_c) + T_s - T_\infty} \tag{2.6}$$

$$q_f'' = q_T'' - q_{cond}'' - q_{rad}'' \tag{2.7}$$

2.2.2 Transient Thermal Method

The transient thermal method is described by Ekkad et al. [9] and Ekkad et al. [10]. Reference 9 utilized the transient liquid crystals on a film cooled, heated cylinder in crossflow,

while Ref. 10 utilized infrared thermography for surface temperature measurements. From the transient method, both T_{aw} and h_f distributions can be determined. The transient thermal method relies on a uniform temperature, semi-infinite model that is exposed to a step change in free stream temperature. The surface temperature distribution is then determined at two times, t, after the step change is applied. The T_{aw} and h_f distributions are determined by simultaneous evaluation of Eqs. (2.8) and (2.9). T_{aw} can then be nondimensionalized to η using Eq. (2.2). An advantage to using infrared thermography in the transient method is that T_{aw} and h_f can be evaluated with a single experiment while the liquid crystal temperature measurements require two separate experiments to determine T_{aw} and h_f. Two experiments are necessary with liquid crystals because the crystals change color at a specified temperature rather than expressly measuring the surface temperature. Therefore, the time to reach a specific temperature is measured rather than the surface temperature at a particular time. A further advantage to infrared measurements is that multiple evaluations of T_{aw} and h_f can be made, allowing for a least-squares curve fit to be applied, leading to more accurate results.

$$\frac{T_{s,1}-T_0}{T_{aw}-T_0} = 1 - \exp\left(\frac{h_f^2 \alpha_{wall} t_1}{k_{wall}^2}\right) \operatorname{erfc}\left(\frac{h_f \sqrt{\alpha_{wall} t_1}}{k_{wall}}\right) \tag{2.8}$$

$$\frac{T_{s,2}-T_0}{T_{aw}-T_0} = 1 - \exp\left(\frac{h_f^2 \alpha_{wall} t_2}{k_{wall}^2}\right) \operatorname{erfc}\left(\frac{h_f \sqrt{\alpha_{wall} t_2}}{k_{wall}}\right) \tag{2.9}$$

2.2.3 Mass Transfer Methods

In addition to the thermal techniques, several mass-transfer methodologies have been developed for film cooling analysis. These methods are attractive because common boundary conditions, such as constant temperature/adiabatic walls can be exactly simulated without errors resulting from conductive and radiative heat losses. Two different methods are employed to achieve the two boundary conditions. The constant temperature wall condition is achieved using

an evaporation-sublimation technique and is applied to situations where h_f distributions are to be determined while the adiabatic wall condition is simulated using a mass injection technique in experiments where η distributions are determined.

Two evaporation-sublimation techniques are described in Goldstein and Cho [11] and Ammari et al. [12], where h_f was determined using the heat-mass transfer analogy. The constant temperature wall condition was simulated with a constant mass fraction wall. Goldstein and Cho utilized the naphthalene sublimation technique wherein a model is coated with a thin layer of naphthalene. The mass transfer coefficient distribution during the experiment is determined by measuring the change in layer thickness, usually using a laser measurement. Additionally, the area averaged mass transfer coefficient is determined by measuring the change in mass of the model during the experiment. Conceptually, the swollen polymer technique described by Ammari et al. is similar to the naphthalene sublimation technique. For this method, the model is coated with a thin layer of silicone rubber that is swollen with a liquid. Like the naphthalene sublimation technique, the local mass transfer coefficients are determined from the change in the layer thickness. Though not mentioned in Ref. 12, the weighing method described in Ref. 11 could likely be applied to the swollen polymer technique as well to obtain average transfer coefficients.

Basic mass injection techniques are described in Pedersen et al. [13]. For these experiments, a tracer species, either in the freestream or the coolant jet, is utilized to determine the coolant distribution in the flow field. The adiabatic effectiveness is then determined using Eq. (2.10), where $\mathcal{Y}_T$ refers to the mass fraction of the tracer species, and the subscripts ∞, s, and c refer to the quantities located in the freestream, at the model surface, and in the coolant respectively. The mass fraction of the tracer gas is determined either at discrete locations with

sampling taps or with a pressure sensitive paint (PSP) technique for full field measurements. The PSP method for film cooling experiments is described by Li et al. [14].

$$\eta = \frac{y_{T,\infty} - y_{T,s}}{y_{T,\infty} - y_{T,c}} \tag{2.10}$$

Before describing the application of the PSP methodology itself, a brief overview of how PSP operates is in order. There are two main formulations for PSPs—single component and binary PSP. As their names suggest, single component PSP contains only one luminescent particle, while the binary formulation contains two. The paint structures are shown in Fig. 2.1. For both paint formulations, the measured pressure is a function of the ratio of the measured intensities of emitted radiation for a reference and experimental case, $\mathcal{I}_{ref}/\mathcal{I}_{exp}$, which is a result of a change in the local partial pressure of O_2 at the surface, due to an oxygen quenching process as described by Narzary et al. [15]. This oxygen quenching process only occurs with the sensitive molecule (red in Fig. 2.1). Emission intensity for the sensitive molecule, however, is also a function of temperature. This sensitivity presents a complication when attempting to conduct film cooling experiments where the freestream and coolant temperatures are not matched. The reference molecule (green in Fig. 2.1b) is a pressure-insensitive temperature-sensitive molecule, used to correct for the temperature sensitivity of the sensitive molecule [16]. Using this second molecule, the local partial pressure ratio, $P_{O_2,exp}/P_{O_2,ref}$, is correlated with the intensity ratios, $\mathcal{I}_{ref}/\mathcal{I}_{exp}$, for both the sensitive and reference channels.

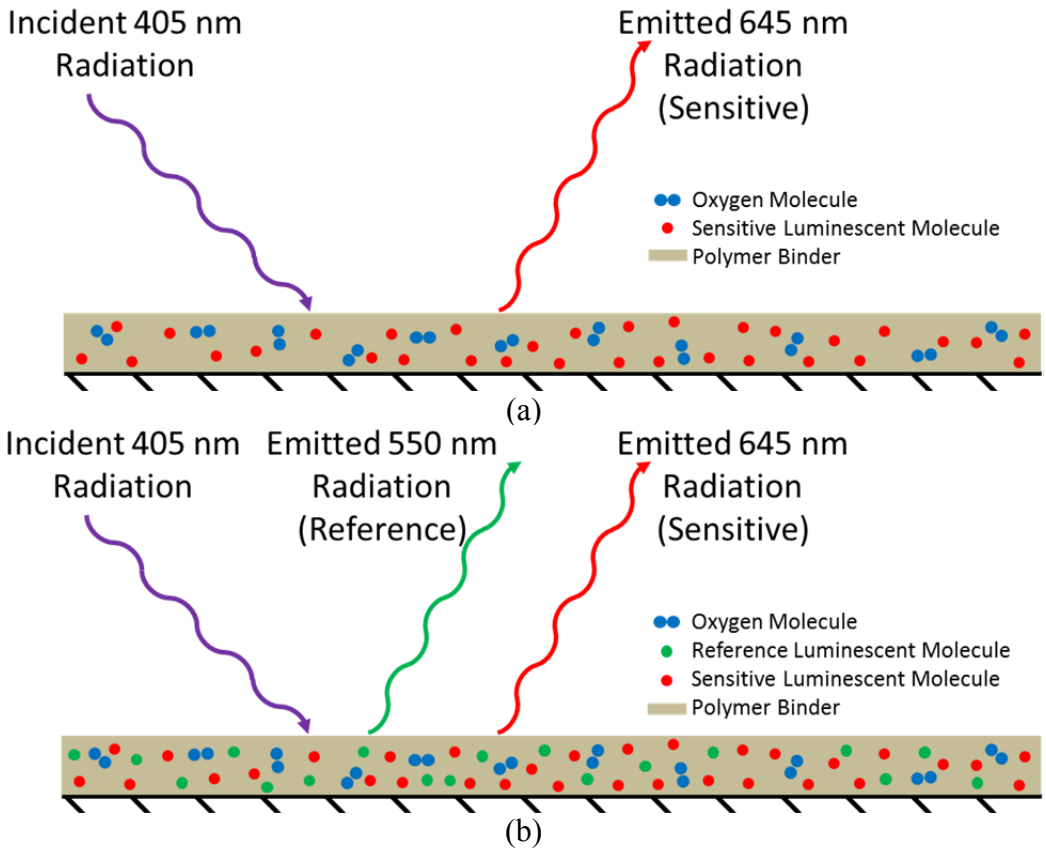

Figure 2.1. PSP composition for single component (a) and binary (b) PSP.

Regardless of whether a binary or single component PSP is used, the partial pressure of O_2 distribution is obtained on the surface of the test article. Since O_2 is displaced from the coolant plume in an anaerobic cooling jet, O_2 can be used as the tracer gas for film cooling experiments. However, Eq. (2.10) cannot be applied directly since PSP does not directly measure the mass fraction of O_2 at the surface. As a result, an expression for the adiabatic effectiveness must be derived in terms of the local partial pressure of O_2. The expression for mass fraction of O_2 in terms of the mole fraction of O_2 at an arbitrary location in the flow field is shown in Eq. (2.11), where $\mathcal{X}_{O_2,x}$ is the mole fraction of O_2 at that location, $\mathcal{M}_{O_2}$ is the molecular weight of O_2, and $\mathcal{M}_x$ is the molecular weight of fluid at that location. Substitution of Eq. (2.11) into Eq.

(2.10) yields Eq. (2.12). However, since the cooling gases are anaerobic, $\mathcal{X}_{O_2,c} = 0$, simplifying Eq. (2.12) to the form shown in Eq. (2.13).

$$\mathcal{Y}_{O_2,x} = \frac{\mathcal{X}_{O_2,x}\,\mathcal{M}_{O_2}}{\mathcal{M}_x} \tag{2.11}$$

$$\eta = \frac{\dfrac{\mathcal{X}_{O_2,\infty}\,\mathcal{M}_{O_2}}{\mathcal{M}_\infty} - \dfrac{\mathcal{X}_{O_2,s}\,\mathcal{M}_{O_2}}{\mathcal{M}_s}}{\dfrac{\mathcal{X}_{O_2,\infty}\,\mathcal{M}_{O_2}}{\mathcal{M}_\infty} - \dfrac{\mathcal{X}_{O_2,c}\,\mathcal{M}_{O_2}}{\mathcal{M}_c}} \tag{2.12}$$

$$\eta = 1 - \frac{\mathcal{X}_{O_2,s}\,\mathcal{M}_\infty}{\mathcal{X}_{O_2,\infty}\,\mathcal{M}_s} \tag{2.13}$$

Next, the molecular weight of the gas mixture at the surface, $\mathcal{M}_s$, must be taken into account. For simplicity, the gas mixture at the surface is considered a binary mixture of air and the selected coolant gas—recognizing that air, itself, is a binary mixture of O_2 and N_2. The molecular weight of the gas at the surface is given by the expression in Eq. (2.14). However, since air is composed of N_2 and O_2 in fixed amounts, substitution of Eqs. (2.15) and (2.16) into Eq. (2.14) yields a form of the surface fluid molecular weight in terms of the mole fraction of O_2 at the surface alone, shown in Eq. (2.17)—since all other values are fixed for a given experiment.

$$\mathcal{M}_s = \mathcal{X}_{air,s}\,\mathcal{M}_{air} + \mathcal{X}_{c,s}\,\mathcal{M}_c \tag{2.14}$$

$$\mathcal{X}_{air,s} = \mathcal{X}_{O_2,s}\left(1 + \frac{\mathcal{X}_{N_2,air}}{\mathcal{X}_{O_2,air}}\right) \tag{2.15}$$

$$\mathcal{X}_{c,s} = 1 - \mathcal{X}_{air,s} = 1 - \mathcal{X}_{O_2,s}\left(1 + \frac{\mathcal{X}_{N_2,air}}{\mathcal{X}_{O_2,air}}\right) \tag{2.16}$$

$$\mathcal{M}_s = \mathcal{X}_{O_2,s}\left(1 + \frac{\mathcal{X}_{N_2,air}}{\mathcal{X}_{O_2,air}}\right)\mathcal{M}_{air} + \left[1 - \mathcal{X}_{O_2,s}\left(1 + \frac{\mathcal{X}_{N_2,air}}{\mathcal{X}_{O_2,air}}\right)\right]\mathcal{M}_c \tag{2.17}$$

Substitution of Eq. (2.17) into Eq. (2.13) yields the expression shown in Eq. (2.18), where the adiabatic effectiveness is a function of the surface mole fraction of O_2 and experimental parameters. Using the expression in Eq. (2.19), Eq. (2.18) simplifies to the form

shown in Eq. (2.20). Utilizing Dalton's Law of Partial Pressures, $\mathcal{X}_{O_2,s}$ is determined using Eq. (2.21), where $p_{O_2,s}$ is the partial pressure of O_2 at the surface and P_s is the surface pressure. Recognizing that the product of $\mathcal{X}_{O_2,air}$ and P_s is the partial pressure of O_2 for a case wherein air is injected in place of the anaerobic coolant, the adiabatic effectiveness expression becomes that of Eq. (2.22), where the air and c subscripts on the partial pressure terms indicate data obtained during air blowing and anaerobic gas blowing cases, respectively. The form of η shown in Eq. (2.22) is equivalent to the form shown in Li et al [14].

$$\eta = 1 - \frac{\mathcal{X}_{O_2,s}\,\mathcal{M}_{air}}{\mathcal{X}_{O_2,air}\left\{\mathcal{X}_{O_2,s}\left(1+\frac{\mathcal{X}_{N_2,air}}{\mathcal{X}_{O_2,air}}\right)\mathcal{M}_{air} + \left[1-\mathcal{X}_{O_2,s}\left(1+\frac{\mathcal{X}_{N_2,air}}{\mathcal{X}_{O_2,air}}\right)\right]\mathcal{M}_c\right\}} \tag{2.18}$$

$$\mathcal{X}_{O_2,air}\left(1+\frac{\mathcal{X}_{N_2,air}}{\mathcal{X}_{O_2,air}}\right) = 1 \tag{2.19}$$

$$\eta = 1 - \frac{1}{1-\left(1-\frac{\mathcal{X}_{O_2,air}}{\mathcal{X}_{O_2,s}}\right)\frac{\mathcal{M}_c}{\mathcal{M}_{air}}} \tag{2.20}$$

$$\mathcal{X}_{O_2,s} = \frac{p_{O_2,s}}{P_s} \tag{2.21}$$

$$\eta = 1 - \frac{1}{1-\left(1-\frac{\left(p_{O_2,s}\right)_{air}}{\left(p_{O_2,s}\right)_c}\right)\frac{\mathcal{M}_c}{\mathcal{M}_{air}}} \tag{2.22}$$

2.3 Scaling

The prediction of a given cooling scheme's effectiveness is influenced by many factors, of which many are coupled. Among these factors are the turbine geometry, cooling scheme location, and coolant flow dynamics. The coolant flow dynamics are heavily temperature dependent, as the freestream gas temperatures entering the turbine are much larger than the coolant temperatures, often by a factor of two [2], resulting in potentially large differences

between the coolant and freestream fluid properties. Often, experimentalists attempt to scale their results with matched freestream Reynolds numbers and with properly scaled geometries while varying the density ratio, DR, between the coolant and the freestream:

$$DR = \frac{\rho_c}{\rho_\infty} \tag{2.23}$$

Accounting for DR effects is often done through the use of various flow rate parameters, in particular: the mass flux, or blowing, ratio, M; momentum flux ratio, I; and the velocity ratio, VR.

$$M = \frac{\rho_c u_c}{\rho_\infty u_\infty} \tag{2.24}$$

$$I = \frac{\rho_c u_c^2}{\rho_\infty u_\infty^2} \tag{2.25}$$

$$VR = \frac{u_c}{u_\infty} \tag{2.26}$$

Each of these flow rate parameters describe a different portion of the flow physics present in the cooling scheme. The blowing ratio partially represents the ability of the coolant to transport energy, since energy transport is linked to $\rho_c u_c c_{P,c}$. The reader should note, however, that the specific heats are missing from Eq. (2.24). In order to account for the energy transport capacity of the coolant, Rutledge and Polanka [17] introduced the flow rate parameter defined in Eq. (2.27) as the heat capacity ratio. However, the current work defines this parameter as the advective capacity ratio to avoid confusion with the coolant to freestream heat capacity ratio, defined in Eq. (2.28).

$$ACR = \frac{\rho_c c_{P,c}\, u_c}{\rho_\infty c_{P,\infty}\, u_\infty} \tag{2.27}$$

$$HCR = \frac{\rho_c c_{P,c}}{\rho_\infty c_{P,\infty}} \tag{2.28}$$

The momentum flux ratio describes the dynamics of the jet-freestream interaction, particularly how the jet is turned by the freestream as it exits the coolant hole. Finally, VR scales the shear layers between the jet and freestream, scaling the turbulent consequences of the jet, however, for shear dynamics to be properly accounted for, the viscosities of the coolant and freestream fluids should be taken into account. Additionally, the reader should note that without a matched DR, the blowing ratio, momentum flux ratio, and velocity ratio cannot be matched simultaneously.

Pietrzyk et al. [4] characterized the effects of DR on the hydrodynamics of cooling flow out of streamwise angled cylindrical holes, to include velocity and turbulence profiles. They examined DR = 1.0 and 2.0 at M = 0.25 and 0.5 for unit DR coolant and M = 0.5 for DR = 2.0 coolant. The DR = 2.0 coolant was found to produce similar velocity profiles near the hole exit at M = 0.5 when compared to the unit DR jet at M = 0.25, though this result was expected because VR = 0.25 for both DR conditions. However, the penetration of the high density jet into the freestream was greater than that of the unit DR jet at these conditions, as the dense jet carried more momentum than the unit density jet at M = 0.25. When compared to the unit density jet where M = 0.5, however, the dense jet was found to penetrate the freestream less effectively, tying I to jet penetration of the freestream, since I = 0.125 for the dense jet at M = 0.5 and 0.062 and 0.25 for the M = 0.25 and 0.5 unit DR jets, respectively. In addition, the dense jet was found to resist the entrainment of freestream fluid better than that of the unit DR jets. Furthermore, it was found that dense jets produce elevated turbulence levels near the hole exit than less dense jets when VR was matched, though the unit DR jet at M = 0.5 produced greater turbulence at the coolant hole exit. Turbulent shear stresses were found to be connected to VR in the near-hole

region. In the far field, however, the dense jet's turbulence characteristics persisted farther downstream than either unit DR case.

Thole et al. [18] investigated the effects of DR on the thermal fields in the flow field produced by cooling jets in crossflow. The elevated DR was achieved by chilling the coolant with a liquid nitrogen heat exchanger, allowing for experimental density ratios of DR = 1.2, 1.6, and 2.0. The separation and reattachment characteristics of the coolant jets were found to scale with I, rather than M or VR. Additionally, the nondimensionalized temperature profiles were also found to be similar across DR when I was matched. In particular, the thermal profiles near the coolant hole exit was found to scale with I, despite Ref. 4, to which Thole et al. was a complement, showing that the velocity field near the hole scaled with VR.

Sinha et al. [8] explored the effects of DR on the cooling effectiveness downstream of a row of cooling holes on a flat plate. Like Ref. 18, this study achieved variable density ratios with liquid nitrogen heat exchangers, and the coolant was ejected from a row of streamwise, cylindrical coolant holes at various M, I, and VR, at DR of 1.2, 1.6, and 2.0. The three density ratios were evaluated at matched M, VR, and I conditions. They determined that the proper parameter for scaling DR was dependent on the flow dynamics. For well attached coolant jets, the centerline effectiveness was found to scale with M, while jet separation and reattachment was found to scale with I. In addition, at fixed points downstream of the cooling hole, elevated DR coolants were found to produce better effectiveness at all I conditions than the DR = 1.2 coolant. Laterally averaged effectiveness was found to increase with DR, connected to the lateral spreading of the coolant jets. It was found that the jet spreading was dependent on I, with higher I values resulting in decreased jet spreading.

Ammari et al. [12] examined the influence of coolant density ratio on the local heat transfer coefficient using the swollen polymer mass-transfer analogy technique. With inclined, streamwise injection, lower density coolants were found to have elevated heat transfer coefficients at matched M conditions. This finding was attributed to the lower density jets having a higher I than the heavier jets, increasing the mixing around the jet, thus increasing the heat transfer coefficient. Like many other studies, the researchers reported the achieved I values, but did not attempt to isolate and match I further.

Baldauf et al. [5] performed film cooling experiments at elevated freestream temperatures (550 K) to produce engine representative DR, and ejected the coolant through streamwise, cylindrical coolant holes at various M and coolant ejection angles. They found that as DR decreased, the optimal M decreased, as well as a uniform decrease in η at matched M as DR decreased. This decrease was attributed to the tendency of the less dense jets to lift off of the surface behind the cooling hole exit, due to higher jet momentum. Though I was recorded, no test cases were performed when I was matched in this study.

Ekkad et al. [9] investigated the effects of DR and freestream turbulence intensity on local heat transfer coefficient distributions and η distributions for coolants ejected from compound-angled holes on a simulated leading edge. The heat transfer coefficient and η distributions were determined using the transient thermal technique. The variable DR was achieved by using air and CO_2 as the coolants for the unit and DR = 1.5 cases, respectively. They found that the optimal blowing ratio for air was M = 0.4, whereas M = 0.8 was found to be optimal for CO_2 injection. In addition, freestream turbulence was found to degrade the film effectiveness and increase the local heat transfer for both coolants, though the higher blowing (and thus higher momentum) jets were found to resist the effects of the turbulent freestream

better than the lower blowing jets. Furthermore, higher density jets were found to increase the heat transfer to the surface at all blowing ratios.

Pedersen et al. [13] characterized the effects of DR on η using the heat-mass transfer analogy. They found that for discrete cooling holes, spanwise averaged effectiveness monotonically increased with DR at matched M conditions, up to the point of cooling jet liftoff from the surface. Furthermore, the centerline effectiveness was found to increase with increasing I for a matched M condition. This seems counterintuitive, since for matched M, the momentum flux increases with decreasing DR, but the laterally averaged effectiveness was found to be influenced by coolant spreading rate. As a result, the higher I jets maintained a thinner, albeit more intense, cooling effectiveness region—at least until jet separation. It is worth noting, however, that attached jets with higher M were found to be more effective those with lower M.

In summary, when coolant jets are attached to the surface, prior research shows that cooling effectiveness increases with DR and M, but so does the local heat transfer coefficient due to the complex flow phenomena in the coolant jet. The increased effectiveness is attributed to the increased energy transport capacity of the coolant, though the actual energy transport capacity is rarely taken into account. Once the jet is detached from the surface (high I conditions) the heat transfer coefficient remains elevated with greater DR, but the effectiveness decreases due to the entrainment of freestream air near the model surface. Furthermore, at the high I conditions, the cooling effectiveness and heat transfer scale best with I.

Until recently, the focus of scaling experimentation had been on the effects of DR alone. Rutledge and Polanka [17] used computational fluid dynamics (CFD) to explore the effects of various fluid properties on adiabatic effectiveness and heat transfer coefficient distributions for a simulated leading edge, with a single coolant hole, where coolant was injected at a compound

angle. In this study, they investigated the effects of using CO_2 as a coolant at room temperature, as well as fictitious gases wherein one property was set to the corresponding value for CO_2, while all others were set to those of air. Furthermore, the various scaling parameters were evaluated at representative engine conditions and evaluated with the fictitious gases. The researchers found that ACR and I provided fairly good matching between the baseline air case and the corresponding CO_2 cases in terms of profile and magnitude. Additionally, they found that while ACR provided better effectiveness magnitude matching than I, I better matched the heat transfer coefficient ratio distribution, indicating that I matches the coolant jet placement better than the other coolant flow rate parameters.

In addition to Ref. 17, Greiner et al. [1] used CFD to characterize the influence of commonly neglected coolant and freestream parameters on film cooling effectiveness. In particular, the researchers focused on the relative influence of matching M and DR between low temperature and engine representative flow conditions, while also matching either the freestream Reynolds number, Re_∞, or the coolant Reynolds number, Re_c. They found that when Re_c was matched to a baseline engine condition case, the centerline η distribution matched the baseline case well, though the spanwise averaged distribution, $\bar{\eta}$ matched the baseline better when Re_∞ was matched.

In addition to scaling η results, some researchers have attempted to scale laboratory ϕ results to engine conditions. Albert and Bogard [19] describe a method where low temperature ϕ results can be matched to engine conditions if the Biot number—defined in Eq. (2.29) where t_{wall} is the wall thickness and k_{wall} is the thermal conductivity of the wall material; η; and the ratio of internal and external heat transfer coefficient distributions are matched between the laboratory and engine conditions. As a result, large scale conducting models can be used to

simulate gas turbine hardware, provided that the model material is selected so as to balance the conduction and convection processes during the experiment. Equation (2.30) shows the result of a one-dimensional heat transfer analysis relating η, the Biot number, the ratio of heat transfer coefficients, and the coolant warming factor, χ—defined in Eq. (2.31), to ϕ. This relation shows that in matching these parameters, model material, model size, and experimental temperatures are arbitrary, as long as the nondimensional parameter distributions match that of the engine condition.

$$Bi = \frac{h_f t_{wall}}{k_{wall}} \tag{2.29}$$

$$\phi = \frac{1 - \chi\eta}{1 + Bi + \frac{h_f}{h_i}} + \chi\eta \tag{2.30}$$

$$\chi = \frac{T_\infty - T_{c,e}}{T_\infty - T_{c,i}} \tag{2.31}$$

2.4 Governing Equations of Heat and Mass Transfer in Boundary Layers

The heat-mass transfer analogy presents an attractive experimental option for gas turbine film cooling researchers. Mass transfer methodologies have been appealing to experimentalists in the literature on two fronts. First, the data collected during a mass transfer experiment does not lose accuracy due to the presence of conduction and radiation errors, as mass transfer is a purely convection and diffusion driven process. As such, conditions analogous to adiabatic and isothermal walls (impermeable and uniform composition walls, respectively) are fairly easy to construct and implement. The second appealing feature of mass transfer experiments is that many experiments can be performed at room temperature. For many types of experiments, however, isothermal conditions are necessary, prompting the researcher to use heavy gases, such as CO_2, Ar, and special mixes in order to achieve an engine representative DR.

Prior to discussing the intricacies of the heat-mass transfer analogy, the governing equations of heat and mass transfer must be discussed in detail. Equations (2.32) and (2.33) show the conservation equations for mass (continuity) and momentum, respectively, presented in Einstein vector notation, where the viscous stress tensor is shown in Eq. (2.34), assuming the fluid involved is Newtonian [20]. The ∂ terms refer to a partial derivative along the subscripted index, where the 0 index refers to a partial derivative with respect to time. Furthermore, δ_{ji} refers to the Kronecker delta function. As of now, the only simplifying assumptions that have been made were that the fluid is Newtonian, and that body forces are negligible, both of which are the case for most gases. These equations are equivalent for both single component systems, e.g. film cooling with air as the coolant, and for multi-component systems, such as film cooling with a foreign gas, if considerations for the changes in density and viscosity with local fluid composition are taken into consideration and the local velocity component, u_i, is the mass averaged velocity component [21]. For this reason, though the Mach numbers for many film cooling experiments are low enough for the flow to be considered incompressible, the equations below cannot make the assumption that $\partial_i \rho$ and $\partial_i \mu$ are zero at all locations.

$$\partial_0 \rho + \partial_i (u_i \rho) = 0 \tag{2.32}$$

$$\partial_0 u_i + u_j (\partial_j u_i) = -\frac{1}{\rho}(\partial_i P - \partial_j \tau_{ji}) \tag{2.33}$$

$$\tau_{ji} = -\mu \left[\partial_j u_i + \partial_i u_j - \frac{2}{3} \delta_{ji} \partial_k u_k \right] \tag{2.34}$$

For a pure fluid film cooling experiment, i.e. the freestream and coolant are of the same composition, the convective transport of thermal energy governing equation is fairly simple, especially if the specific heats of the fluid, c_P and c_V are near-constant with respect to temperature. This form of the energy equation is shown in Eq. (2.35). With the introduction of a

non-homogeneous mixture of gases at non-isothermal conditions, the energy transport equation must be defined in terms of enthalpy, rather than temperature, shown in Eq. (2.36) [22]. In order to avoid confusion with the heat transfer coefficient, h_f, the specific enthalpy of the fluid is represented by i in these equations. Furthermore, the subscript λ refers to a particular chemical species, rather than a directional index, $\mathcal{Y}_\lambda$ refers to the local mass fraction of species λ, and ζ_λ is a mass diffusion term specific to species λ. This consideration of enthalpy transport must be made in order to account for the change in the specific heats that results from the non-homogeneous mixture of the foreign cooling gas and the freestream [23]. As such, the distribution of chemical species must be accounted for. The differential equation that governs the convective mass transfer process for a single chemical species, λ, is shown in Eq. (2.37) for non-reacting mixtures.

$$\rho u_i \partial_0 (c_P T) + \rho u_i \partial_i (c_P T) - \partial_i (k \partial_i T) = 0 \tag{2.35}$$

$$\rho u_i \partial_0 i + \rho u_i \partial_i i - \partial_i \left(\sum_\lambda \zeta_\lambda i_\lambda \partial_i \mathcal{Y}_\lambda \right) - \partial_i (k \partial_i T) = 0 \tag{2.36}$$

$$\rho u_i \partial_0 \mathcal{Y}_\lambda + \rho u_i \partial_i \mathcal{Y}_\lambda - \partial_i (\zeta_\lambda \partial_i \mathcal{Y}_\lambda) = 0 \tag{2.37}$$

Though application of Eq. (2.36) is not a simple process, Jones [23] shows that is a necessary consideration when attempting to use foreign cooling gases in thermal experiments with the aim to determine the expected adiabatic wall temperature and heat transfer measurements for air at the same fluid flow conditions (e.g. matched M, DR, and therefore I and VR conditions). Jones shows that for a foreign gas experiment, where η_{FG} is determined using Eq. (2.2), that the analogous case for air at the same DR can be determined using the specific heat ratio between the gas at the wall, which is determined by Eq. (2.38), and the freestream gas.

$\mathcal{Y}_{FG,s}$ refers to the local mass fraction of the cooling gas at the wall, and $c_{P,s}$ refers to the specific heat at constant pressure of the gas mixture at the wall. A necessary assumption for Eq. (2.38) is that the specific heats of the coolant and freestream gases are insensitive to temperature, precluding experimentation with large temperature differences. The relationship between the measured η_{FG} and the analogous case with air, η_{air}, is shown in Eq. (2.39). Substitution of Eq. (2.38) into Eq. (2.39) yields Eq. (2.40), assuming that the specific heat of air has not changed significantly as a result of the temperature difference causing in the elevated DR (i.e. the ratio between the wall and freestream specific heats remains near unity).

$$\eta_{FG} = \frac{T_\infty - T_{aw}}{T_\infty - T_{c,e}} \tag{2.2}$$

$$c_{P,s} = c_{P,\infty}\,(1 - \mathcal{Y}_{FG,s}) + c_{P,FG}\,\mathcal{Y}_{FG,s} \tag{2.38}$$

$$\eta_{air} = \mathcal{Y}_{FG,s} = \frac{c_{P,s}}{c_{P,FG}}\eta_{FG} \tag{2.39}$$

$$\eta_{air} = \frac{c_{P,\infty}\,\eta_{FG}}{c_{P,FG}\,(1 - \eta_{FG}) + c_{P,\infty}\,\eta_{FG}} \tag{2.40}$$

Application of the development by Jones [23], however, requires some major assumptions, which may not be true when attempting to scale to high density ratios, particularly the assumption that the c_P ratio between the cooling and freestream air has not deviated far from unity. As a result, experimentalists often prefer to compare the results of pure fluid thermal distributions, governed by Eq. (2.35), and isothermal mass transfer experiments, governed by Eq. (2.37). When these conditions are met, Eqs. (2.35) and (2.37) are of a similar form, where heat and mass are transferred by two mechanisms, advection and conduction (diffusion in mass transfer processes). The similarity between these governing equations is the basis for the mass transfer analogy to heat transfer.

2.5 The Heat-Mass Transfer Analogy

The heat-mass transfer analogy is often employed by researchers to explore the convective heat transfer characteristics of film cooling schemes since mass transfer is driven purely by convective processes, eliminating the uncertainty of measurements due to conduction into the model surface and radiation that are found in thermal experiments.

Eckert et al. [24] discusses the basis for the heat-mass transfer analogy: the similar dependence of heat and mass transfer on their respective nondimensional diffusion parameters, the Prandtl, Pr, and Schmidt, Sc, numbers respectively, though the Prandtl number is a familiar fluid parameter to aerodynamicists, its definition is included alongside that of the Schmidt number, shown in Eqs. (2.41) and (2.42) respectively, so that the similarity between the parameters is obvious. Both terms are ratios of inertial diffusion to the diffusion process that they govern, the thermal diffusivity, α, for the Prandtl number, and the diffusion coefficient for the transferred substance, $\mathcal{D}$, for the Schmidt number. These parameters are shown by Kays et al. [22] to have similar influences on their respective nondimensional transfer parameters, the Nusselt and Sherwood numbers. Like the comparison between the Prandtl and Schmidt numbers, the definitions of the Nusselt and Sherwood numbers are shown together for the sake of comparison in Eqs. (2.43) and (2.44). The h_f term in Eq. (2.43) is the familiar heat transfer coefficient, while the h_M term in Eq. (2.44) is the mass transfer coefficient [m/s]. In fact, the Nusselt and Sherwood number spatial distributions for a constant temperature or mass fraction plate in laminar flow, shown in Eqs. (2.45) and (2.46), maintain exact dependence on the Reynolds number and the diffusion parameter, provided that Pr and Sc meet the required conditions [22].

$$Pr \equiv \frac{\mu c_P}{k} = \frac{\nu}{\alpha} \tag{2.41}$$

$$Sc \equiv \frac{\mu}{\rho \mathcal{D}} = \frac{\nu}{\mathcal{D}} \tag{2.42}$$

$$Nu \equiv \frac{h_f l}{k} \tag{2.43}$$

$$Sh \equiv \frac{h_M l}{\mathcal{D}} \tag{2.44}$$

$$Nu_x = 0.332\sqrt{Re_x}\sqrt[3]{Pr}\ for\ Pr > 0.6 \tag{2.45}$$

$$Sh_x = 0.332\sqrt{Re_x}\sqrt[3]{Sc}\ for\ Sc > 0.6 \tag{2.46}$$

Similar expressions can be found for other flow and boundary conditions, to include turbulent boundary layers, arbitrarily set temperature/composition walls, and fixed/arbitrary heat/mass flux conditions.

For a perfect heat-mass transfer analogy, the Prandtl and Schmidt numbers are constrained to be equivalent. In the case of many heat and mass transfer experiments, however, exact equality of these two parameters is not possible. Eckert et al. [24], however, showed that the ratio of the Nusselt and Sherwood numbers scaled by a constant factor, dependent on the Prandtl and Schmidt numbers, when all other salient aspects of the flow conditions are matched, i.e. the freestream Reynolds number and the driving boundary conditions. For the constant temperature/mass fraction flat plate with laminar flow, this factor is approximately the cube root of the ratio of the Prandtl and Schmidt numbers, or, more simply, the cube root of the Lewis number, defined in Eq. (2.47). Therefore, a Lewis number of unity is not a strict criterion, though the Prandtl and Schmidt numbers should be of approximately the same magnitude.

$$Le \equiv \frac{\mathcal{D}}{\alpha} = \frac{Pr}{Sc} \tag{2.47}$$

Goldstein and Cho [11] discuss a revision to the strict condition that the Lewis number be unity to apply the heat-mass transfer analogy directly. They show that the *turbulent* Lewis number must be unity, indicating that the diffusion of thermal energy and chemical species are equal in a turbulent mixing field. As a result, if this turbulent diffusion condition is met, the analogy factor takes the form shown in Eq. (2.48), where n is determined empirically for a given geometry and turbulence condition, though the previous result of n = 1/3 is exactly valid for laminar flows over flat plates. In continuing their discussion, however, the authors point out that the relative simplicity of the analogy in Eq. (2.48) breaks down at Reynolds numbers greater than 10^5. They show that the analogy is valid, however, if the formulations for the Nusselt and Sherwood number distributions that account for surface friction are used, allowing the analogy factor to become a function of the Reynolds number.

$$\frac{Nu}{Sh} = \left(\frac{Pr}{Sc}\right)^n = Le^n \tag{2.48}$$

The utility of the heat-mass transfer analogy extends beyond that of determining heat or mass transfer coefficients. As discussed in Section 2.1, the driving temperature for convective heat transfer is the adiabatic wall temperature, T_{aw}. The condition of an adiabatic wall can be simulated by using a model that is impermeable to a selected tracer compound, and measuring the local distribution of an injected tracer compound the system. For an experiment of this type, η is determined using Eq. (2.10). Unlike the convective heat and mass transfer coefficients, Eq. (2.10) is applied directly rather than corrected between the two processes [13], [14], [15].

3. Methodology

The bulk of past film cooling scaling research has focused on DR with little regard to other coolant properties, most notably the thermal transport properties, k and c_P. These parameters were investigated computationally by Greiner et al. [1] and Rutledge and Polanka [17], but have not yet been targeted experimentally. In addition, the increased use of PSP to evaluate film cooling schemes warrants the investigation and comparison of the thermal techniques to the PSP technique. The purpose of this chapter is to describe the experimental setup and methodology for conducting the present research. Included in this chapter are the model and facility characteristics, test procedures, calibrations, spatial distributions, corrections, energy separation phenomena, and experimental uncertainty analyses.

3.1 Model Characteristics

The models utilized in this study replicated the geometry used by Ekkad et al. [10]. The model geometry simulates the leading edge region of a high pressure turbine airfoil as a semi-cylinder in crossflow with a flat afterbody. A schematic representation of the model is shown in Fig. 3.1. The leading edge diameter was D = 8.89 cm, with a coolant hole diameter of d = 0.476 cm, resulting in a leading edge-to-coolant hole diameter ratio of D/d = 18.67. The leading edge thickness was t_{wall} = 1.92 cm. The coolant was ejected onto the surface of the model at a compound angle, shown in Fig. 3.1a, where β = 21.5° from the stagnation line and γ = 20° from the model surface in the plane defined by β and the center of the cylinder, the β-plane (Fig. 3.1b). This coolant ejection angle and model thickness resulted in a cooling hole length-to-diameter ratio of L/d = 11.79.

In order to avoid confusion, the subscript lab is used to refer to the frame of reference for the experiment observer, while the unsubscripted axes refer to the frame of reference on the

surface of the model. As a result, the z-axis in the model frame is normal to the model surface and lies in a plane parallel to the laboratory x-y plane. The x-axis in the model frame points along the model surface, and is positive downstream of the cooling hole. The model y-axis is parallel to the laboratory z-axis, and is positive above the cooling hole.

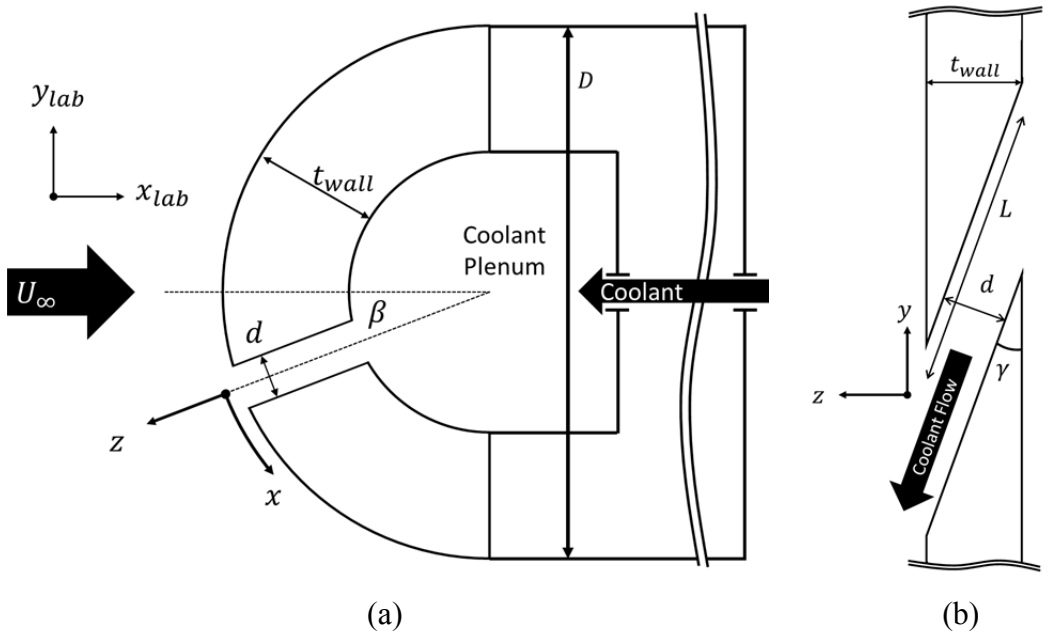

(a) (b)

Figure 3.1. Leading-edge schematic (a) and hole configuration in β-plane view (b).

Two leading edge models were utilized in this study. The first was constructed out of General Plastics Last-A-Foam FR-7106 [25], a high-density, low thermal conductivity foam. The material properties for the foam are: ρ = 96 kg/m^3, c_P = 1260 J/kg-K, k = 0.030 W/m-K. The foam model was painted black with an acrylic spray paint so that uniform surface emissivity was achieved for IR thermography measurements. Additionally, two J-type thermocouples were embedded into the surface away from the cooling hole for in-situ IR calibration purposes. In addition to the surface thermocouples, a J-type thermocouple was placed approximately 1 hole diameter into the cooling hole from inside the model for coolant temperature measurements. This

thermocouple served both as the temperature at which the coolant fluid properties were determined, as well as T_c in Eq. (2.2). The second model was constructed from DuPont Corian® solid surface material, so that it could be painted with binary pressure sensitive paint. The material properties were collected from internal studies performed by DuPont and are: ρ = 1700 kg/m^3, c_P = 1379 J/kg-K, k = 1.009 W/m-K. In addition to the PSP coating, the Corian model was also equipped with a J-type thermocouple, located 1 hole diameter into the cooling hole from the plenum for the determination of coolant fluid properties.

3.2 Facility Characteristics

The wind tunnel used in this study was an open loop, blow-down wind tunnel, powered by up to two 50 hp blowers. A schematic view of the wind tunnel flow path is shown in Fig. 3.2. The freestream flow velocity was controlled by a flow control valve (Fig. 3.2-B), located immediately downstream of the primary blower (Fig. 3.2-C). Three methods were available to control the freestream temperature. To reduce the freestream temperature, chilled water was pumped through a copper tube heat exchanger (Fig. 3.2-F). When using this heat exchanger, the freestream temperature was controlled by the water flow rate, which was set using the bypass valve assembly, shown in schematic form in Fig. 3.3. In order to achieve the minimum possible freestream temperature on a given day, the ball valve (Fig. 3.3-B) was opened so as to allow for the maximum cooling water flow rate. For finer temperature control, the ball valve was closed, forcing the cooling water to flow through the globe valve (Fig. 3.3-A). Using the globe valve, freestream temperature could be set to within 1 K. However, due to the nonlinear relationship between valve setting and coolant flow rate, as well as the weather dependence of the blower output temperature, no attempts to develop a calibration were made. In addition, due to the weather dependence of blower output temperature, the freestream temperature was observed to

drift up to 3 K over the course of an experiment. Larger drifts were prevented by adjusting the water flow rate so as to counteract them.

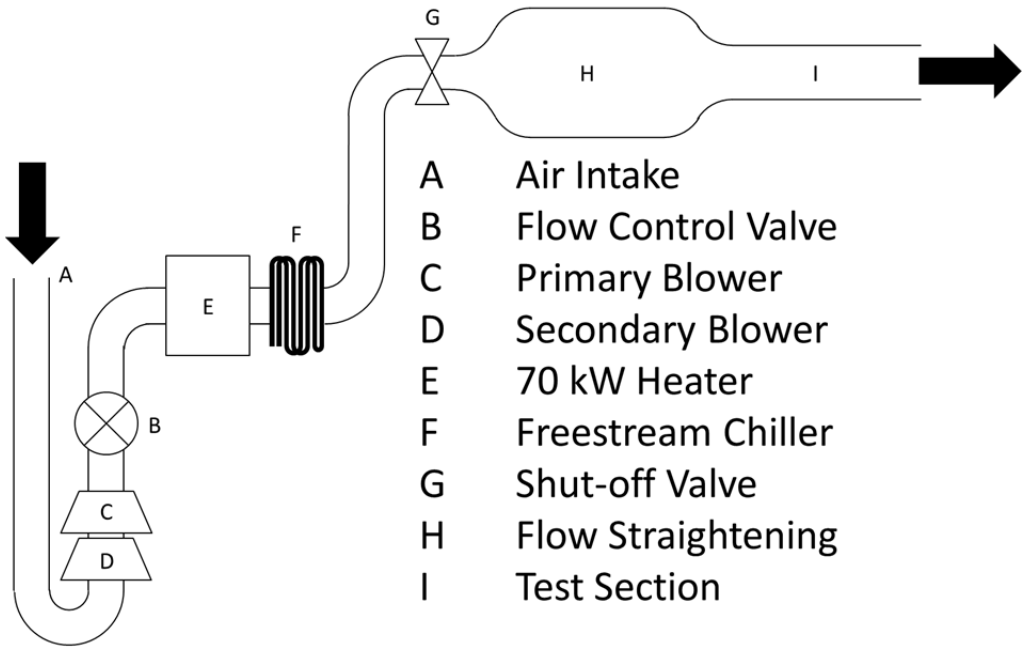

Figure 3.2. Wind tunnel schematic.

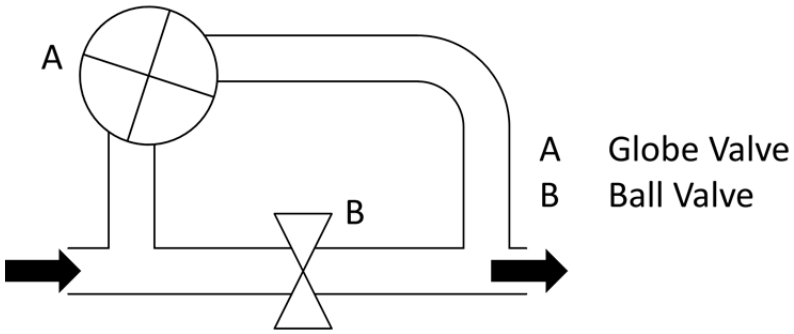

Figure 3.3. Freestream cooling water bypass valve assembly.

The freestream flow was heated using a variety of methods, depending on the magnitude of heating required. Increases in maximum freestream temperature on the order of 3-5 K were accomplished by closing the test cell bay doors so as to force the exhausted freestream to cycle back through the blowers, resulting in a slow increase in freestream temperature. Larger increases in maximum temperature were accomplished by activating both blowers (Fig. 3.2-C

and D). This method resulted in an increase in maximum freestream temperature on the order of 15-20 K. Often, temperatures near 320 K (or 315 K for winter testing) were accomplished by a combination of activating both blowers and cooling the freestream flow to the desired temperature.

Figure 3.4 shows a schematic of the test section (Fig. 3.2-I). The test section was constructed of clear acrylic, with a cross-section of 36.8 cm by 40.6 cm perpendicular to the flow. The turbulence characteristics of this test section were characterized by Rutledge [25], and are displayed in Table 3.1 for a freestream Reynolds number of Re_D = 60000. The high turbulence condition was achieved by placing a square mesh of 1.5 cm diameter round bars, 1.2 m upstream of the leading edge model. The mesh width of the turbulence grid was 6.9 cm.

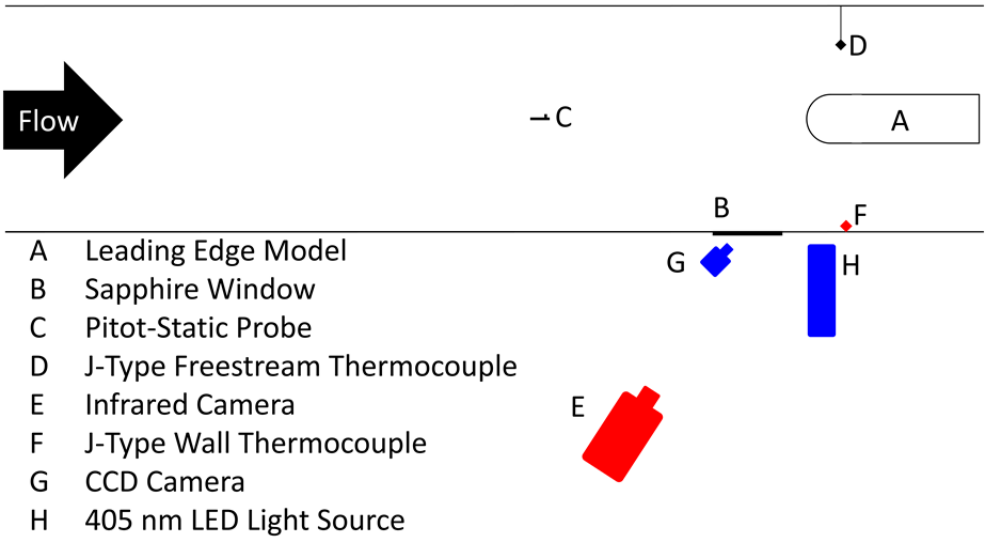

Figure 3.4. Test section schematic for IR (red) and PSP (blue) testing

Table 3.1. Test Section Turbulence Characteristics

Turbulence Condition	Tu (%)	Λ_f/d
Low	0.67	24
High	4.5	7.5

The flow velocity was determined using a pitot-static probe (Fig. 3.4-C), located approximately 73.7 cm upstream of the leading edge model (Fig. 3.4-A). The pitot-static pressure was measured with an Omega PCL-1B manometer, equipped with a 0.5 in-H_2O transducer insert. Freestream density was determined from T_∞ measurements taken with a J-Type thermocouple (Fig. 3.4-D), and an assumed atmospheric pressure of 98358 Pa, the standard-day atmospheric pressure for Wright-Patterson AFB, OH. Assuming a constant day-to-day ambient pressure was considered reasonable because a 2% change in ambient pressure would result in only a 0.8% change in freestream velocity. Freestream viscosity, μ_∞, specific heat, $c_{P,\infty}$, and thermal conductivity, k_∞ were determined by linear interpolation to T_∞ from published data sets for air at approximately 1 atm [26, 27, 28]. In addition to the freestream thermocouple, a second J-type thermocouple was affixed to the wall (Fig. 3.4-F) for wall temperature correction purposes. The wall temperature correction will be discussed in Section 3.4. When in the IR thermography configuration, the IR camera (Fig. 3.4-E) views the leading edge model (Fig. 3.4-A) through a sapphire IR window (Fig. 3.4-B), while the CCD camera (Fig. 3.4-G) views the leading edge model (Fig. 3.4-A) through the sapphire window (Fig. 3.4-B) in the PSP configuration. The model is illuminated by the 405 nm LED source (Fig. 3.4-H) through the wind tunnel walls, since the acrylic walls do not block light in the visible and ultraviolet spectra. In order to reduce signal noise during PSP testing, the test section was covered by black paper, except for the sapphire window and the port for the LED illumination, so as to shield the experiment from ambient light sources.

Coolant was supplied to the model by a separate flow path, shown in Fig. 3.5. For cases where air was used as the cooling gas, the compressed gas supply (Fig. 3.5-A) was a shop line maintained at between 100 and 125 psig. For anaerobic cooling gases, the gas supply was a

compressed gas bottle farm located near the test rig at an initial line pressure of approximately 100 psig. From the supply, the gas delivery pressure was set with a pressure line regulator (Fig. 3.5-B). Separate regulators were used for air and anaerobic gas delivery. The mass flow of cooling gas was monitored by use of a digital flowmeter (Fig. 3.5-C). The flowmeter was an Omega FMA-1609A laminar flow element flowmeter, capable of measuring up to 50 standard liters per minute (SLPM), with preloaded data for various gases. Variable coolant temperatures were achieved by cycling the cooling gas through a variable length, counter flow, tube-in-tube heat exchanger (Fig. 3.5-D). The heat exchanger fluid was a mixture of ethylene glycol and water, which was supplied by a Cole-Parmer PolyStat bath, capable of a heat exchanger fluid temperature range of 253-373 K. This temperature range allowed for a coolant temperature range of 270-320 K, depending on T_∞ due to convective heat transfer processes between the freestream and the model material.

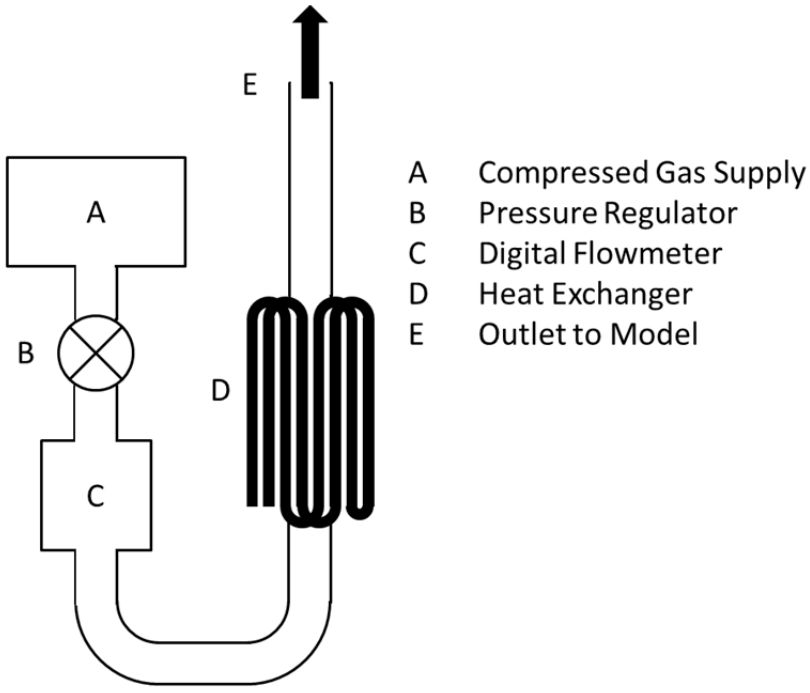

Figure 3.5. Coolant flow path schematic

Coolant fluid properties were determined through linear interpolation of published gas property data for the various cooling gases at a pressure of approximately 1 atm to the coolant temperature measured at the entrance to the cooling hole [26, 27, 28]. The reference pressure for the coolant density calculation was the same as that of the freestream. The binary diffusion coefficients, $\mathcal{D}_{AB}$ [m^2/s], for both the freestream and the coolant diffusing into air were determined using the Chapman-Enskog formula for binary diffusion coefficients, found in Eq. (3.1) [20], where $\mathcal{M}_B$ is the molecular weight of air and $\mathcal{M}_A$ is the molecular weight of the diffusing gas. T_{ref} is a reference temperature, taken to be the average of the gas species temperatures [K] and P_{amb} is the ambient pressure [atm]. σ_{AB} is the mean Lennard-Jones collision diameter [Å], shown in Eq. (3.2), where σ_A and σ_B are the Lennard-Jones collision diameters for the species of interest. $\Omega_{\mathcal{D},AB}$ is the nondimensional collision integral for molecular diffusion, interpolated to $\kappa T_{ref}/\epsilon_{AB}$ from tabulated values, where κ is the Boltzmann constant and ϵ_{AB} is the combined maximum Lennard-Jones attractive energy between molecules of species A and B, shown in Eq. (3.3) [20]. From the determined transport property values, the various nondimensional diffusional transport parameters were calculated for the coolant gases and the freestream, as well as the ratios between these parameters for the coolant to those of the freestream. The diffusional parameters of interest are the Prandtl number (Pr), the Schmidt number (Sc), and the Lewis number (Le).

$$\mathcal{D}_{AB} = 1.8583 \left(\frac{\sqrt{T_{ref}^3 \left(\frac{1}{\mathcal{M}_A} + \frac{1}{\mathcal{M}_B} \right)}}{P_{amb} \sigma_{AB}^2 \Omega_{\mathcal{D},AB}} \right) * 10^{-7} \tag{3.1}$$

$$\sigma_{AB} = \frac{\sigma_A + \sigma_B}{2} \tag{3.2}$$

$$\epsilon_{AB} = \sqrt{\epsilon_A \epsilon_B} \tag{3.3}$$

3.3 Test Procedures

Though both IR thermography tests and PSP test procedures are, for the most part, similar in nature, key differences between the tests warrant the discussion of each test procedure individually.

For IR thermography tests, the model and frame were secured into the test section by means of screws from the ceiling and floor of the test section. The internal coolant line was then attached to the line exit of the coolant heat exchanger (Fig. 3.5-E), and the desired fluid bath temperature was set. The thermocouple wires, to include the freestream and wall thermocouples, were then plugged into the J-type thermocouple extensions, and routed to the thermal data acquisition computer. The IR camera, which for this study was a FLIR SC8300, was then connected to the IR acquisition computer by means of a Cat5E cable, and to the thermal data acquisition computer by means of a BNC cable for triggering purposes. The image frame was selected so that the cooling hole and both surface thermocouples were in clear view. The IR camera was then focused using a metal ruler set on to the model surface in the camera frame. The tunnel shut off valve (Fig. 3.2-G) was opened and the Pitot-static manometer was zeroed. The tunnel was then powered, and the freestream was set to the desired Reynolds number and temperature using the methods discussed in Section 3.2. The desired coolant was then selected and programmed into the flowmeter. In order to reduce the time between individual test points, air from the shop line was cycled through the model so that the coolant temperature was beyond that of the target temperature from the freestream, as changing the flow rate was found to change the coolant temperature. For example, if the desired coolant temperature was 295 K with a

freestream temperature of 315 K, air was cycled so that the coolant temperature reached ~290 K. Likewise, if the desired coolant temperature was 315 K and the freestream temperature was 295 K, air would cycle until the coolant temperature reached ~320 K. The coolant supply was then switched between the shop line and the desired coolant gas bottle, and the model was purged of air.

The coolant flow rate was then set to the flow rate required to reach the desired coolant flow rate parameter value. The required flow rate was calculated from the coolant and freestream temperatures, the freestream velocity, and the molecular weight of the coolant itself. Once the flow rate was set, it was held steady for at least 20 s, as the effect of changing the coolant flow rate lagged behind the process of changing the flow rate, i.e. the coolant flow rate would change and the surface effect would be later observed. Figure 3.6 shows a time history of reported coolant jet effectiveness, where data was collected at 13 s intervals after the coolant flow rate was set for 39 s. The most drastic change in the reported effectiveness distribution occurred between 0 s and 13 s (Figs. 3.6a-b), where the reported effectiveness increases significantly at all points inside of the region of elevated reported adiabatic effectiveness. Comparison of Figs. 3.6b-d shows that development of the coolant jet continues between 13 s and 39 s after the coolant flow rate was set, though compared to the changes between 0 s and 13 s, these changes were considered less significant as further minor development only occurred beyond x/d = 7.5. As a result, the jet was considered to be fully developed and steady after 20 s. After the settling time passed, a single frame of temperature data was recorded with the IR camera. Furthermore, the freestream and coolant temperature data were collected using a LabView system. This LabView system also recorded the coolant-to-freestream property ratios, freestream Reynolds number, and the coolant flow rate.

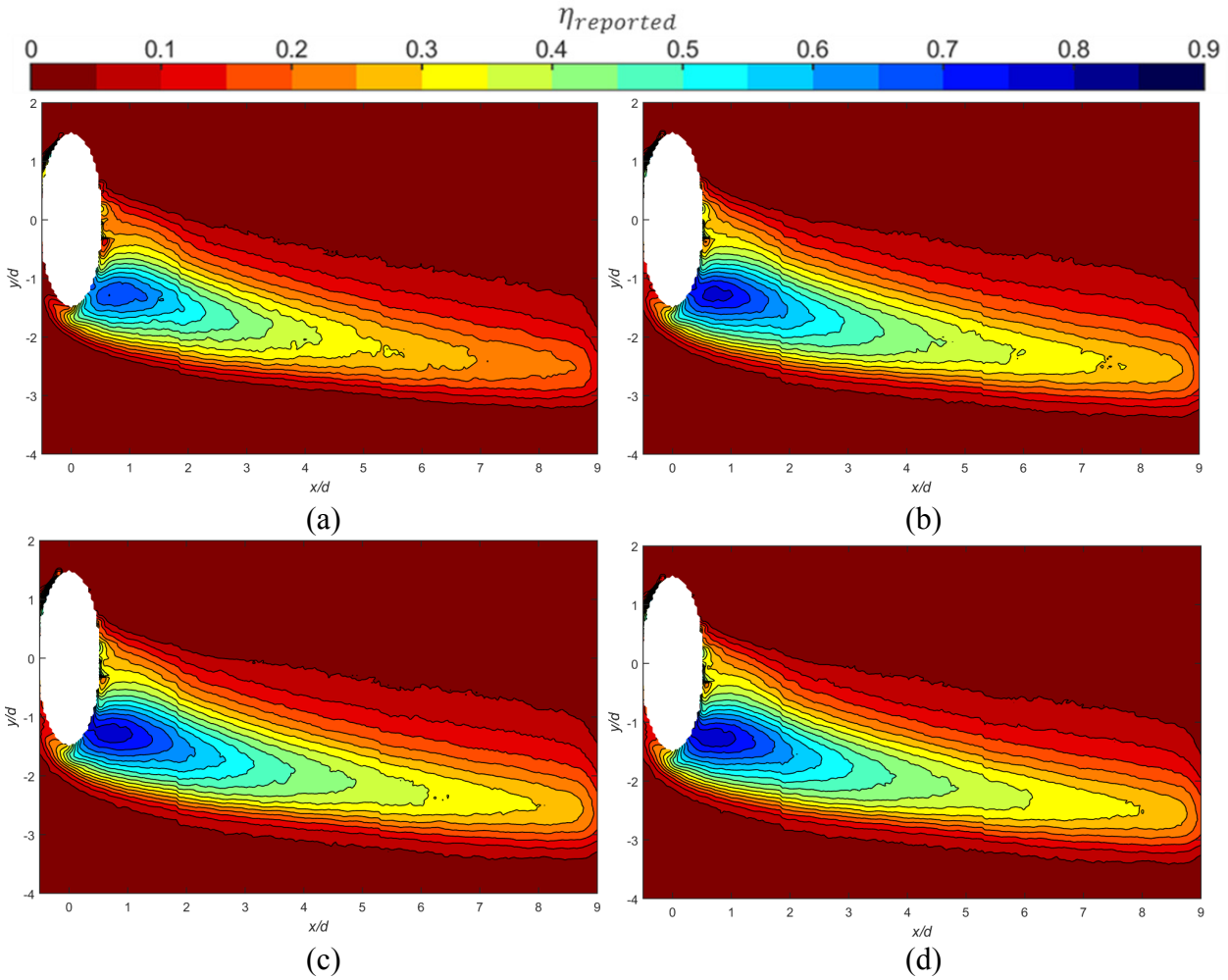

Figure 3.6. Time dependence of reported cooling jet effectiveness, air coolant, M = 1.33, at (a) t = 0 s, (b) t = 13 s, (c) t = 26 s, and (d) t = 39 s

The process for conducting a PSP experiment is similar to that of an IR experiment in terms of model setup, except that the setup procedures must be conducted with an incident radiation shield in place over the model so as to prevent PSP photodegradation during tunnel setup. Once the desired freestream conditions were set, the test cell lights were shut off, tunnel was shut down, the incident radiation shield was removed, and 100 images were collected over 2.25 s by the CCD camera without the 405 nm LED activated to account for a record of background image noise on both the sensitive and reference channels. The 405 nm LED was then

activated and an additional 100 images were collected on both channels to provide a reference image for data reduction. Following the collection of the reference images, the LED was deactivated. Contrary to Li et al. [14] the reference images were only collected once on a given test day since the size of the model used in this study allowed for a region outside of the coolant jet effect region to be used as a correction for photodegradation and other variation over the course of multiple tests. The tunnel was then restarted and allowed to equilibrate at the set Reynolds number and temperature conditions. Since this study focused on the temperature dependent properties of the coolant, the same process was used to set the coolant temperature during PSP testing as IR testing. The coolant flow rate was then set, allowing 20 s of dwell time before the LED was activated. With the LED activated, another set of 100 images was collected at the test point on each channel. At the same time, the thermal data acquisition computer was triggered to collect thermal data while the CCD computer collected the images to record the freestream and coolant temperatures. In post-processing, the six sets of images (three conditions, two channels) were averaged into six separate images. Examples of these averaged images are shown in Fig. 3.7 for the sensitive channel and Fig. 3.8 for the reference channel.

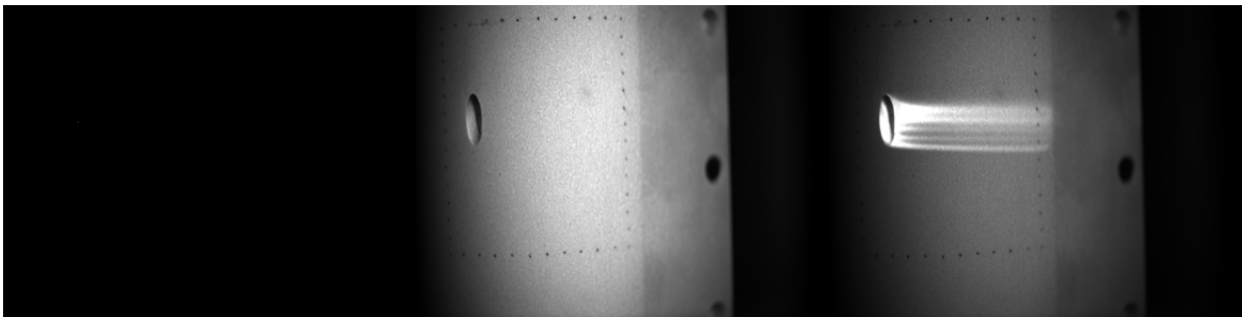

(a) (b) (c)

Figure 3.7. Example sensitive channel (a) background, (b) reference, and (c) test images

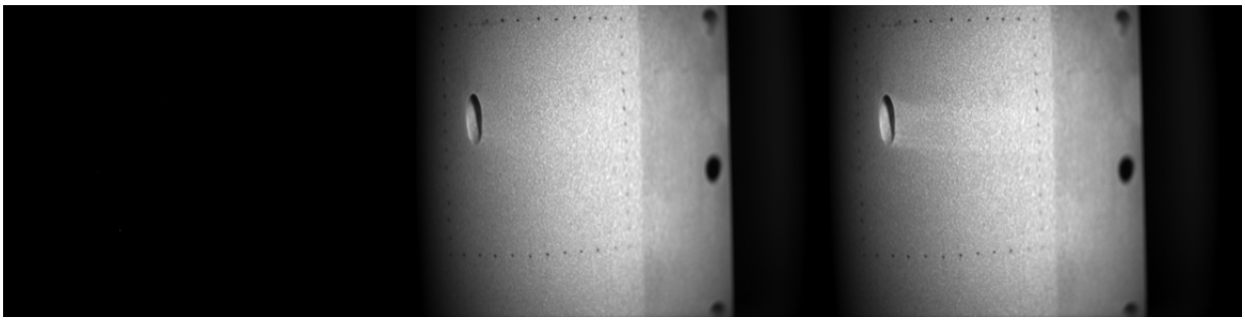

(a) (b) (c)

Figure 3.8. Example reference channel (a) background, (b) reference, and (c) test images

3.4 Infrared Camera Calibration

In order to ensure accurate surface temperature measurements, the IR camera was calibrated in situ using two surface thermocouples embedded into the foam model with a freestream flow over the model. A factory calibration for temperatures between 253 K and 328 K was used as the baseline surface temperature measurement. The apparent (IR) and actual (thermocouple) temperatures were recorded at various temperature conditions. The surface temperatures were varied by controlled changes in the freestream temperature. Temperature data was collected in approximately 1 K intervals through the range of wind tunnel, with multiple images and thermocouple measurements collected at each interval. Furthermore, calibration runs were conducted over the course of several days for repeatability purposes. The apparent temperatures were then fit to the measured temperatures using a second-order polynomial. This curve is shown in Fig. 3.9, and exhibited an uncertainty of $\varepsilon = 1.1$ K. The hysteresis that occurred between infrared measurements of 290 K and 320 K were the primary sources of this uncertainty. The points that lay below the curve were found to have been collected when the freestream was cooled to achieve a particular surface temperature, while the points that lay above the curve were found to have been collected when the freestream cooling was deactivated in order to warm the model surface. In particular, the points centered about an IR measurement of

300 K that lay far below the curve were taken when a rapid freestream temperature change was imposed. This effect was not likely to be the result of an unresolved transient since IR images and thermocouple measurements were collected after the thermocouple temperatures were held within 0.1 K for 10 seconds.

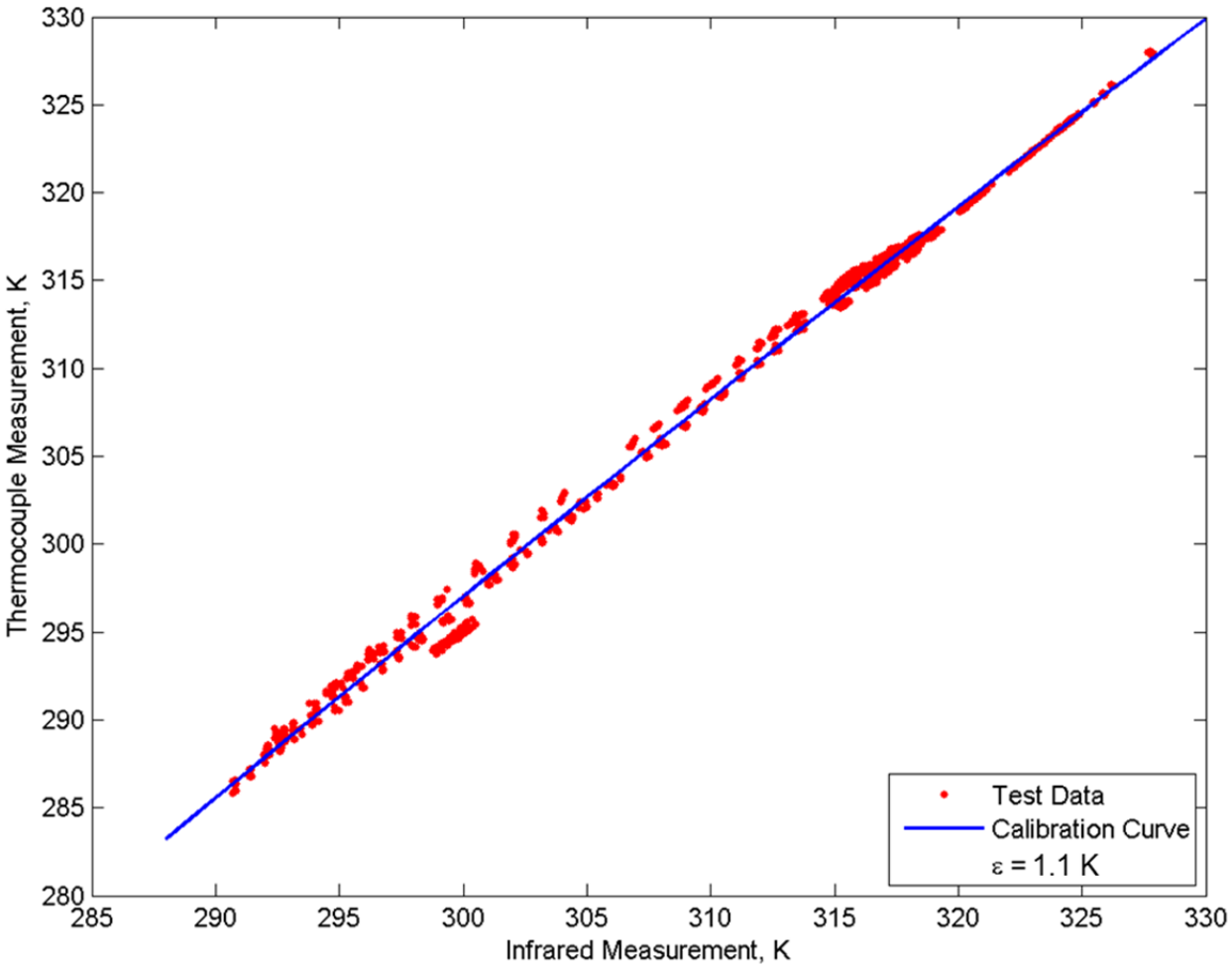

Figure 3.9. Initial IR calibration curve

The hysteresis observed in Fig. 3.9 was found to be a result of reflected radiation from the walls of the wind tunnel, which had a greater temperature than the model surface when the tunnel was being actively cooled and a lower temperature than the model when the tunnel was warming up; resulting in elevated and suppressed IR measurements respectively. In order to account for the effects of the wall temperature, a two-part calibration process was developed.

The first step was to estimate the relationship between the apparent surface temperature and the surface thermocouple measurement using the second order polynomial fit discussed above and is shown in in Eq. (3.4), where T_{IR} is the temperature measured by the IR camera and the a coefficients are the polynomial fit coefficients. The difference between this estimated surface temperature and the tunnel wall temperature as measured by a thermocouple (T_{wall}), δT—defined in Eq. (3.5), was used in conjunction with the initial IR temperature measurement as an independent variable of the multivariable polynomial shown in Eq. (3.6). Furthermore, the a coefficients in Eq. (3.4) were used as initial conditions for the corresponding A coefficients in Eq. (3.6) in the least squares curve fit process, while the A coefficient numbered 4-6 were initialized as zero. The result of this process reduced the uncertainty of the IR thermal measurements to ε = 0.5 K, which was similar in magnitude to the reported 0.3 K uncertainty of the surface thermocouples [25].

$$T_{est} = a_1 T_{IR}^2 + a_2 T_{IR} + a_3 \tag{3.4}$$

$$\delta T = T_{wall} - T_{est} \tag{3.5}$$

$$T_s = A_1 T_{IR}^2 + A_2 T_{IR} + A_3 + A_4 T_{IR}^2(\delta T) + A_5 T_{IR}(\delta T) + A_6(\delta T) \tag{3.6}$$

3.5 Spatial Calibration

Since experimental data was collected with an optical device for both the IR and PSP methods, spatial calibrations were necessary in order to determine the spatial distribution of the data. Furthermore, each method required its own spatial calibration procedure, though the methods were similar.

For the PSP spatial calibration, a grid of 5.08 mm squares was attached to the surface of the leading edge model. The resulting grid pattern, shown in Fig. 3.10, was used to determine the coordinate distribution on the surface of the model. The image was then rotated in order to correct for the apparent "lean" observed in the grid. Once rotated, the optical distortion observed near the edges of the image was found to be insignificant relative to the model scale, and the grid was assumed to rectilinear. A rectilinear mesh was constructed from the grid points with the origin of the grid located at the center of the coolant hole. Due to the large portion of the available camera field used for PSP measurements, this calibration process was completed any time the camera or model was removed and remounted in the test setup.

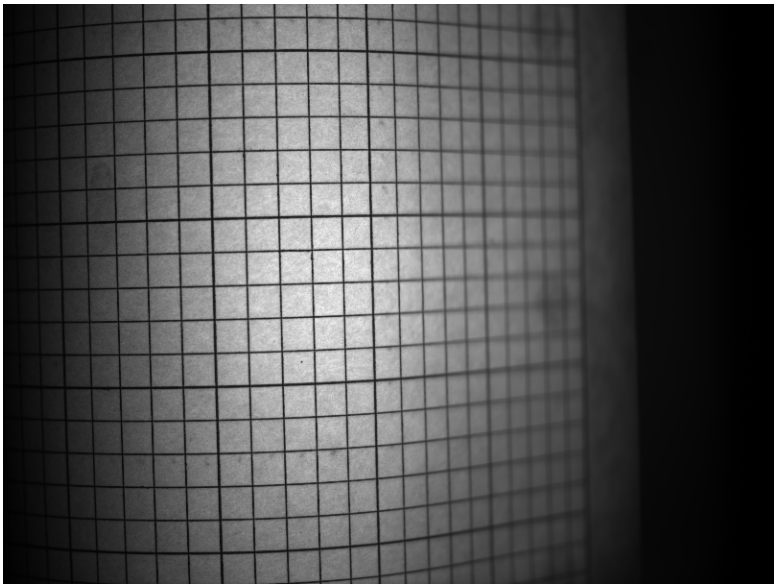

Figure 3.10. Sample image for surface coordinate determination in PSP experiments

The surface grid used for the PSP spatial distribution, however, does not appear when observed in the IR spectrum. In order to determine the surface coordinate distribution on the IR model, a tape was constructed with steel pins inserted at 5.08 mm intervals in the x-direction and at 5.08 mm intervals in the y-direction every 25.4 mm in the x-direction. The tape and model surface were heated with a heat gun so that the steel pins would be readily visible with the IR

camera, as shown in Fig. 3.11. The locations of the pins in the x-direction were fit to a third order polynomial in order to account for the effects of surface curvature, while the interval of the pins arranged in the y-direction were assumed constant. Like the spatial distribution used for PSP experiments, the origin of the spatial grid used in IR experiments was set to the center of the coolant hole, however, since the IR camera field was much larger than the region of interest, small changes in image window size and model location within the image were considered to be insignificant, requiring only one spatial calibration for IR measurements.

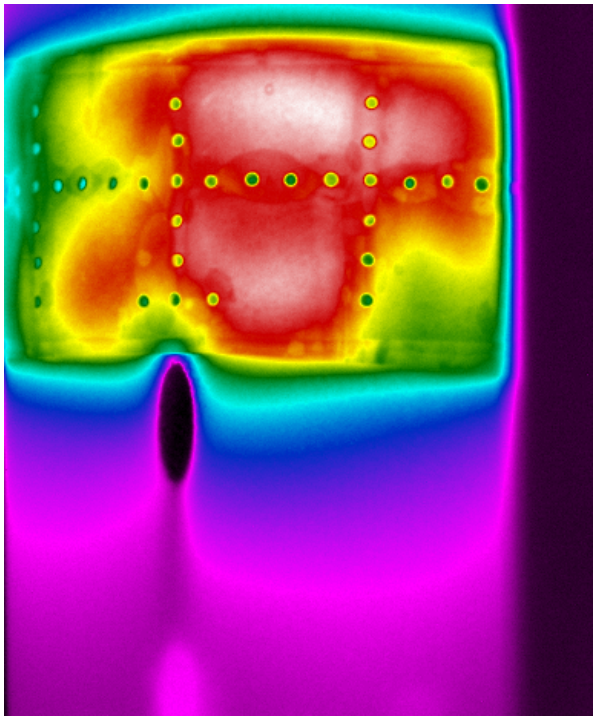

Figure 3.11. Sample image for surface coordinate determination in IR experiments

3.6 Conduction Correction

As discussed in Section 2.2.1, no model material is actually adiabatic, requiring the adiabatic effectiveness to be defined as in Eq. (2.5). The second term that appears in Eq. (2.5) accounts for the convective heat transfer to the model, which is difficult to measure. In order to reduce the uncertainty due to estimating this heat flux, a low thermal conductivity material is

often used for model construction, though this heat transfer must still be accounted for. The conduction correction described by Williams et al. [7] was used in this study, which is a simple one-dimensional method described by Eq. (3.7), where η_{app} is the apparent adiabatic effectiveness observed during a thermal experiment, defined Eq. (3.8), and η_0 is the baseline adiabatic effectiveness that is present due to heat transfer through the model. A sample η_0 profile is shown in Fig. 3.12.

$$\eta = \frac{\eta_{app} - \eta_0}{1 - \eta_0} \tag{3.7}$$

$$\eta_{app} = \frac{T_\infty - T_s}{T_\infty - T_c} \tag{3.8}$$

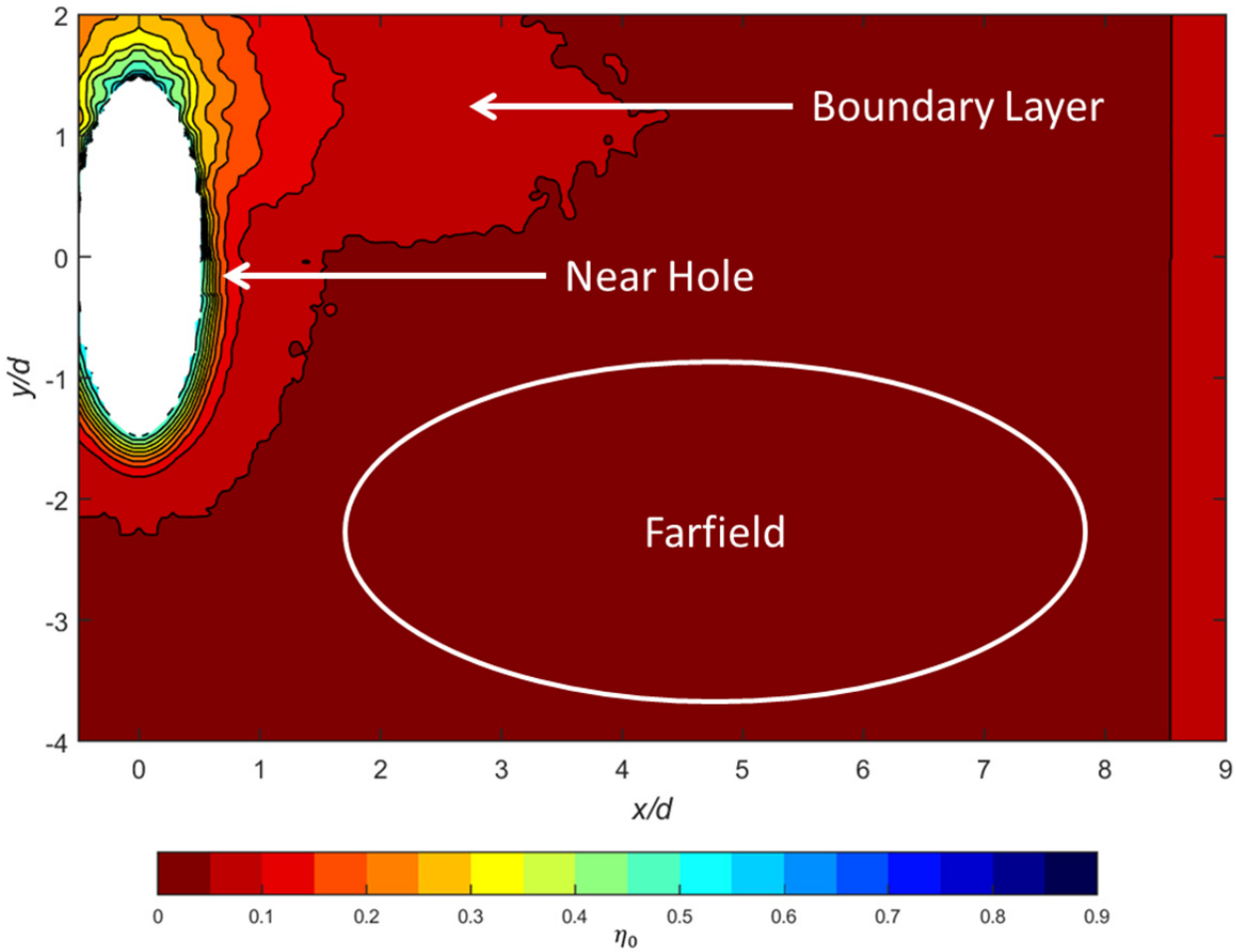

Figure 3.12. Sample η_0 distribution

There are three primary regions that an η_0 profile describes. The first is in the farfield region, where heat is transferred to the model due to a temperature gradient between the freestream flow and the coolant plenum located behind the leading edge surface. The second is the near-hole region, where the coolant temperature influences the model material temperature as it flows through the coolant channel. The third region that requires correction is above the coolant hole. In this region, the thin layer of material that makes up the coolant channel is significantly influenced by the cooling flow, and this influence penetrates into the boundary layer, resulting in an observed apparent adiabatic effectiveness above the hole, where there is no coolant flow. Furthermore, this conduction correction is one-dimensional, and the lateral conduction throughout the coolant jet is not accounted for. Additionally, the complex heat flows that occur near the coolant hole itself cannot be accounted for with this simple method, resulting in poor data quality near the coolant hole. For this reason, conclusions cannot be drawn from experimental results obtained less than one hole diameter downstream of the coolant hole.

The η_0 distribution shown in Fig. 3.12 was the result of stitching together the representative regions of apparent effectiveness distributions at various coolant flow rates. The near-hole and farfield effectiveness regions were determined using data obtained from relatively low flow rate conditions where the coolant plume was primarily located directly behind the cooling hole. For the farfield region, the η_0 distribution was determined by averaging η_{app} values between y/d = -4 and y/d = -5 for the full range of x/d. In the near-hole region, the η_0 distribution was obtained from η_{app} data around, though upstream, of the coolant hole. This distribution was then applied to all locations not effected by the boundary layer region. The boundary layer region η_0 distribution was determined from a high flow rate case, which caused an increased level of heat transfer from the cooling channel to the model surface. Furthermore,

the elevated flow rate displaced the coolant plume far from the boundary layer region, ensuring that apparent effectiveness that resulted from the coolant trace was not corrected out. In order to prevent sharp discontinuities in the η_0 distribution, the image seams were blended together using a median filter.

3.7 Surface Pressure Distribution

As discussed in Section 2.2.3, the partial pressure distribution of O_2 when using air as the coolant must be considered when determining η with PSP. Knowledge of this partial pressure distribution is necessary because the PSP is sensitive to the partial pressure of O_2 regardless of whether the change was a result of oxygen displacement or a change in the absolute pressure on the model surface. However, in order for the absolute pressure beneath the coolant plume to be accurately considered, the air coolant plume must lay onto the model surface at the same location as the anaerobic coolant plume of interest. In order to accomplish this, Han and Rallabandi [29] recommend injecting air at the same blowing ratio as desired for the anaerobic gas. When using a flat plate model (and at sufficiently low blowing ratios), matching the blowing ratio may be sufficient. However, in momentum dominated flow fields, the blowing ratio does not accurately capture the jet dynamics and placement of the jet [18]. Since there was no clear way to place the air and anaerobic coolant traces by matching a single coolant flow rate parameter, a sweep of air flow rates from 0 to 50 SLPM was conducted at both turbulence conditions and the resulting pressure distributions were collected. Over the range of flow rates and turbulence levels, no significant deviation from the uncooled pressure distribution was observed downstream of the cooling hole, indicating that there was an insignificant pressure effect from the coolant jet. This result was expected since at these flow conditions, the freestream dynamic pressure required to achieve a Reynolds number of 60,000 was approximately 80 Pa, and even if the dynamic

pressure of the coolant jet were 10 times greater than the coolant jet—corresponding to a momentum flux ratio of 10—the jet dynamic pressure would be approximately 800 Pa, which would result in a deviation from the ambient pressure on the surface of 0.8%. As a result, the surface pressure distribution that results from the cooling jet was assumed to be that of the surface pressure distribution far from the cooling hole on the model surface. At higher velocities and Mach numbers than those used in the present work, however, this approximation would not likely be valid due to compressibility effects.

3.8 Energy Separation Phenomenon

At the outset of this study, helium gas was intended to be implemented as a low density, high c_P coolant. However, a severe energy separation effect was observed. Energy separation refers to the phenomenon where the coolant plume thermal distribution separates into hot and cold regions (rather than just one region of relatively warm or cool fluid). This phenomenon was not observed to be an effect of mixing with the freestream as it was observed when the freestream and coolant temperatures were matched within 0.5 K. Furthermore, this effect was not found to be a result of participating media skewing the surface temperature measurements, as measurements were verified with a thermocouple. Further hypotheses regarding the origin of this phenomenon are presented at the end of this section. The energy separation phenomenon was quantified for air, Ar, CO_2, N_2, and He and the magnitude of this separation effect was defined as shown in Eq. (3.9), where $\bar{T}$ is the average between the freestream and coolant temperatures.

$$\Delta T = T_s - \bar{T} \tag{3.9}$$

The gases were evaluated at three momentum flux ratios, I = 0.25, 1.0, and 2.0 with a freestream Reynolds number of 60,000 at a matched freestream and coolant temperature, $T_\infty = T_c$ = 294 K.

The experimental conditions for the low flow rate (I = 0.25) are shown in Table 3.2 for each gas, as well as the maximum and minimum deviations from $\bar{T}$. Furthermore, ΔT contours at these conditions are shown in Fig. 3.13. At these conditions, the monatomic gases (He and Ar) were found to be more susceptible to energy separation than that of the diatomic (air and N_2) and triatomic (CO_2) gases. As such, the air and N_2 cases (Fig. 3.13a and Fig. 3.13b, respectively) show little energy separation effect throughout the flow field, and exhibit poorly defined coolant traces. Though CO_2 does not exhibit large energy separation regions, the coolant trace appears to separate into two distinct regions, with a warm region behind the upper half of the cooling hole and a cool region behind the lower half. However, the magnitude of separation was less than 1.0 K. Ar, however, exhibits regions of energy separation where the fluid reaches ΔT magnitudes greater than 1.0 K. In particular, a warm region centered at approximately y/d = 0.6, x/d = 1.0 and a cool trace located at y/d = -0.6 and 0.0 ≤ x/d ≤ 1.0. Finally, at these conditions, He exhibits the greatest of energy separation with a cold region located behind the upper half of the coolant hole and a hot region behind the lower half of the coolant hole. The cold region reached a temperature difference of ΔT = -8.7 K, while the hot region reached ΔT = 12.2 K.

Table 3.2. Energy Separation Characterization Conditions, I = 0.25

Coolant	T_∞ [K]	T_c [K]	$\bar{T}$ [K]	ΔT_{max} [K]	ΔT_{min} [K]
Air	294.5	294.4	294.4	0.5	-0.1
Ar	294.2	294.4	294.3	1.2	-1.2
CO_2	294.4	294.3	294.3	0.4	-0.7
He	294.2	294.1	294.2	12.2	-8.7
N_2	294.2	294.1	294.2	0.2	-0.3

Increasing the coolant flow rates to I = 1.0 resulted in a decrease in ΔT magnitude for each coolant, as shown in Table 3.3 and Fig. 3.14. As a result, air, N_2, and CO_2 (Fig. 3.14a-c)

behaved similarly with matched coolant and freestream temperatures. Furthermore, the Ar coolant jet (Fig. 3.14d) did not exhibit any regions with a ΔT magnitude greater than 1 K, though a maximum positive ΔT of 0.7 K was observed. Finally, the He jet (Fig. 3.14e) did not exhibit the hot region that was observed when I = 0.25, though a cold region was observed behind the coolant hole, as well as in the region $y/d \in$ [-2.75, -1.0] and $x/d \in$ [0.25, 8.0]. The hot region was not observed for the I = 1.0 case because the hot portion of the cooling flow was likely ejected into the freestream flow and did not stay attached to the model surface where it could be measured—the location where the 1.7 K warming was observed was at the top upstream edge of the cooling hole.

Table 3.3. Energy Separation Characterization Conditions, I = 1.0

Coolant	T_∞ [K]	T_c [K]	$\bar{T}$ [K]	ΔT_{max} [K]	ΔT_{min} [K]
Air	294.4	294.4	294.4	0.3	-0.2
Ar	294.2	294.3	294.3	0.7	-0.3
CO_2	294.2	294.2	294.2	0.3	-0.3
He	294.3	294.1	294.2	1.7	-7.2
N_2	294.2	294.1	294.2	0.3	-0.2

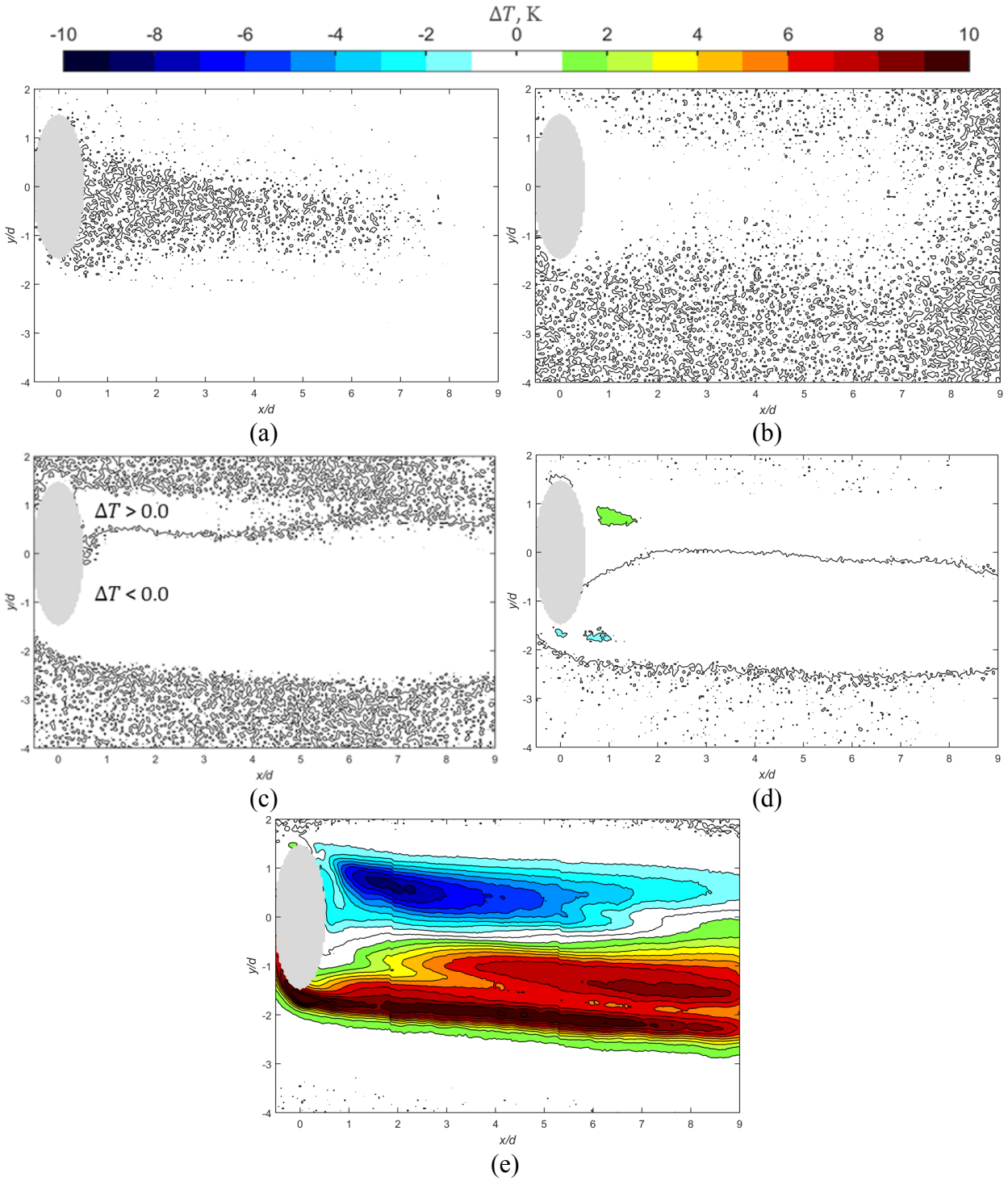

Figure 3.13. ΔT contours for (a) Air, (b) N_2, (c) CO_2, (d) Ar, and (e) He, I = 0.25

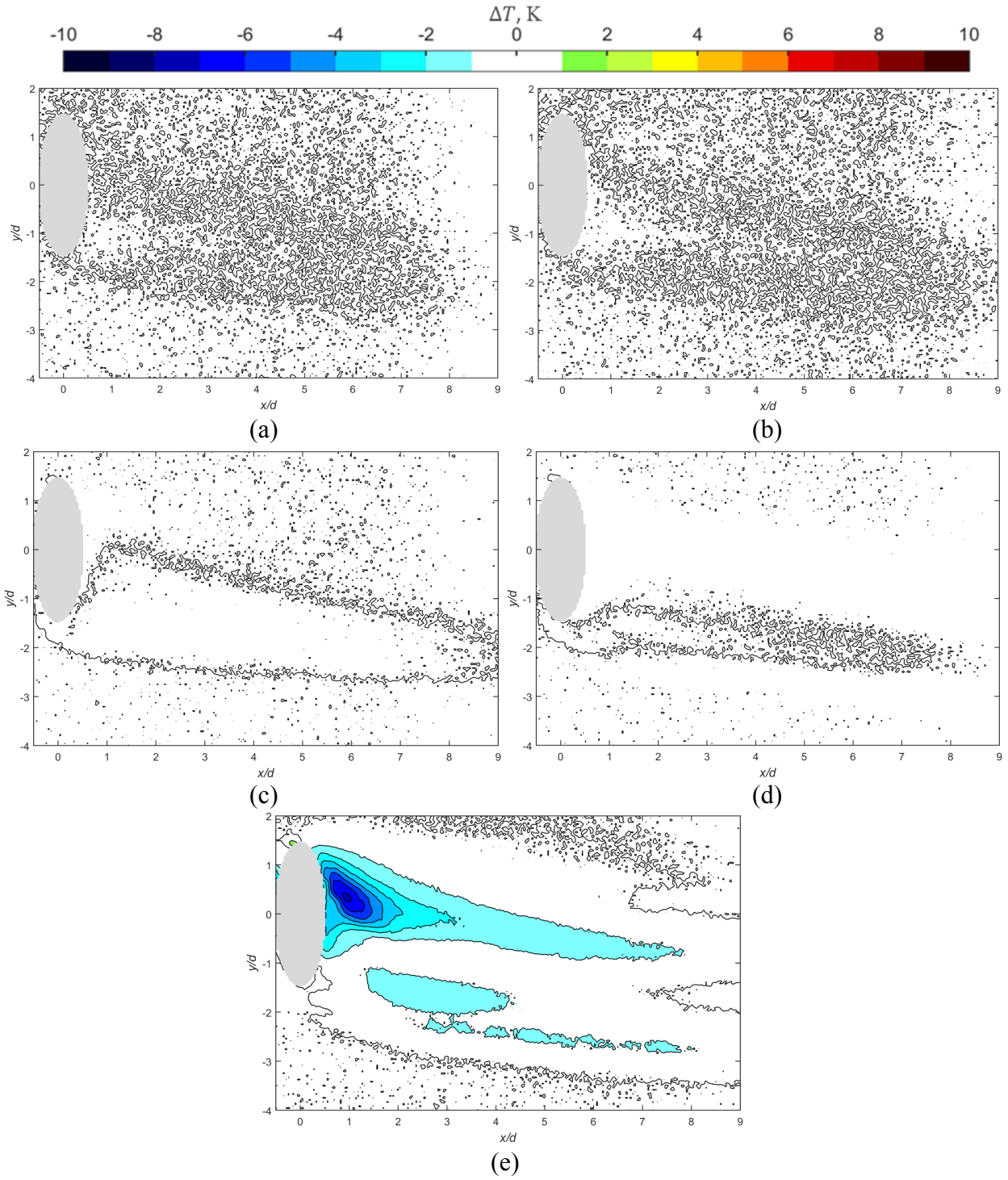

Figure 3.14. ΔT contours for (a) Air, (b) N_2, (c) CO_2, (d) Ar, and (e) He, I = 1.0

Further increasing the coolant flow rates to reach momentum flux ratio of I = 2.0 resulted in the conditions tabulated in Table 3.4 and shown in Fig. 3.15. At these conditions, air, N_2, and

CO_2 each exhibited equal ΔT_{max} and ΔT_{min} values, as well as similar values to the I = 1.0 case. Likewise, Ar performed in a similar manner to its I = 1.0 case, where the same 0.7 K increase was observed. The He jet exhibited a less extreme cooling effect behind the hole when compared to the I = 1.0 case, though two distinct cooling "tails" were observed in the behind the cooling hole, with the secondary cooling trace located below the primary trace. Furthermore, no hot region was observed downstream of the coolant hole, rather, the location where the 1.6 K increase was observed at the upper, upstream edge of the cooling hole, like that of the I = 1.0 case.

Table 3.4. Energy Separation Characterization Conditions, I = 2.0

Coolant	T_∞ [K]	T_c [K]	$\bar{T}$ [K]	ΔT_{max} [K]	ΔT_{min} [K]
Air	294.3	294.3	294.3	0.4	-0.2
Ar	294.1	294.3	294.2	0.7	-0.2
CO_2	294.3	294.2	294.2	0.4	-0.2
He	294.3	294.2	294.2	1.6	-4.7
N_2	294.2	294.1	294.2	0.4	-0.2

As a result of the extreme energy separation phenomena observed with He, He cooling was not considered for adiabatic effectiveness measurements, as surface temperature distributions that resulted from experimental conditions (such as specified T_∞ and T_c) could not be decoupled from the effects of the energy separation and could result in η values much greater than unity or much less than zero. Furthermore, though PSP experimentation would, theoretically, avoid the energy separation effects of He, the relatively extreme temperatures could heat or cool the PSP surface to a temperature outside of its calibration range, adding further uncertainty. Ar and CO_2 were considered to be valid cooling gases for this study since the

imposed experimental temperature differences could be set so as to dominate the energy separation phenomena at any flow rate.

One possible explanation for the energy separation phenomena is that the shear layers that form between the coolant jet and the freestream flow create vortices near the model surface that can cause the separation of the flow into hot and cold sections [30]. This explanation, however, does not account for why only notable energy separation was observed when the gas was non-diatomic, or why CO_2 and Ar exhibited warming regions above the cooling regions while He exhibited heating regions (when observed) below the observed cooling regions.

A second hypothesis for the cause of the energy separation phenomena is that the coolant plenum and cooling hole inadvertently act as a Ranque-Hilsch tube which results in the separation of a compressed gas flow into hot and cold jets which eject from opposite sides of the device [31]. This separation is a result of the hot gas being "spun" to the outer section of the vortex while the core remains cold. There are three reasons, however, that it is unlikely that the cooling geometry acts as a Ranque-Hilsch tube at these conditions. First, the coolant pressures are near ambient as they enter the plenum, while the Ranque-Hilsch tube requires elevated pressures. Second, Ranque-Hilsch tubes often utilize air as the working fluid, though air exhibited no energy separation response in these experiments. Finally, the coolant hole is the only exit from the coolant plenum, so the vortex separation that is required for Ranque-Hilsch tube operation is not likely.

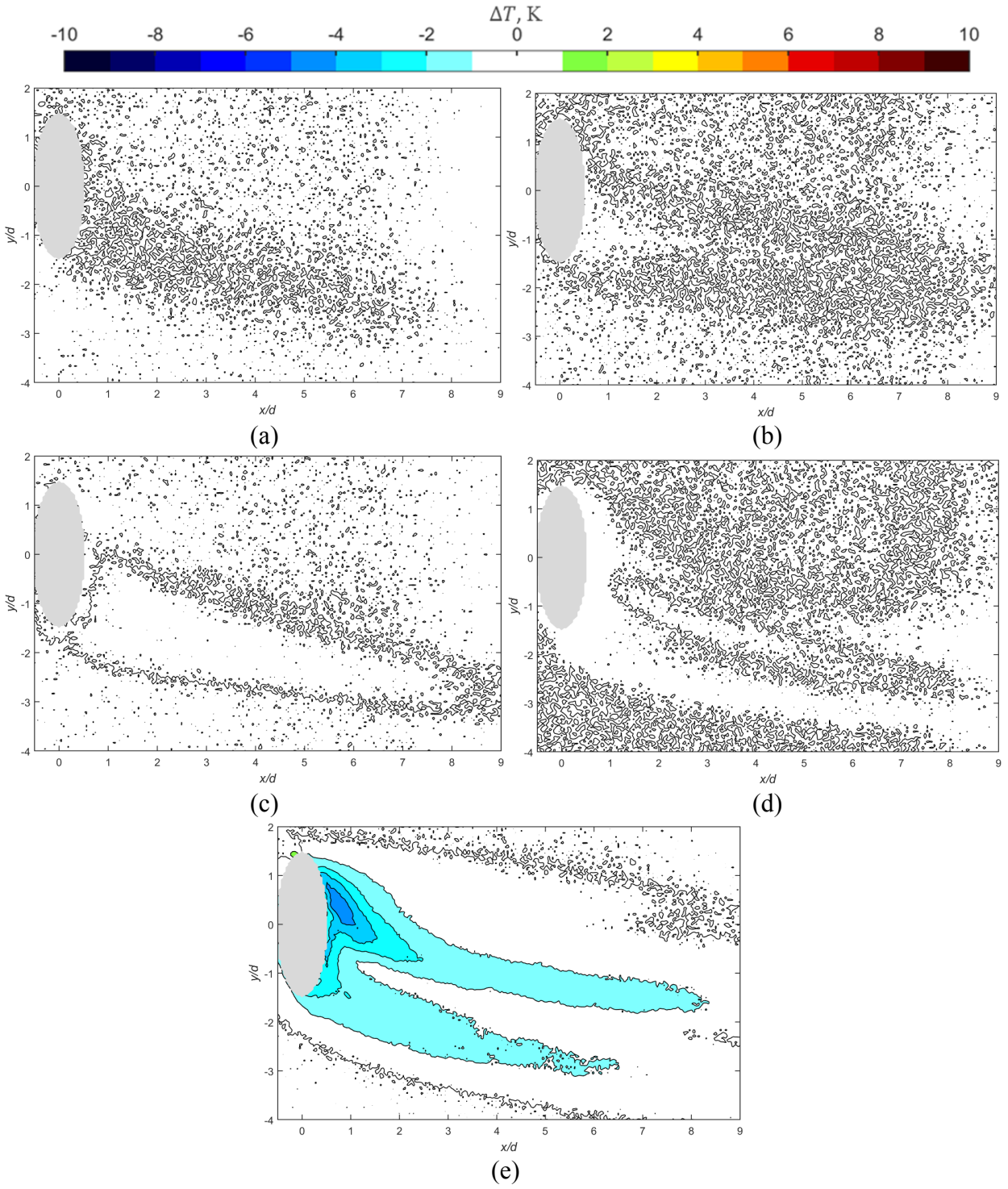

Figure 3.15. ΔT contours for (a) Air, (b) N_2, (c) CO_2, (d) Ar, and (e) He, I = 2.0

A third hypothesis regarding the source of these phenomena is that there is a kinetic interaction between the freestream air and the coolant gases. Since the freestream air is diatomic,

thermal energy can be stored as translational kinetic energy, rotational kinetic energy, and vibrational kinetic energy—though at the temperatures of interest, translational and rotational modes of energy storage dominate the vibrational mode [32]. Likewise, the N_2 and the air coolants are diatomic and carry the same energy storage modes. As such, when the N_2 and air coolant particles are struck by the freestream air particles, the net changes in the coolant flow field energy storage portions (the amount of energy stored in the translational and rotational modes) are approximately zero. As a result, no net energy is added to (or removed from) the rotational storage mode which would result in a change in the translational storage mode, which is related to the observed temperature (sometimes known as the heavy particle temperature) [32]. However, if the coolant gas was monatomic, energy can only be stored in the translational mode (at experimental temperatures). As a result, intermolecular interactions between the coolant and the freestream can only change the translational kinetic energy of the coolant, though both the rotational and translational kinetic energies of the freestream can be changed. This could result in a non-zero net change in the freestream and coolant particle translational energies in certain regions of the flow, which would be observed as changes temperature. It is also possible that a similar process could occur when using CO_2 which, due to its molecular structure and modes of energy storage, could cause an energy separation effect.

3.9 Uncertainty Analysis

The characterization of experimental uncertainty was accomplished using the methods presented by Kline and McClintock [33]. For an arbitrary function ζ that is determined from measured quantities, ξ_{1-N}, the uncertainty in ζ is found using Equation (3.10), where ε_{ξ_i} refers to the measurement uncertainty of a particular measured quantity.

$$\varepsilon_\zeta = \sqrt{\left(\frac{\partial \zeta}{\partial_{\xi_1}}\varepsilon_{\xi_1}\right)^2 + \left(\frac{\partial \zeta}{\partial_{\xi_2}}\varepsilon_{\xi_2}\right)^2 + \cdots + \left(\frac{\partial \zeta}{\partial_{\xi_N}}\varepsilon_{\xi_N}\right)^2} \tag{3.10}$$

3.9.1 Freestream and Coolant Conditions

The uncertainty in the freestream Reynolds number was determined by Rutledge [25] to be primarily driven by uncertainty in the freestream velocity measurement, which was characterized as 1%. As a result, the uncertainty in Re_∞ was considered to be 1% as measured and the measured value was set to be within 2% of the target value of 60,000 for each test, resulting in an overall possible deviation in Re_∞ of 3% between test cases.

Temperature dependent gas property ratios were determined through the use of the Ideal Gas Law, linear interpolation of tabulated data, and through the use of the Chapman-Enskog formula for binary diffusion coefficients. Both the Ideal Gas Law and Chapman-Enskog formula were sensitive to the molecular weight of the evaluated gas as well as the ambient pressure, but for the purposes of this study, the molecular weights and ambient pressures were considered to be constants. As a result, the uncertainty in DR was only a function of the temperature uncertainty. Furthermore, the uncertainty in the Chapman-Enskog formula for binary diffusion was approximately 6% [20]. Each property table had its own reported uncertainty, but the worst case uncertainty was observed for CO_2 with ε_μ = 2%, ε_k = 2%, and ε_{c_P} = 0.5% [26, 27, 28]. The uncertainties in the temperature dependent properties of the other gases were considered to be equivalent to the CO_2 uncertainties for a conservative uncertainty estimate. At the nominal conditions of T_∞ = 315 K and T_c = 295 K, the coolant-to-freestream property ratios exhibited the uncertainties as shown in Table 3.5 where the lowest uncertainty was observed in the density ratio and the highest was observed in the binary diffusion coefficient ratio.

Table 3.5. Property Ratio Uncertainty at T_∞ = 315 K and T_c = 295 K

$\varepsilon_{\rho_c/\rho_\infty}$	$\varepsilon_{c_{P,c}/c_{P,\infty}}$	$\varepsilon_{\mu_c/\mu_\infty}$	$\varepsilon_{k_c/k_\infty}$	$\varepsilon_{\mathcal{D}_{AB,c}/\mathcal{D}_{AB,\infty}}$
0.2%	0.7%	2.8%	2.8%	8.5%

The coolant flow rates were set in terms of the mass flow through the cooling channel, which was measured in SLPM. The flowmeter accuracy was reported by the manufacturer as $\varepsilon_{\dot{m}} = \pm$ (0.8% reading + 0.1 SLPM). This resulted in the uncertainty in coolant flow rate as shown in Fig. 3.16 where the uncertainty is characterized as a fraction of the mass flow rate reading. This uncertainty profile is applicable to each gas used in this study. Furthermore, the natural fluctuations in the coolant line over the course of a single test were less than the uncertainty in the displayed flow rate. The majority of the coolant flow rates that were evaluated in this study were greater than 5 SLPM, which corresponds to an uncertainty in flow rate of 2.8% with one case evaluated at a flow rate of 3 SLPM, corresponding to an uncertainty of 4.1%. At the nominal conditions of T_∞ = 315 K, T_c = 295 K, and Re_∞ = 60,000, the uncertainty in the blowing ratio for CO_2 (the gas at the lowest flow rate) flowing at 3 SLPM was found to be 4.2%. However, for the majority of the coolant flow rates, the uncertainty in the blowing ratio was found to be less than 3%. The uncertainties in the other coolant flow rate parameters were determined by redefining them in terms of M as shown in Eqs. (3.11)-(3.14). The uncertainties in the coolant flow rate parameters were evaluated at a nominal condition of M = 1.0 with air assuming an uncertainty of 3% in M. At these conditions, VR and ACR each exhibited an uncertainty of 3%, dominated by the coolant flow rate. ReR exhibited an uncertainty of 4.2% due to its inverse dependence on the dynamic viscosity ratio, μ_c/μ_∞. Finally, I, exhibited an uncertainty of 6% due to its dependence on M^2, rather than M.

$$VR = \frac{M}{DR} \tag{3.11}$$

$$I = \frac{M^2}{DR} \tag{3.12}$$

$$ACR = M\left(\frac{c_{P,c}}{c_{P,\infty}}\right) \tag{3.13}$$

$$ReR = M\left(\frac{\mu_\infty}{\mu_c}\right) \tag{3.14}$$

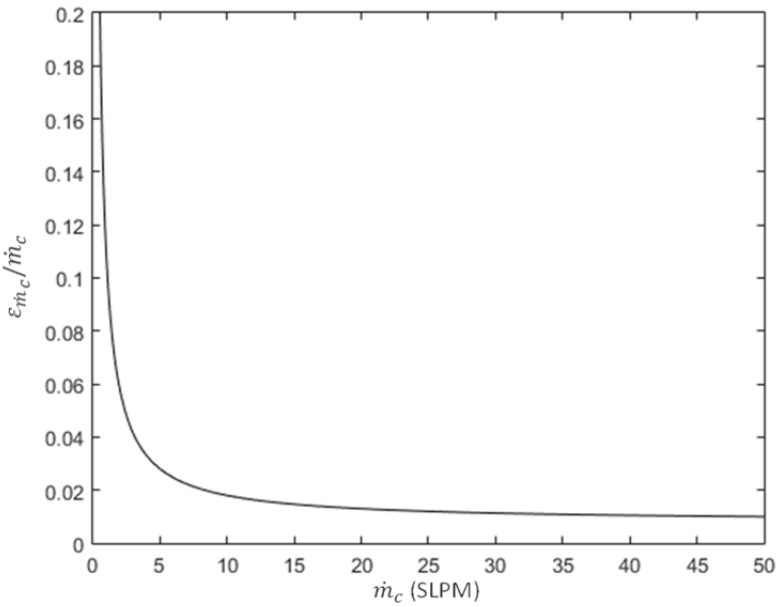

Figure 3.16. Uncertainty in coolant mass flow as a function of reading

3.9.2 Thermal Adiabatic Effectiveness Uncertainty

The uncertainty in the adiabatic effectiveness as determined with the IR method was accomplished by first evaluating the uncertainty in η_{app} and η_0 using the methods described in Ref. 33, since both quantities are based on direct temperature measurements or the calibrated IR measurement of the model surface. The majority of the test conditions examined in this study were set to T_∞ = 315 K and T_c = 295 K, where $\varepsilon_{T_\infty} = \varepsilon_{T_c}$ = 0.3 K and ε_{T_s} = 0.451 K. Since η_{app} and η_0 are not linear functions of the observed surface temperature, the uncertainties in η_{app} and

η_0 vary as the surface temperature varies between the coolant and freestream temperatures, but the maximum uncertainty in both parameters was observed at surface temperatures near either the coolant or the freestream temperature. This maximum uncertainty value, however, was dependent on the difference between the coolant and freestream temperatures, increasing as the difference decreased. Figure 3.17 shows the dependence of the uncertainty in the apparent adiabatic effectiveness as a function of the difference between the freestream and coolant temperatures. The 20 K difference that was utilized for the majority of this study resulted in $\varepsilon_{\eta_{app}}$ = 0.027. Furthermore, a 20 K difference between the coolant and freestream temperatures was used to determine the farfield η_0 distribution resulting in ε_{η_0} = 0.027 as well.

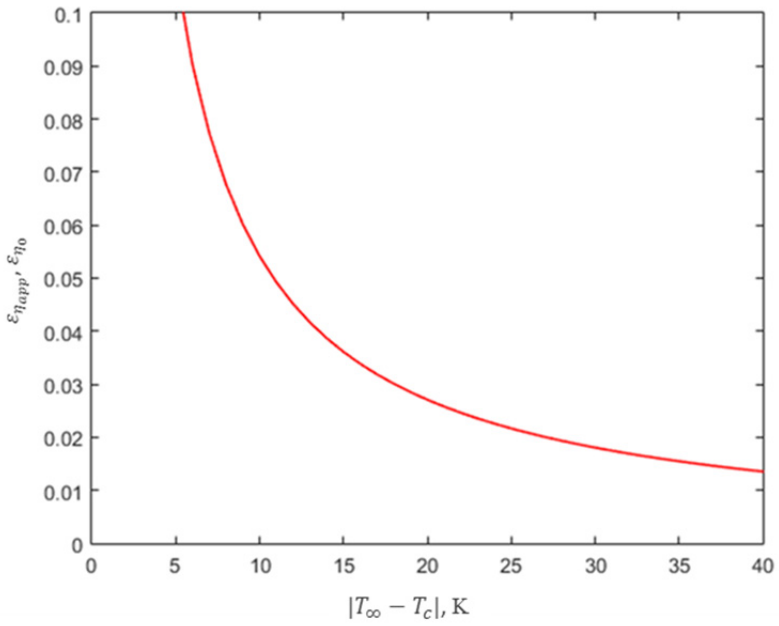

Figure 3.17. Dependence of $\varepsilon_{\eta_{app}}$ and ε_{η_0} on the quantity $|T_\infty - T_c|$

The uncertainties in η_0 and η_{app} were then used to evaluate an overall uncertainty in η based on application of Eq. (3.10) to Eq. (3.8) where η_{app} and η_0 were treated as measured quantities. The effects of the combined uncertainty is shown at x/d = 5 using air at M = 1.0 at T_∞ = 315 K and T_c = 290 K in Fig. 3.18. The overall uncertainty exhibited spatial variation,

shown in Fig. 3.19, reaching a values near ε_η = 0.04 at $y/d \leq$ -3 and $y/d \geq$ 0.5, while reaching values as low as $\varepsilon_{\eta_{IR}}$ = 0.032 near y/d = -1 This was a result of the increased influence of η_0 near regions of small η_{app}, while in regions with elevated η_{app}, such at -2 $\leq y/d \leq$ -1, the influence of η_0 is diminished. The influence of η_{app}, however, is near constant with respect to y/d, with slight variations due to spatial variation in η_0. The partial derivatives of η with respect to η_0 and η_{app} are shown in Fig. 3.20, where at $y/d \leq$ -3 and $y/d \geq$ 0.5 the absolute values of both partial derivatives are near unity and maximized, and since the uncertainties in η_0 and η_{app} were considered uniform, the overall uncertainty is maximized at these locations.

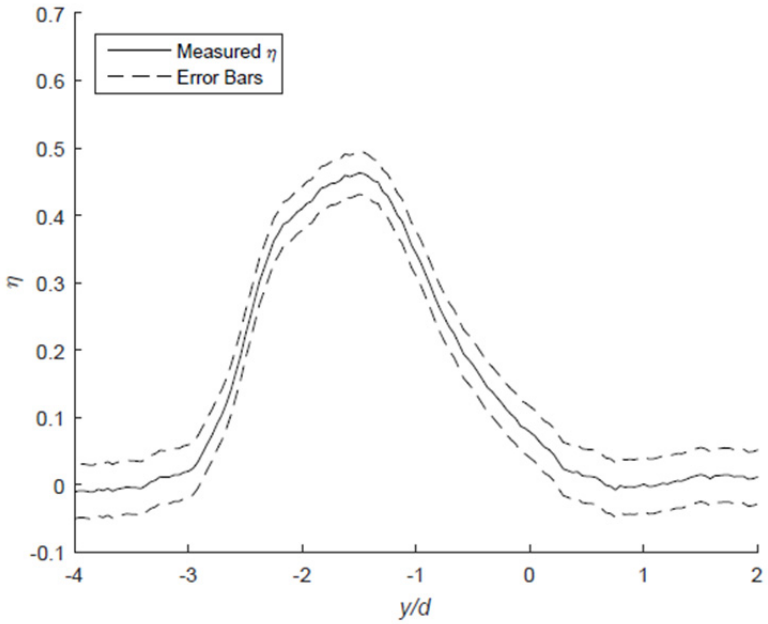

Figure 3.18. Uncertainty bands for air coolant, M = 1.0, x/d = 5.0, T_∞ = 315 K, T_c = 295 K, thermal technique

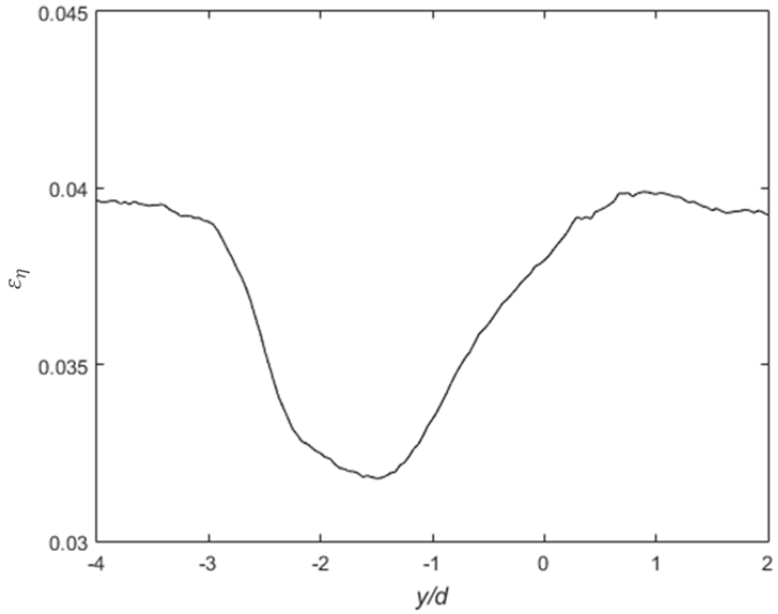

Figure 3.19. Spatial variation of ε_η for air coolant, M = 1.0, x/d = 5.0, T_∞ = 315 K, T_c = 295 K, thermal technique

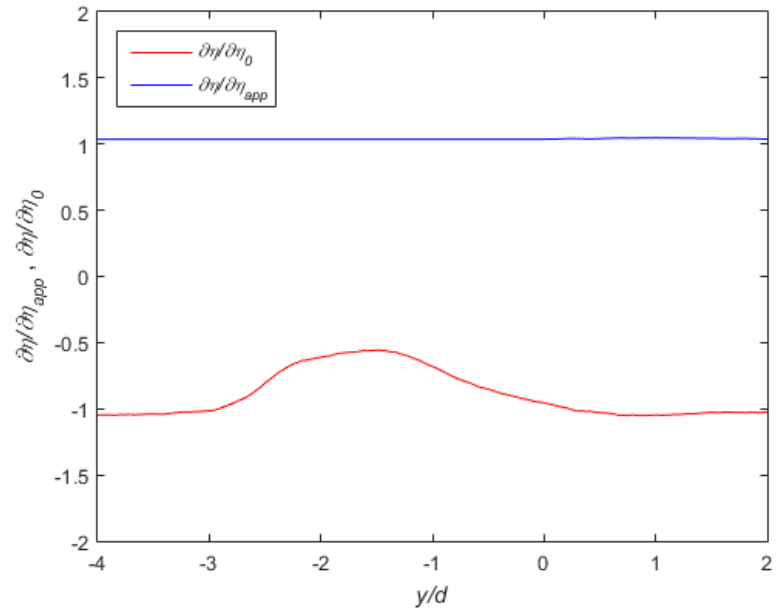

Figure 3.20. $\partial\eta/\partial\eta_{app}$ and $\partial\eta/\partial\eta_0$ for air coolant, M = 1.0, x/d = 5.0, T_∞ = 315 K, T_c = 295 K

The use of a single η_0 distribution, however, does provide the advantage that any measurement error in the η_0 distribution resulted in a bias error, rather than a randomly

distributed error. As a result, the observed repeatability of the adiabatic effectiveness provides a better characterization of the measurement uncertainty. The flow conditions used for repeatability characterization using the thermal method were air coolant at $T_c \approx 295$ K and $M \approx 1.0$ with $T_\infty \approx 315$ K. Seven cases were selected for repeatability evaluation. Cases were selected from four days of experimental testing. Table 3.6 shows the blowing ratios and peak adiabatic effectiveness values obtained during these cases, and the mean peak effectiveness, was observed to be 0.46 with a standard deviation, $\sigma_{\eta_{max}} = 0.01$. On a 95% confidence interval using a t-distribution, the repeatability was less than 0.02. The resultant profiles at $x/d = 5.0$ are shown in Fig 3.21. The peak effectiveness was selected as the repeatability parameter rather than an overall repeatability profile because slight shifts in the y location of the coolant jet would be characterized as regions of an over exaggerated reduced repeatability due to the large spatial gradients in η that occur away from the coolant peak.

Table 3.6. Thermal Repeatability Conditions

Case	Date	M	η_{max}
1	20150807	1.00	0.46
2	20150810	1.01	0.45
3	20150812	1.00	0.46
4	20151009	1.00	0.46
5	20150807	0.99	0.48
6	20150807	0.99	0.47
7	20151009	1.00	0.45

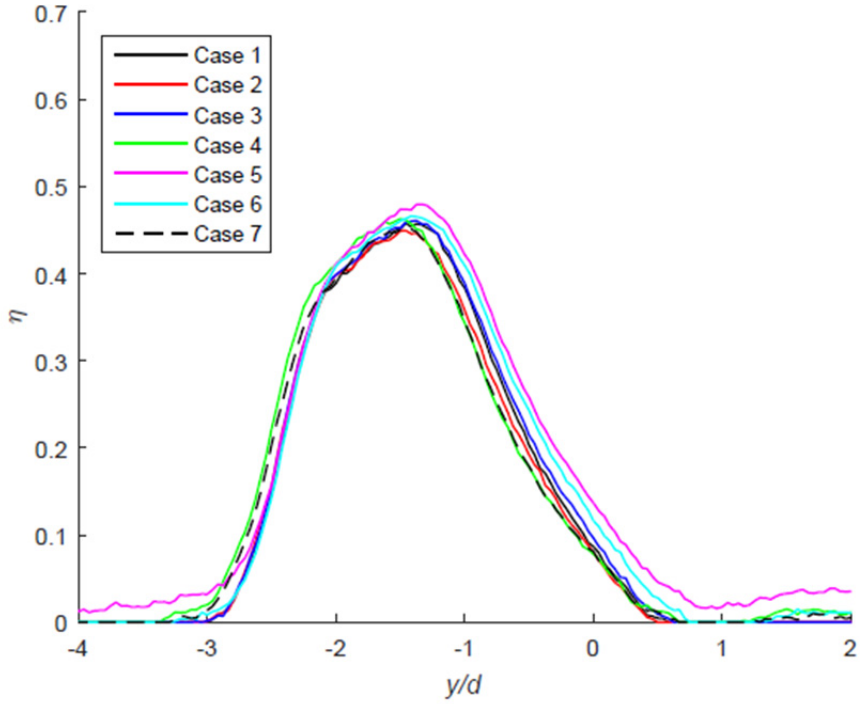

Figure 3.21. Spanwise adiabatic effectiveness profiles at x/d = 5.0 at repeatability conditions, thermal method

3.9.3 PSP Adiabatic Effectiveness Uncertainty

Uncertainty in the PSP technique was driven by the uncertainty in the partial pressure of O_2 measurements at the surface since the other variables in Eq. (2.22) were considered constant for each coolant gas in this study. However, the uncertainty in the pressure measurement is dependent on temperature gradients, illumination artifacts, and model motion. Use of a binary PSP, however, reduces the uncertainty due to temperature gradients to approximately 50 Pa/K [16], resulting in a maximum uncertainty of 1% in the pressure measurement due to temperature gradients in PSP portions of this study. Illumination artifacts are eliminated by characterizing the change in p_{O_2} in terms of an intensity ratio between the reference and experimental images. Model motion during a test was considered negligible due to the low aerodynamic loading on the symmetric leading edge model. In addition to the uncertainty sources as noted by Crafton, et al.

[16], a bias error was observed, likely due to photodegradation, over the course of testing, as one set of images was used as the reference condition, taken at the start of the test runs for a given day. As time progressed, and the model was exposed to illumination, the paint response uniformly decreased on the image, resulting in a uniformly increased observed pressure on the model surface. This bias was corrected by normalizing the observed pressure measurements in the vicinity of the coolant hole by the observed pressure measurements obtained from a region with no cooling gas and using that ratio as the independent variable in Eq. (2.22). The uncertainty in the adiabatic effectiveness measurement was achieved by determining the mean and standard deviation of the measured adiabatic effectiveness in a region with no film cooling. The mean adiabatic effectiveness measurement in this region was found to be approximately η = -0.005, and was consistent between cooling gases. The standard deviation, however, was found to be dependent on the cooling gas used, with CO_2 exhibiting the largest standard deviation in this region where σ_η = 0.019. Using a normal distribution and a 95% confidence interval, the uncertainty in η using PSP was determined to be $\varepsilon_{\eta_{PSP}}$ = 0.03 for all gases, recognizing the N_2 and Ar cooling gases produced lower farfield uncertainties, and likely have lower overall uncertainties. Figure 3.22 shows the measured effectiveness and uncertainty limits of the PSP measurement technique for N_2 coolant at $T_c \approx 295$ K and $T_\infty \approx 315$ K.

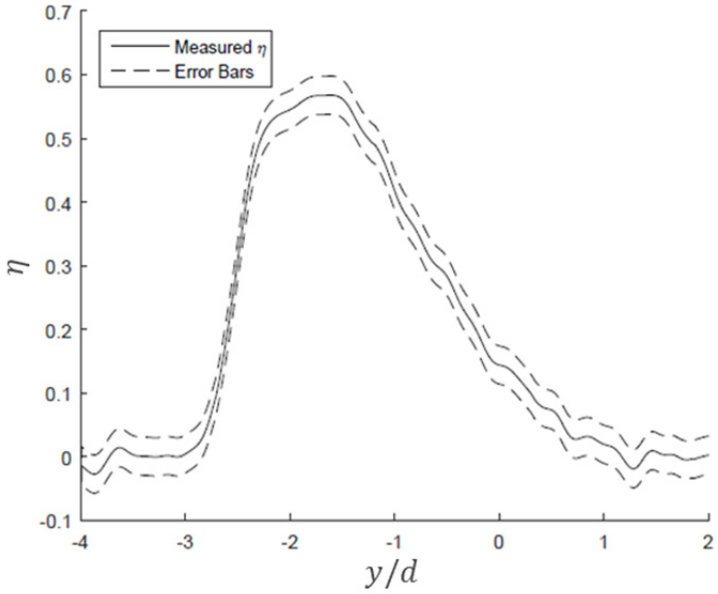

Figure 3.22. Uncertainty bands for N_2 coolant, M = 1.0, x/d = 5.0, T_∞ = 315 K, T_c = 295 K, PSP technique

PSP repeatability was established over two testing days with N_2 at flow rates within 2% of M = 1.0 with $T_c \approx$ 295 K and $T_\infty \approx$ 315 K. These cases were selected from matched flow rate parameter cases where M was near 1.0 for N_2. Table 3.7 shows the blowing ratios and resultant η_{max} values obtained during the repeatability runs, while Figure 3.23 shows the effectiveness profiles obtained at the repeatability conditions. The mean η_{max} was observed to be 0.55, with a standard deviation, $\sigma_{\eta_{max}}$ = 0.03, resulting in a repeatability of 0.06 with a 95% confidence interval. However, it should be noted that this repeatability condition represents a worst case, since all subsequent PSP data presented in this work was collected over the course of a single testing day (6 October) and the 95% confidence interval on 6 October was observed to be 0.02 with a mean peak effectiveness of 0.57. A possible source of this difference may have been the spatial calibration used for the 5 October cases. The implemented spatial calibration was a shifted version of the calibration used for 6 October, rather than a separate calibration, losing some fidelity in characterizing the surface curvature, which may have placed the x/d = 5.0 line

further downstream on 5 October than 6 October, resulting in a lower measured adiabatic effectiveness. Another possible source of this error could have been the experimental procedure used on 5 October where the reference image set was taken with the mainstream flow on, rather than off. This would have then not properly accounted for the pressure rise due to the flow over the model, decreasing the measured effectiveness.

Table 3.7. PSP Repeatability Conditions

Case	Date	M	η_{max}
1	20151005	1.00	0.53
2	20151005	1.01	0.53
3	20151006	1.00	0.57
4	20151006	1.02	0.58
5	20151006	1.02	0.59

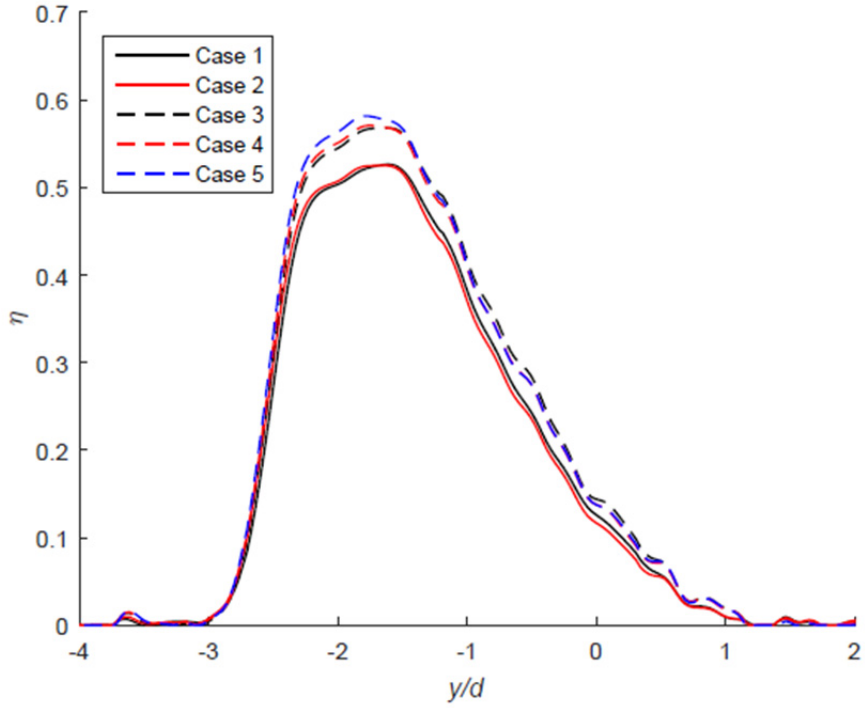

Figure 3.23. Spanwise adiabatic effectiveness profiles at x/d = 5.0 at repeatability conditions, PSP method

4. Results and Discussion

The purpose of this chapter is to present and discuss the results of the experiments performed in order to determine the influence of the coolant flow rate parameters on the adiabatic effectiveness distribution downstream of a single coolant hole and the comparisons between the thermal and PSP methodologies.

4.1 Influence of Coolant Flow Rate Parameters

The first objective of this research was to determine the influence of the various coolant flow rate parameters on the adiabatic effectiveness distribution. The coolant flow rate parameters that were considered included the conventional velocity ratio (VR), mass flux (blowing) ratio (M), and the momentum flux ratio (I), as well as the unconventional coolant flow rate parameters: Reynolds number ratio (ReR) and advective capacity ratio (ACR). For this initial investigation, the coolant and freestream were set to approximately 295 K and 315 K, respectively with a freestream Reynolds number of 60,000 at the low turbulence condition. The coolant-to-freestream property ratios at these conditions are shown in Table 4.1. Included in these property ratios are the density ratio, specific heat ratio, dynamic viscosity ratio, thermal conductivity ratio, and the ratio of binary diffusion coefficients. Commonly, these fluid properties are displayed in terms of the nondimensional diffusional transport parameters, the Prandtl, Schmidt, and Lewis numbers, shown in Table 4.2. With the exception of CO_2, the Lewis number is near unity, though the use of CO_2 is often justified in heat-mass transfer analogy experiments through the assumption that the turbulent Lewis number is near unity [14]. Each coolant flow rate parameter was evaluated at values on the range of 0.10-2.00 with both the IR and PSP techniques for each gas—with the exception of air when using the PSP method. Though the specific heats of the cooling and freestream gas have no influence on the mass transfer

processes, matched ACR experiments were performed with the PSP technique to evaluate the thermal decoupling effect of the PSP.

Table 4.1. Coolant-to-Freestream Property Ratios at T_∞ = 315 K and T_c = 295 K

Coolant	ρ_c/ρ_∞	$c_{P,c}/c_{P,\infty}$	μ_c/μ_∞	k_c/k_∞	$\mathcal{D}_{AB,c}/\mathcal{D}_{AB,\infty}$
Air	1.07	1.00	0.95	0.95	0.94
Ar	1.47	0.52	1.17	0.64	0.90
CO_2	1.62	0.83	0.77	0.60	0.76
N_2	1.03	1.03	0.92	0.94	0.94

Table 4.2. Diffusional Transport Parameters at T_∞ = 315 K and T_c = 295 K

Gas	Pr	Sc	Le
Freestream Air	0.71	0.76	1.08
Coolant Air	0.71	0.72	1.01
Ar	0.67	0.67	1.01
CO_2	0.76	0.47	0.62
N_2	0.71	0.72	1.01

4.1.1 General Flow Rate Effects

Prior to discussing the efficacy of the individual coolant flow rate parameters for scaling film cooling effectiveness, a discussion of the effect of the coolant flow rate is warranted. Since each of the coolant flow rate parameters of interest are monotonically increasing with the coolant flow rate, a sweep of a single coolant flow rate parameter with a single coolant gas is all that is necessary to provide a general overview of the cooling jet dynamics. For simplicity and brevity, the discussion of general flow rate effects will be based on the results from a blowing ratio sweep using air as the coolant. Table 4.3 shows the values of the coolant flow rate parameters included in these results while Figure 4.1 shows the effect of increasing the coolant flow rate. At the lowest flow rate condition (M = 0.1, Fig. 4.1a), the coolant jet escaped the coolant channel and spilled onto the model surface in two distinct regions of elevated adiabatic effectiveness,

while little effectiveness was observed near y/d = 0. Increasing the flow rate to M = 0.25 (Fig. 4.1b), resulted in a second flow pattern wherein a region of elevated effectiveness was observed at y/d > 0 and a series of smaller regions of elevated cooling effectiveness—known as effectiveness "fingers"—was observed at y/d < 0. Increasing the flow rate further to M = 0.50 (Fig. 4.1c) resulted in a single major region of elevated effectiveness centered near y/d = 0. The collapsing of the elevated effectiveness region to a single major region immediately downstream of the coolant hole rather than a series of effectiveness "fingers" was considered to be the criterion for classifying a coolant jet as fully developed. For simplicity sake, fully developed jets were primarily considered for comparison purposes.

Further increases in the coolant flow rate (Fig. 4.1d-f), resulted in further penetration by the coolant jet in the -y/d direction due to the higher jet momentum relative to the freestream. This increase in momentum also eventually leads to separation of the coolant jet wherein the cooling jet is primarily ejected into the freestream flow, rather than laying back onto the model surface. Determining when the coolant jet is separated from the model surface, however, is difficult without characterizing the velocity field near the coolant hole, which was outside the scope of this study.

Table 4.3. Coolant Flow Rate Parameters for Air *M* Sweep

M	I	VR	ACR	ReR
0.10	0.01	0.09	0.10	0.11
0.25	0.06	0.24	0.25	0.27
0.50	0.23	0.47	0.50	0.52
1.00	0.94	0.94	1.00	1.05
1.50	2.09	1.40	1.50	1.58
2.00	3.68	1.84	2.00	2.12

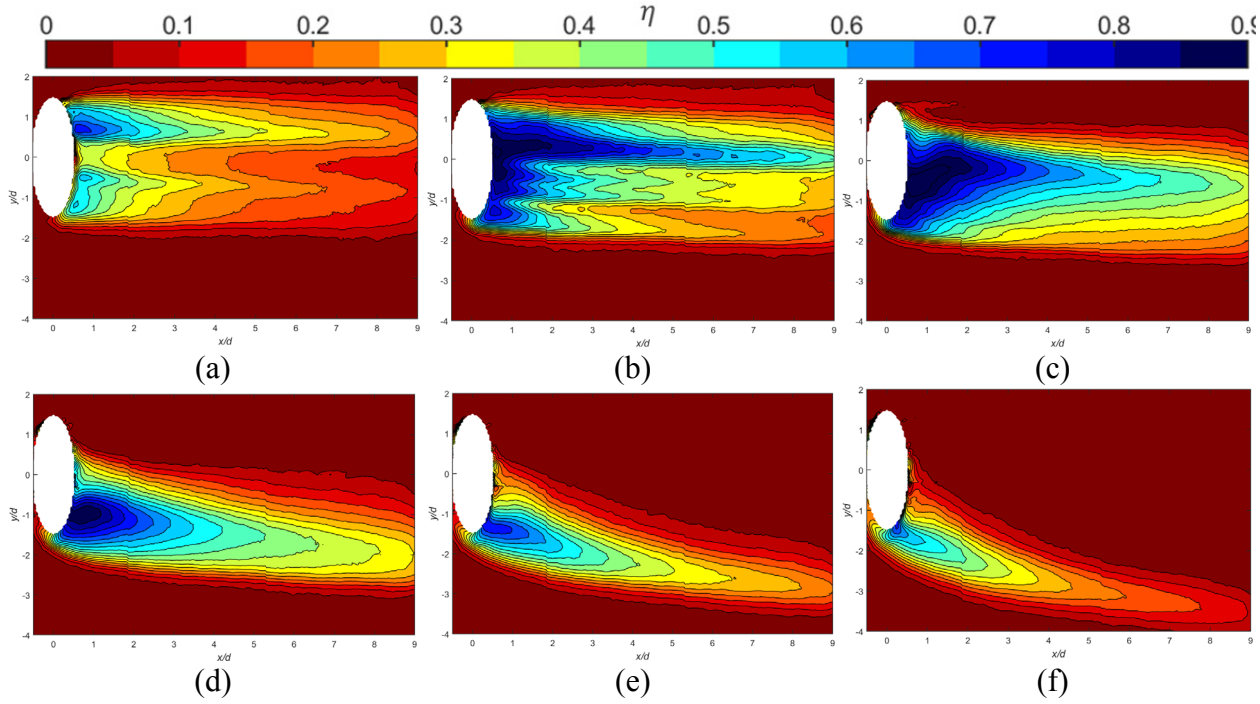

Figure 4.1. General influence of coolant flow rate on adiabatic effectiveness distributions: air at M = (a) 0.10, (b) 0.25, (c) 0.50, (d) 1.00, (e) 1.50, (f) 2.00, IR technique

4.1.2 Velocity Ratio

The first coolant flow rate parameter of interest was the simple velocity ratio, VR. VR characterizes the volumetric flux of the coolant relative to the freestream. As a result, no account is made for mass or momentum flux relative to the freestream since DR is not accounted for. Fully developed jets were first observed with each cooling gas at VR = 0.5—with coolant flow rate parameter values tabulated in Table 4.4 and results shown in Fig. 4.2 for the IR and PSP techniques.

At these flow conditions, the air and N_2 jets produce similar effectiveness contours when evaluated using the IR technique, though this agreement was expected since all relevant flow parameters are essentially matched when using air and N_2 coolants. The dense Ar and CO_2 coolant jets, however, produce significantly different η distributions when compared to the air

and N_2 jets. This, too, was expected since Thole et al. [18] showed that VR did not properly scale thermal fields downstream of a coolant hole with respect to DR. When evaluated with the PSP technique, each gas produced a similarly shaped η distribution to its IR complement, though with a greater effectiveness magnitude, the possible sources of which are discussed in Section 4.2. Furthermore, the CO_2 profile appeared to exhibit a small secondary region of elevated effectiveness, beginning at approximately x/d = 2.0 indicating that a small column of CO_2 had split from the main jet. This second column of CO_2 was not readily apparent in the IR data, though at 2.0 ≤ x/d ≤ 4.0, $\partial\eta/\partial y$ approached zero at approximately y/d = -1 indicating that this secondary column may be interacting thermally with the freestream more than the main column. This phenomenon is more evident in Fig. 4.3 which shows the spanwise effectiveness profiles for the IR and PSP experiments for each gas at x/d = 5.0. At this location, the PSP experiment yielded greater effectiveness results than the corresponding IR experiment for each gas, though similar profile shapes were observed between experiments when comparing like gas conditions, with the exception of CO_2 where the PSP experiment showed a second effectiveness peak further in the -y/d direction than the primary peak.

Table 4.4. Coolant Flow Rate Parameters at VR = 0.5

	Thermal					PSP				
Coolant	M	I	$\boldsymbol{VR}$	ReR	ACR	M	I	$\boldsymbol{VR}$	ReR	ACR
Ar	0.74	0.37	**0.50**	0.63	0.38	0.73	0.37	**0.50**	0.62	0.38
CO_2	0.82	0.42	**0.51**	1.07	0.69	0.82	0.40	**0.51**	1.04	0.67
N_2	0.52	0.26	**0.50**	0.56	0.53	0.51	0.26	**0.50**	0.55	0.53
Air	0.54	0.27	**0.51**	0.57	0.54	--	--	--	--	--

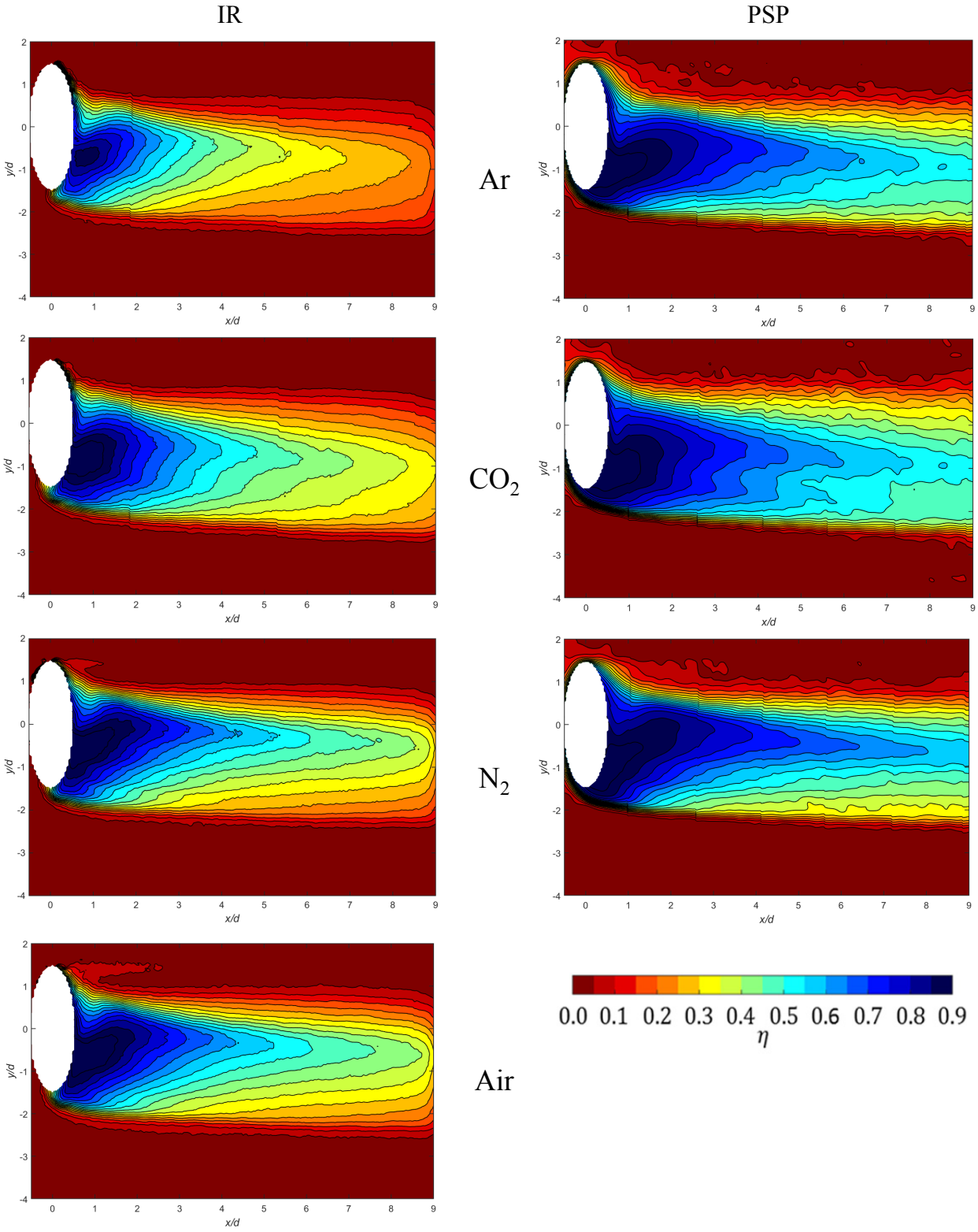

Figure 4.2. Adiabatic effectiveness contours at VR = 0.5, IR (Left) and PSP (Right) methods

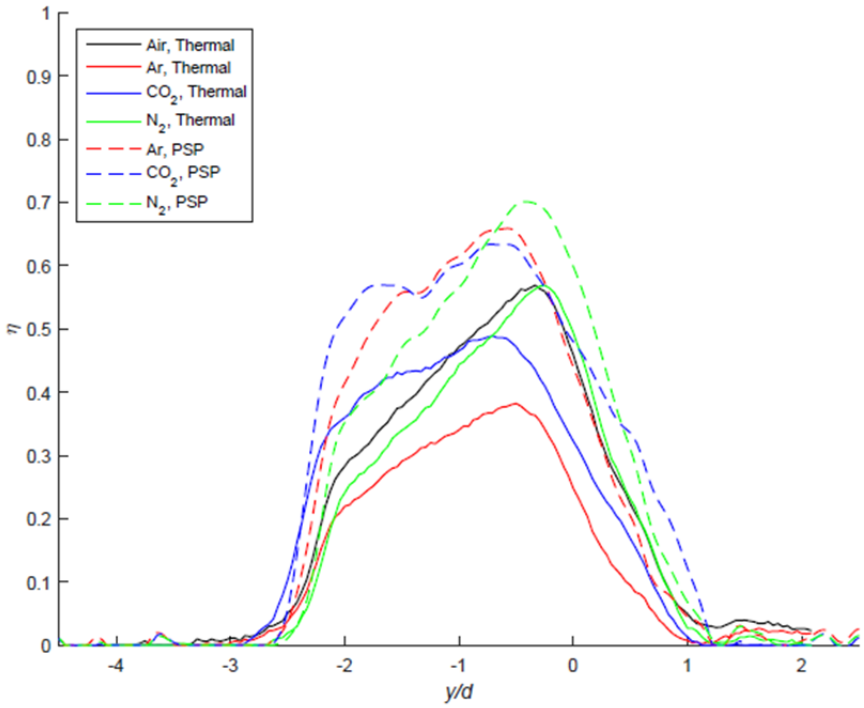

Figure 4.3. Spanwise adiabatic effectiveness profiles at x/d = 5.0, VR = 0.5

Increasing the coolant flow rate to correspond to VR = 1.0 resulted in the coolant flow rate parameter values tabulated in Table 4.5 and the effectiveness profiles shown in Fig. 4.4. Like the VR = 0.5 case, the air and N_2 coolant jets produced similar effectiveness profiles when evaluated with the IR method, though with a lesser effectiveness magnitude than that of the PSP case with a N_2 jet. Furthermore, the only profile agreement between gases at these conditions is between air and N_2—shown in greater detail in Fig. 4.5. The disagreement between gases is likely due to the increased momentum flux of the jet, which at VR = 1.0, I takes the value of the jet DR. As a result, the jets arrange themselves in terms of DR where the jet with the greatest DR (CO_2) penetrated furthest in the -y/d location, followed by the Ar, N_2, and air jets. In addition, when comparing the CO_2 jet between the two experimental techniques, the PSP method shows a sharper peak—one that has a higher concavity—compared to the IR method. This peak was also observed to be further in the -y/d direction than that of the IR method, indicating that perhaps

the coolant jet itself penetrates further in the $-y/d$ direction than its thermal effect. Possible explanations for this apparent "lag" in the temperature profile will be discussed in Section 4.2. Based on the lack of agreement between cooling effectiveness profile shapes and locations at matched velocity ratio conditions, VR was determined to be an ineffective parameter for scaling the placement of the coolant jet effectiveness region downstream of the coolant hole.

Table 4.5. Coolant Flow Rate Parameters at $\boldsymbol{VR}$ = 1.0

	Thermal					PSP				
Coolant	M	I	$\boldsymbol{VR}$	ReR	ACR	M	I	$\boldsymbol{VR}$	ReR	ACR
Ar	1.48	1.49	**1.00**	1.28	0.77	1.45	1.45	**1.00**	1.24	0.75
CO_2	1.63	1.63	**1.00**	2.13	1.36	1.62	1.63	**1.00**	2.11	1.36
N_2	1.03	1.03	**1.00**	1.13	1.07	1.02	1.02	**1.00**	1.11	1.06
Air	1.07	1.07	**1.00**	1.13	1.07	--	--	--	--	--

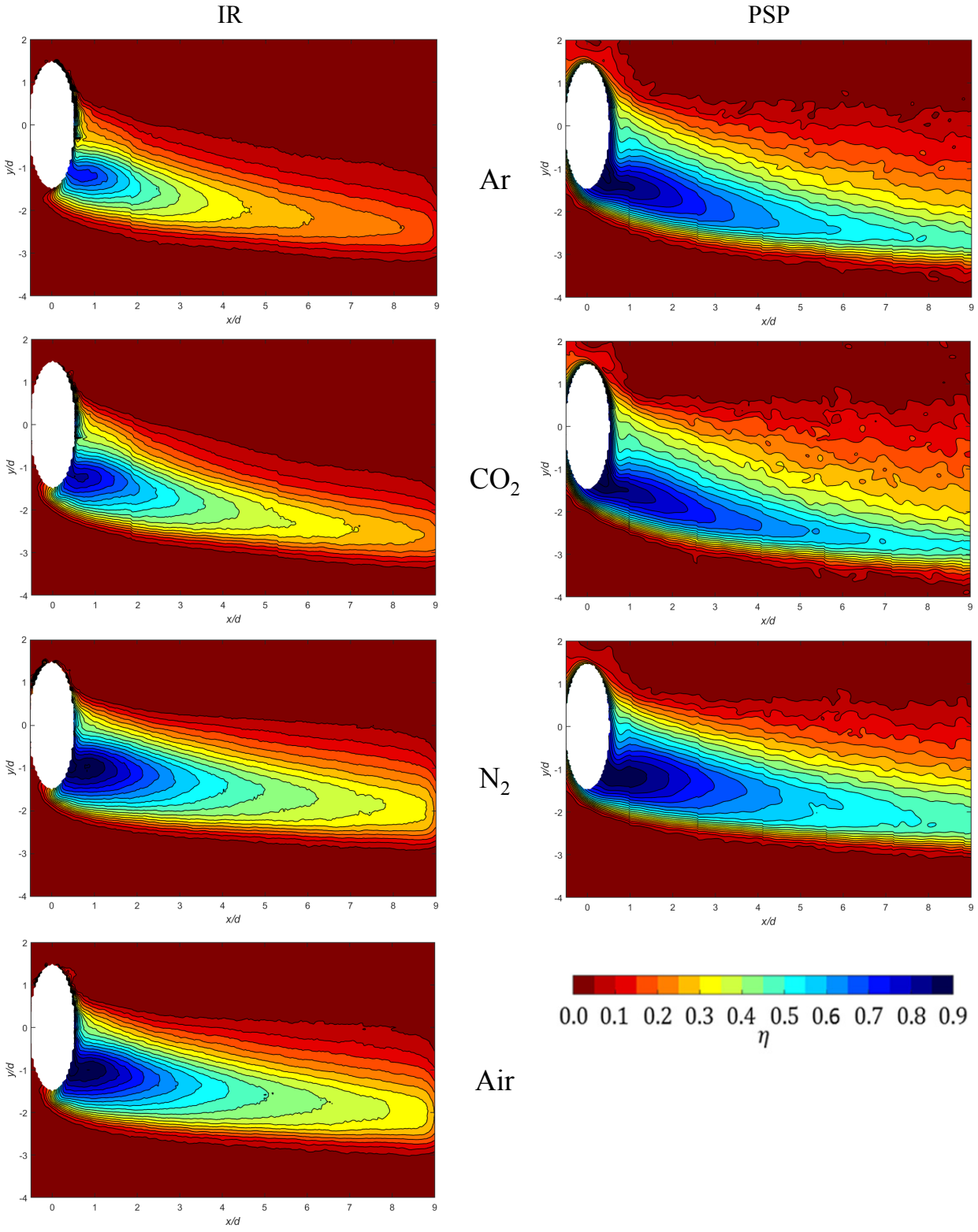

Figure 4.4. Adiabatic effectiveness contours at VR = 1.0, IR (Left) and PSP (Right) methods

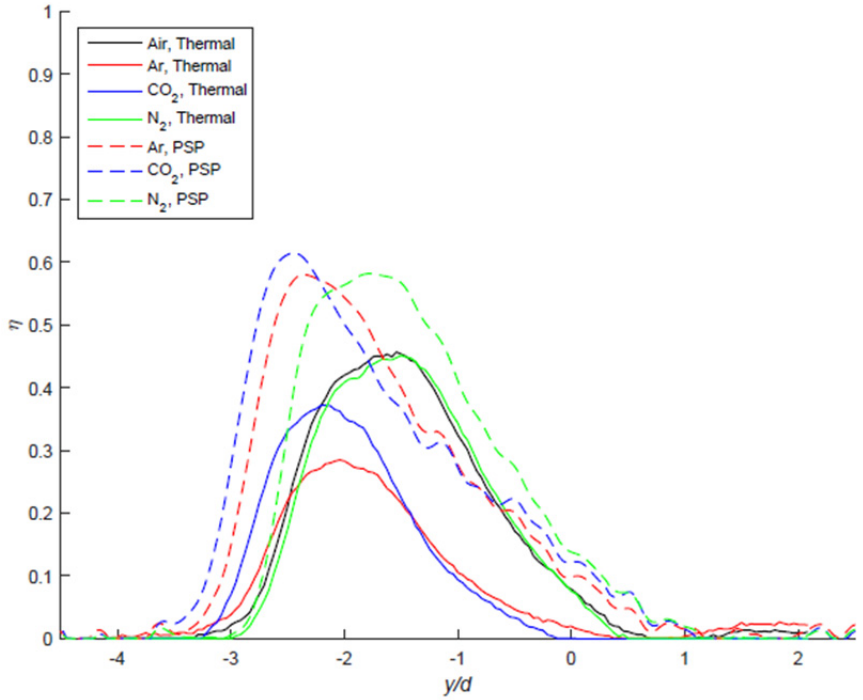

Figure 4.5. Spanwise adiabatic effectiveness profiles at x/d = 5.0, VR = 1.0

4.1.3 Mass Flux Ratio

Unlike VR, the mass flux, or blowing, ratio accounts for the mass flux of the coolant jet relative to the freestream. Each coolant jet was considered developed at M = 0.5, though the Ar and CO_2 jets were near the edge of this classification, and the full suite of coolant flow rate parameters are tabulated in Table 4.6 with the effectiveness contours displayed in Fig. 4.6.

Table 4.6. Coolant Flow Rate Parameters at M = 0.5

	Thermal					PSP				
Coolant	***M***	*I*	*VR*	*ReR*	*ACR*	***M***	*I*	*VR*	*ReR*	*ACR*
Ar	**0.50**	0.17	0.34	0.43	0.26	**0.50**	0.17	0.35	0.43	0.26
CO_2	**0.50**	0.16	0.31	0.65	0.42	**0.50**	0.15	0.31	0.64	0.42
N_2	**0.50**	0.24	0.48	0.55	0.52	**0.50**	0.25	0.49	0.55	0.52
Air	**0.50**	0.23	0.47	0.52	0.50	--	--	--	--	--

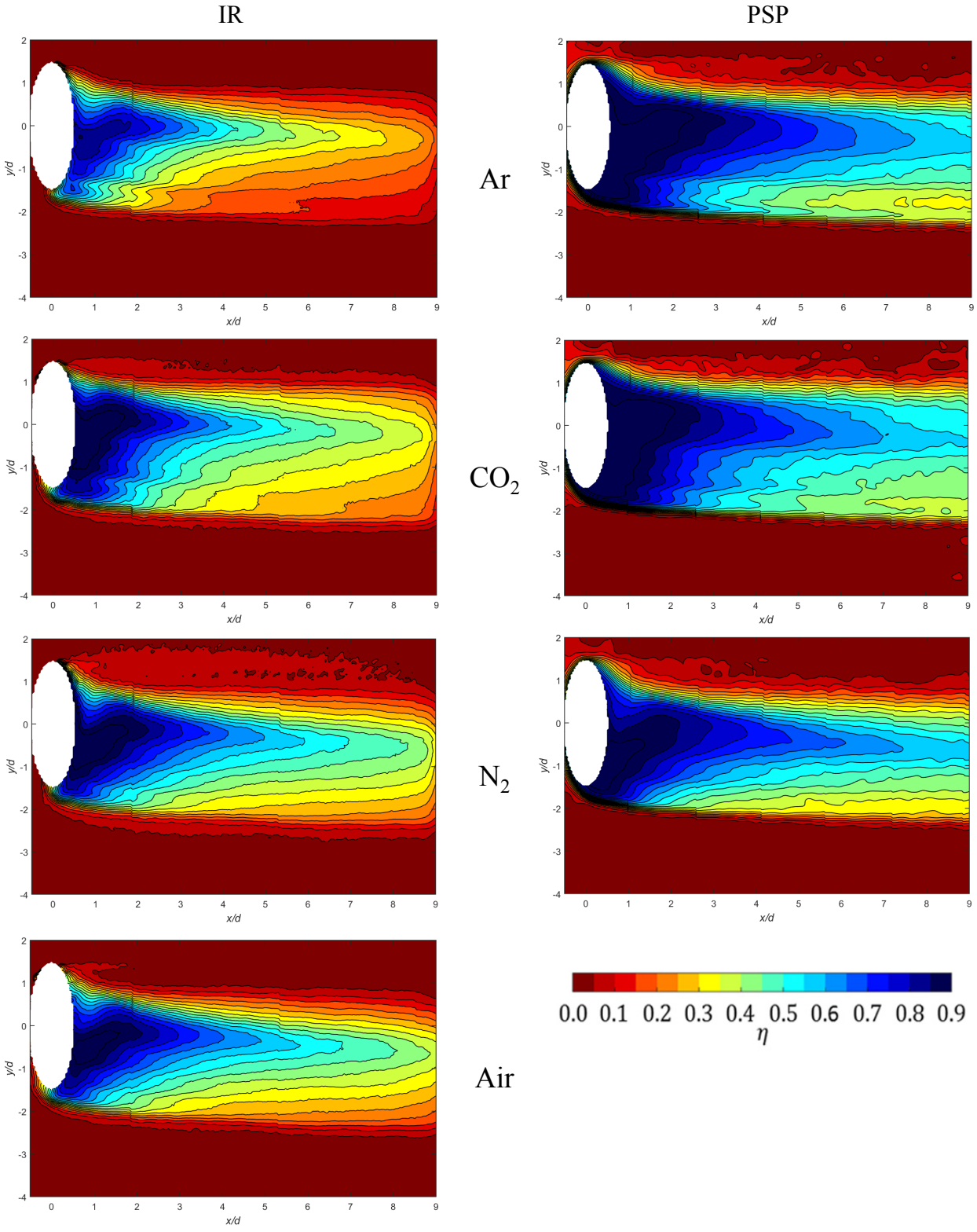

Figure 4.6. Adiabatic effectiveness contours at *M* = 0.5, IR (Left) and PSP (Right) methods

When employing the IR method, the Ar and CO_2 cooling jets produce similar profiles, but the effectiveness magnitude for the Ar jet is subdued compared to the CO_2 jet. Likewise, the Air and N_2 jets produce similar effectiveness profile shapes and magnitudes, with the exception of an artifact of the boundary layer correction $y/d \geq 1.0$. When comparing effectiveness profiles obtained from the PSP method to their IR counterparts, the Ar and CO_2 jets exhibit flow features that are not readily apparent in the IR measurements. First and foremost, both jets exhibit a local adiabatic effectiveness maxima at approximately y/d = -2—the subdued influence of this maxima can be seen in both Ar and CO_2 IR results. Furthermore, the primary coolant column—the region centered around y/d = 0.0—for the Ar case maintained a greater effectiveness downstream than the CO_2 jet while the opposite was observed when evaluated with the IR technique.

Figure 4.7 shows the spanwise adiabatic effectiveness distributions at M = 0.5 conditions at x/d = 5.0. Both the IR and PSP experiments indicate a separation of the coolant flows into two groups: one with air and N_2 producing similar results and a second with Ar and CO_2. When evaluated with PSP, the N_2 jet exhibited greater effectiveness than the IR measurements, though the profile shapes remained similar between the two experimental techniques at each point downstream of the coolant hole. The CO_2 and Ar group exhibited similar profile shapes, though the Ar jet produced lower effectiveness than CO_2 when evaluated with the IR technique and slightly greater effectiveness in the primary region of elevated effectiveness region when evaluated with PSP. Furthermore, the effectiveness finger discussed previously was observable at approximately y/d = -2.0 for both gases using the PSP technique.

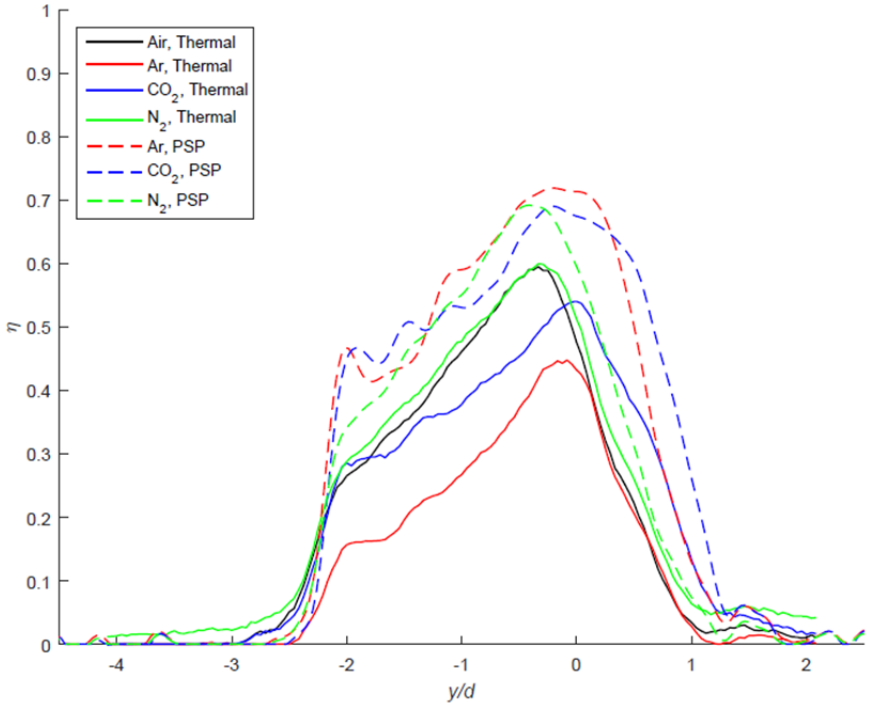

Figure 4.7. Spanwise adiabatic effectiveness profiles at x/d = 5.0, M = 0.5

The separation of the coolant gases into two groups was likely a result of the momentum flux ratios obtained at these conditions. When M = 0.5, N_2 and air exhibit momentum flux ratios near 0.24 while the Ar and CO_2 jets maintained momentum flux ratios of approximately 0.16. Based on the similarity between Ar and CO_2 in terms of both M and I at these conditions, the differences in effectiveness magnitude can likely be attributed to either the disparity in ReR or ACR, both of which CO_2 maintained a greater value. The elevated ACR of the CO_2 jet would likely lead to greater η magnitude because the CO_2 jet can absorb more thermal energy from the freestream before heating up compared to the Ar jet.

Increasing the coolant flow rates to M = 1.0 resulted in the coolant flow rate parameter values tabulated in Table 4.7 and the η distributions shown in Fig. 4.8. In terms of shape and dominant flow features, Ar and CO_2 exhibit similar profiles, though the cooling effectiveness magnitude for the Ar jet was reduced compared to the CO_2 jet in both evaluation techniques,

though the effectiveness as obtained through IR measurements was subdued to a greater degree than the PSP test. Again, the trend of additional visible flow features flow features that appear when using the PSP technique was apparent with the bifurcation of the coolant trace in both the Ar and CO_2 jets. This bifurcation is shown in greater detail in Fig. 4.90 where the secondary region of elevated effectiveness Ar and CO_2 jets is apparent, resulting in a second local effectiveness maxima near y/d = -2. Furthermore, the separation of the coolant jet profiles into two groups is more readily visible with the air and N_2 jets positioned with their maximum effectiveness centered around y/d = -1.5, while the Ar and CO_2 jets produce wider jets with effectiveness peaks located at approximately y/d = -1.0. Like the M = 0.5 cases, this binary grouping was likely due to the relatively matched I values within the two gas groupings where the higher momentum (air and N_2) jets produce thinner jets located further in the -y/d direction than the lower momentum jets.

Table 4.7. Coolant Flow Rate Parameters at M = 1.0

	Thermal					PSP				
Coolant	$\boldsymbol{M}$	I	VR	ReR	ACR	$\boldsymbol{M}$	I	VR	ReR	ACR
Ar	**0.99**	0.67	0.68	0.85	0.51	**1.00**	0.68	0.68	0.85	0.52
CO_2	**1.00**	0.62	0.62	1.31	0.84	**1.00**	0.62	0.62	1.29	0.84
N_2	**1.00**	0.97	0.97	1.09	1.04	**1.00**	0.97	0.97	1.09	1.03
Air	**1.00**	0.94	0.94	1.05	1.00	--	--	--	--	--

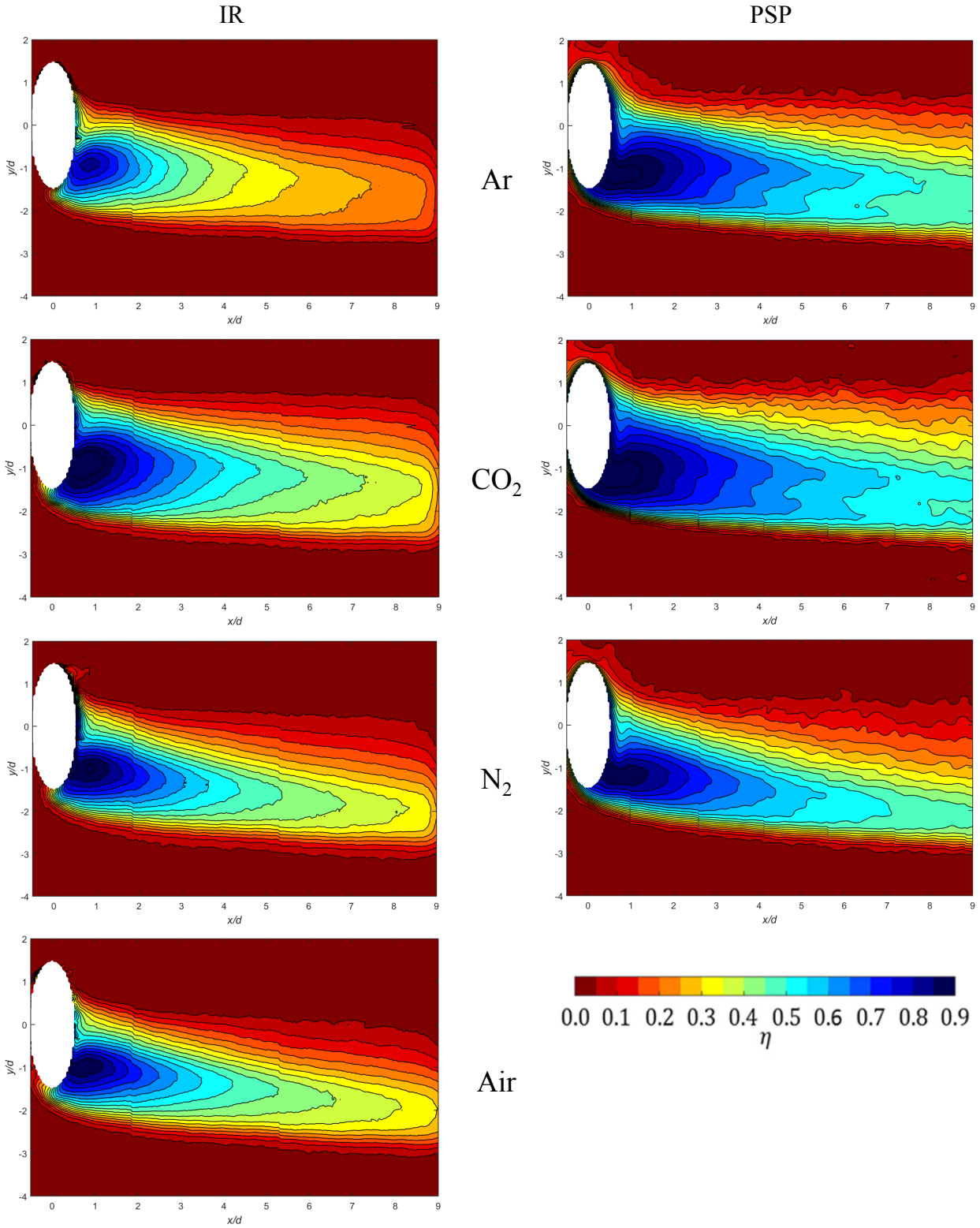

Figure 4.8. Adiabatic effectiveness contours at *M* = 1.0, IR (Left) and PSP (Right) methods

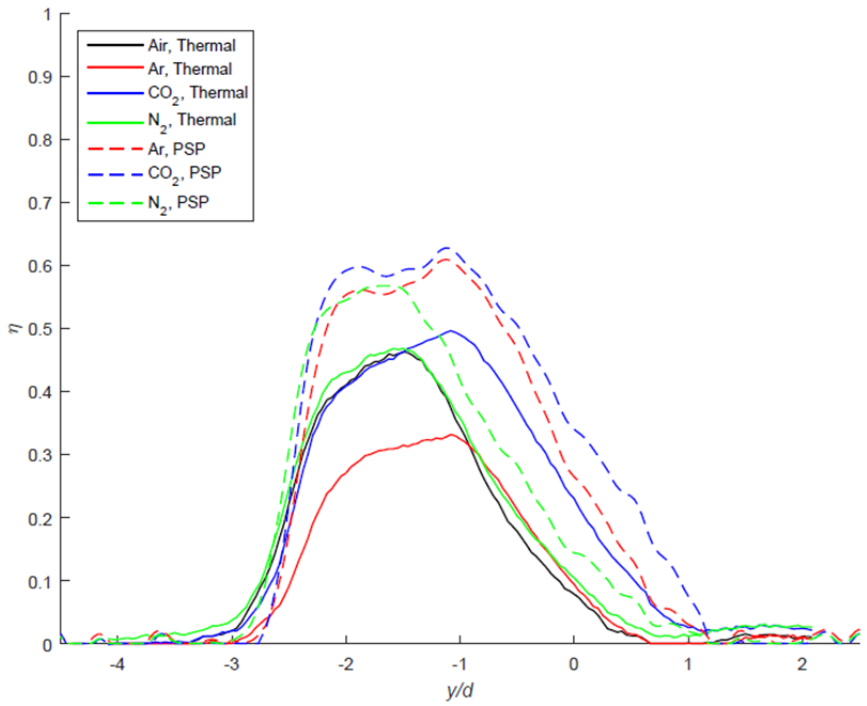

Figure 4.9. Spanwise adiabatic effectiveness profiles at x/d = 5.0, M = 1.0

Further increases in coolant flow rate to M = 2.0 resulted in the coolant flow rate parameters shown in Table 4.8 and the effectiveness contours shown in Fig. 4.1. At these flow rates, each gas produces a thin primary effectiveness region when compared to the M = 1.0 case. Furthermore, the jets are further displaced in the -y/d direction. The thin, displaced jets indicate that at these conditions, the jets are primarily lifting off of the model surface and ejecting into the freestream. The effectiveness contours observed with the PSP method, however, show a large region of relatively shallow adiabatic effectiveness gradients when compared to the IR measurements above the primary coolant trace. This effectiveness gradient is likely the result of a thin layer of anaerobic coolant gas that rapidly warms as it travels downstream. Examination of the spanwise effectiveness distributions shown in Fig. 4.11 indicates a phenomenon that is not obvious when examining the effectiveness contours: that the spanwise peak effectiveness

location is uniformly further in the $-y/d$ direction when evaluating a gas using PSP regardless of the cooling gas used. The difference in effectiveness peak location further indicates that a diffusional process is not visible when using the PSP technique, or rather, that IR measurements are influenced by additional diffusion processes resulting in subdued apparent jet displacement and cooling effectiveness.

Table 4.8. Coolant Flow Rate Parameters at M = 2.0

	Thermal					PSP				
Coolant	$\boldsymbol{M}$	I	VR	ReR	ACR	$\boldsymbol{M}$	I	VR	ReR	ACR
Ar	**2.00**	2.71	1.35	1.72	1.04	**2.00**	2.72	1.36	1.72	1.04
CO_2	**2.00**	2.44	1.22	2.62	1.67	**2.01**	2.48	1.24	2.61	1.68
N_2	**2.00**	3.84	1.92	2.19	2.06	**2.00**	3.87	1.93	2.18	2.07
Air	**2.00**	3.68	1.84	2.12	2.00	--	--	--	--	--

Despite the good agreement between the Ar and CO_2 cases in terms of profile shape and location, M was found to exhibit poor scaling performance when comparing Ar and CO_2 to the air and N_2 cases. The disagreement between the elevated density jets and the near unity density jets was likely due to the disparity in the jet momentum fluxes where the near unity jets maintained an elevated momentum flux ratio; resulting in thinner jets that were displaced further in the $-y/d$ direction. Furthermore, when examining the Ar and CO_2 jets using the thermal method, the Ar jet exhibited lower effectiveness magnitude at each flow rate condition.

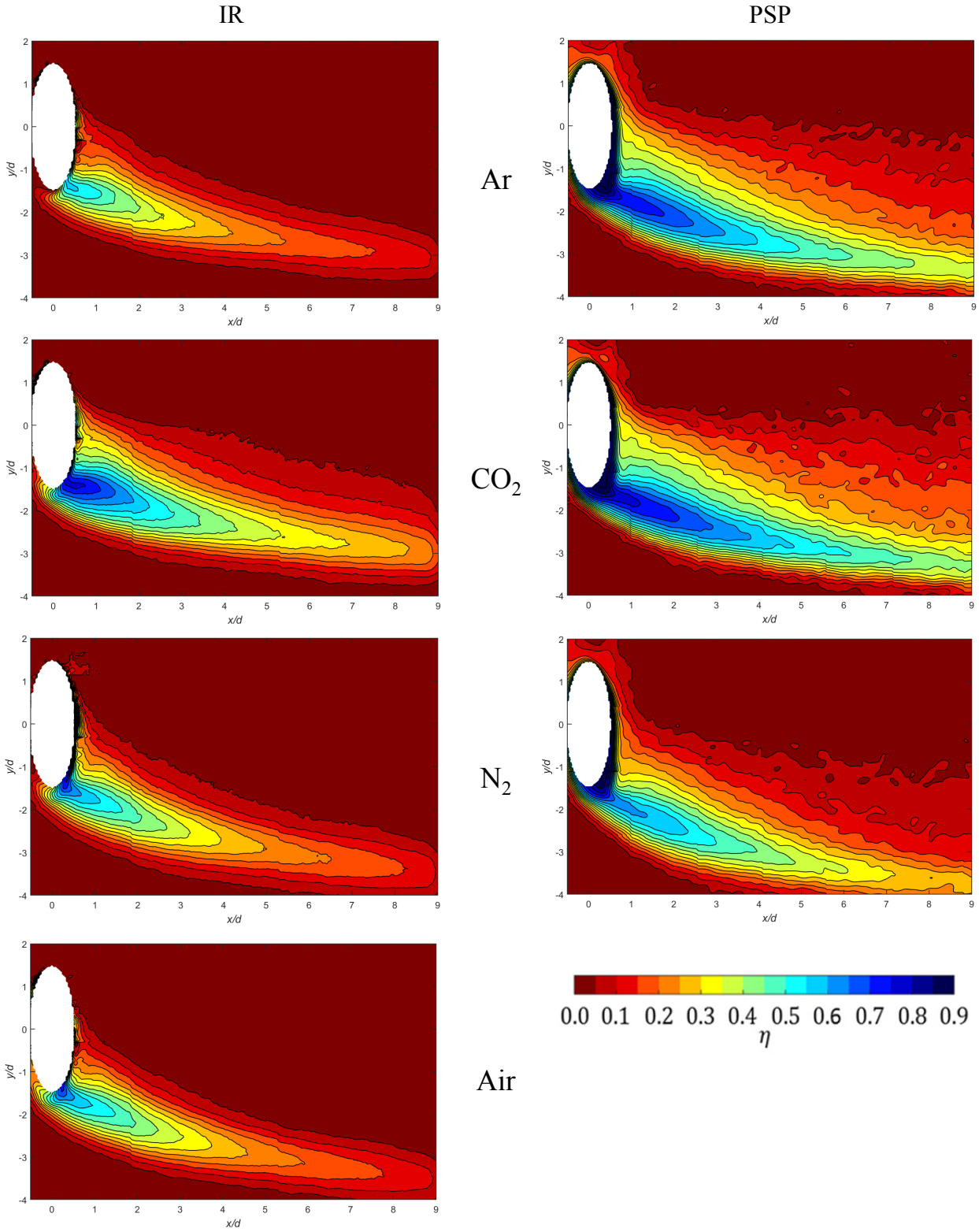

Figure 4.10. Adiabatic effectiveness contours at M = 2.0, IR (Left) and PSP (Right) methods

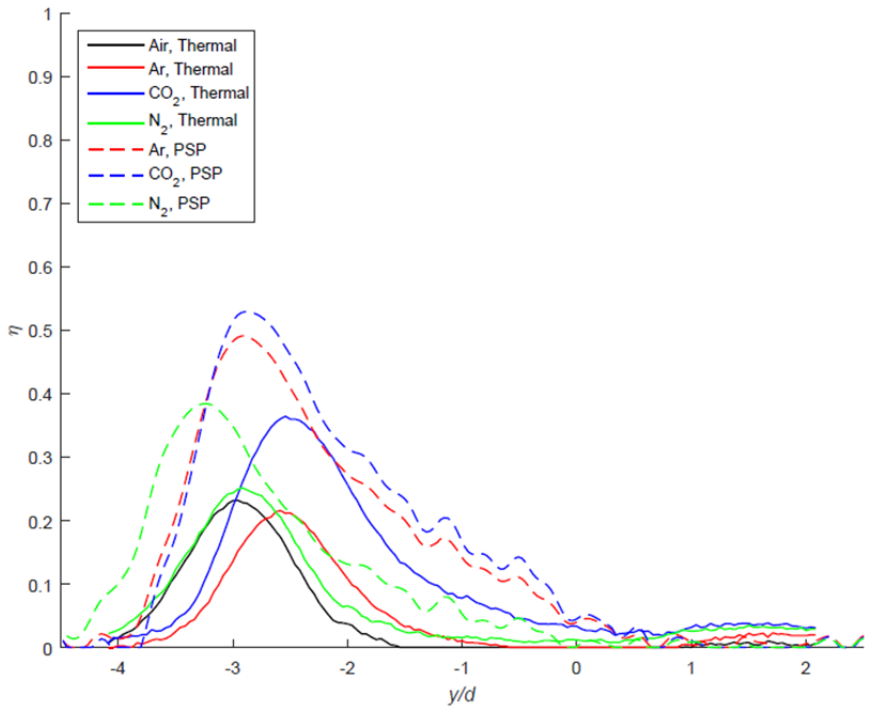

Figure 4.11. Spanwise adiabatic effectiveness profiles at x/d = 5.0, M = 2.0

4.1.4 Momentum Flux Ratio

Based on the observed similarity in effectiveness contours at near-matched I conditions during matched M experimentation, matched I conditions were explored with each gas. Each gas exhibited a fully developed effectiveness profile with $I \geq 0.25$ and the resultant coolant flow rate parameters and effectiveness profiles are shown in Table 4.9 and Fig. 4.12 respectively. At these conditions, the effectiveness profile shapes were similar between Ar, N_2, and air, while the CO_2 profile exhibited some key differences—but was more comparable to the other coolants than was observed by matching other flow rate conditions. The first key difference was that the CO_2 effectiveness profile appeared to bifurcate when evaluated using the PSP technique. Furthermore, the magnitude of $\partial\eta/\partial y$ at -1.0 ≤ y/d ≤ -0.5 was lower than any of the other gases shown in Fig. 4.12, particularly when the thermal technique was applied. The spanwise effectiveness profiles shown in Fig. 4.13 show the similarity between the Ar, N_2, and air

effectiveness profiles, while the CO_2 profile exhibited the characteristics of a bifurcated coolant jet. The differences in profile shape may have been a result of the coolant Reynolds number since the CO_2 jet maintained $ReR \approx 0.83$ at these flow conditions while the other jets maintained $ReR \approx 0.53$. Furthermore, the Ar jet exhibited a lower effectiveness magnitude than either the N_2 or air jets when evaluated with the thermal technique, likely due to the influence of the reduced ACR value since ReR was near matched at these flow conditions and has little bearing on the ability of a coolant to transport thermal energy.

Table 4.9. Coolant Flow Rate Parameters at I = 0.25

	Thermal					PSP				
Coolant	M	$\boldsymbol{I}$	VR	ReR	ACR	M	$\boldsymbol{I}$	VR	ReR	ACR
Ar	0.61	**0.25**	0.41	0.52	0.32	0.60	**0.25**	0.41	0.52	0.31
CO_2	0.64	**0.26**	0.40	0.84	0.54	0.64	**0.25**	0.40	0.83	0.54
N_2	0.51	**0.25**	0.49	0.55	0.53	0.50	**0.25**	0.49	0.55	0.52
Air	0.51	**0.25**	0.48	0.54	0.51	--	--	--	--	--

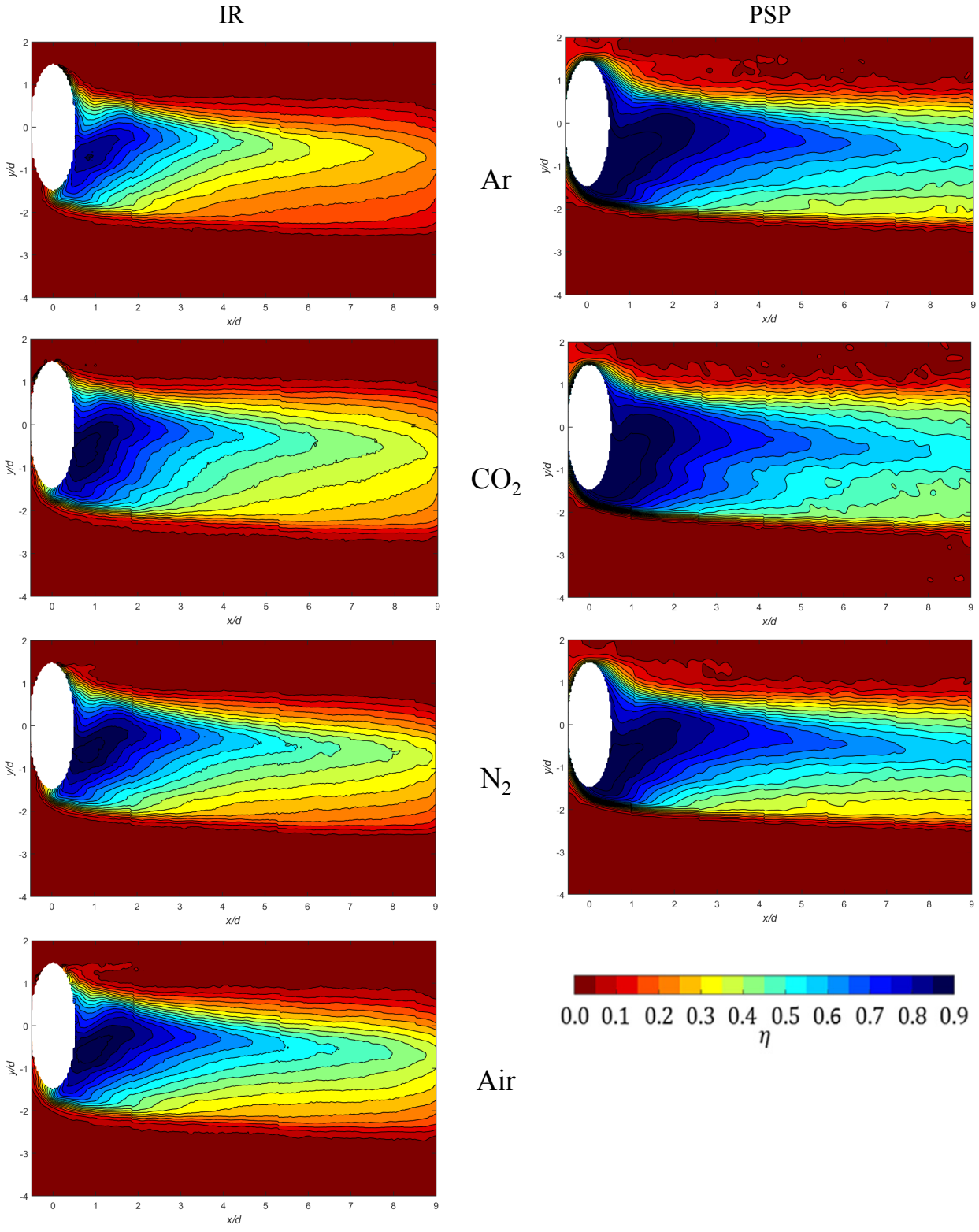

Figure 4.12. Adiabatic effectiveness contours at I = 0.25, IR (Left) and PSP (Right) methods

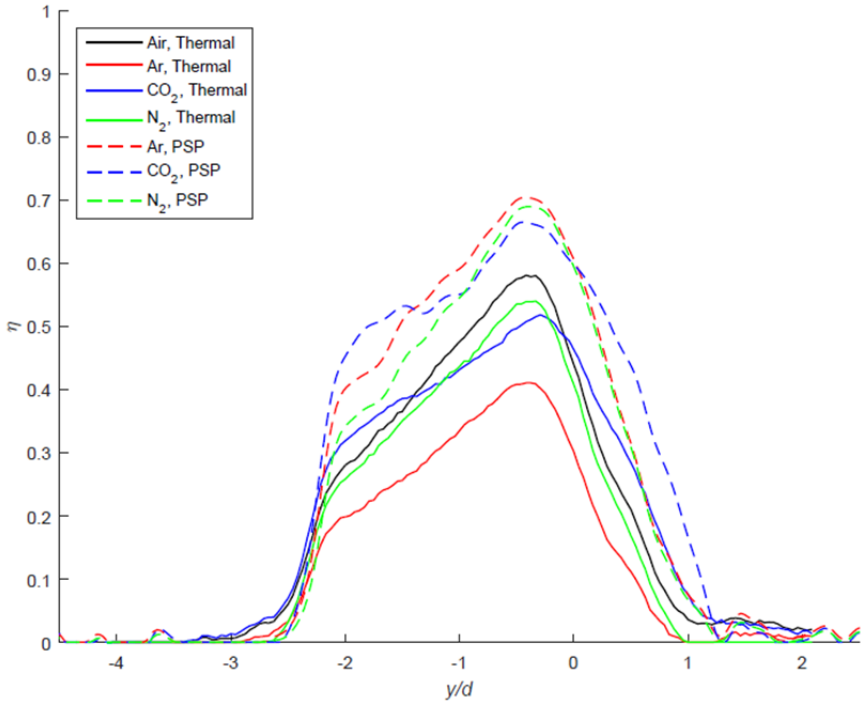

Figure 4.13. Spanwise adiabatic effectiveness profiles at x/d = 5.0, I = 0.25

Increasing the momentum flux to I = 0.5 resulted in the coolant flow rate parameter values tabulated in Table 4.10 and the effectiveness profiles shown in Fig. 4.14. At these conditions, the effectiveness profiles obtained from the IR measurements were similar in terms of profile shape, though the Ar jet was less effective than any other coolant jet. When comparing the effectiveness profiles obtained from PSP measurements, each gas showed jet bifurcation effects, though the bifurcation was most severe with the CO_2 coolant jet. Like the I = 0.25 case, this phenomenon was likely due to the elevated ReR of the CO_2 jet compared to the other coolant jets. The profiles as obtained from IR experimentation, however, show similar contours, though as was noted for the I = 0.25 cases, the Ar jet exhibited a lower adiabatic effectiveness magnitude at all points in the profile region due to its inability to absorb thermal energy without increasing in temperature, unlike the other cooling jets.

Table 4.10. Coolant Flow Rate Parameters at I = 0.5

	Thermal					PSP				
Coolant	M	$\boldsymbol{I}$	VR	ReR	ACR	M	$\boldsymbol{I}$	VR	ReR	ACR
Ar	0.85	**0.50**	0.58	0.73	0.44	0.86	**0.51**	0.59	0.73	0.45
CO_2	0.90	**0.50**	0.55	1.17	0.75	0.90	**0.50**	0.56	1.16	0.75
N_2	0.72	**0.51**	0.70	0.79	0.75	0.72	**0.50**	0.70	0.78	0.74
Air	0.73	**0.50**	0.69	0.77	0.73	--	--	--	--	--

Examination of the spanwise adiabatic effectiveness distributions shown in Fig. 4.15 revealed that in thermal experimentation each gas produces a similarly shaped and located profile, though the Ar jet produced a decreased effectiveness magnitude, while the CO_2, N_2, and air jets produced remarkably similar effectiveness magnitudes across the profile. At these flow conditions, the ACR values for the CO_2, N_2, and air jets were nearly matched at $ACR \approx 0.75$ while the Ar jet maintained an $ACR = 0.44$, which is approximately 59% that of the other jets, indicating that the Ar jet can absorb approximately 59% of the thermal energy per unit Kelvin as the other coolant jets, causing it to warm faster when exposed to the freestream flow. When comparing the PSP results, each gas produced a similar primary effectiveness peak as well as exhibited an inflection point further in the $-y/d$ direction. However, below the primary effectiveness peak, the effectiveness profiles diverged where the CO_2 effectiveness increased at the inflection point and the Ar and N_2 effectiveness distributions plateaued, though the N_2 jet was less effective below the primary peak than the Ar jet.

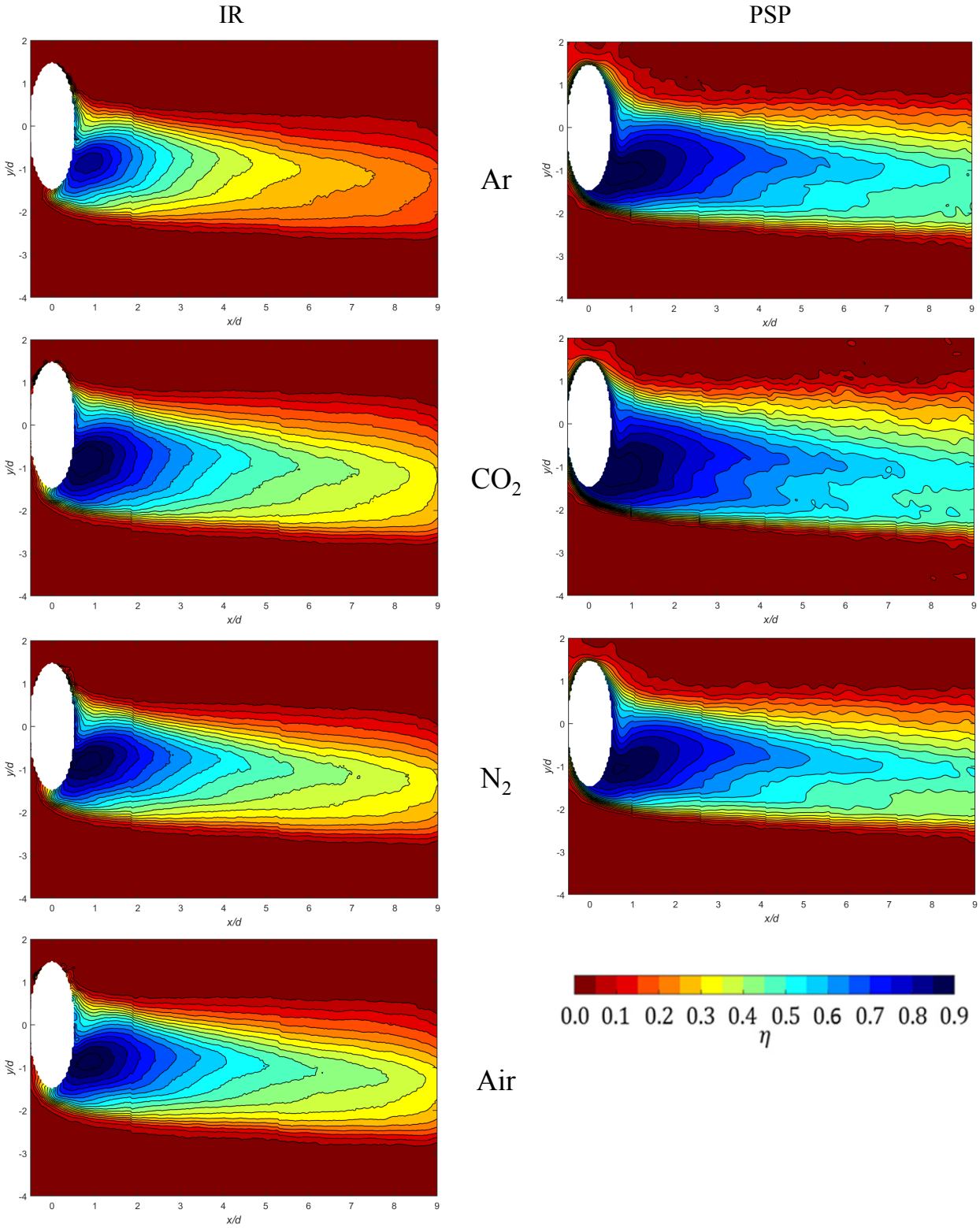

Figure 4.14. Adiabatic effectiveness contours at I = 0.5, IR (Left) and PSP (Right) methods

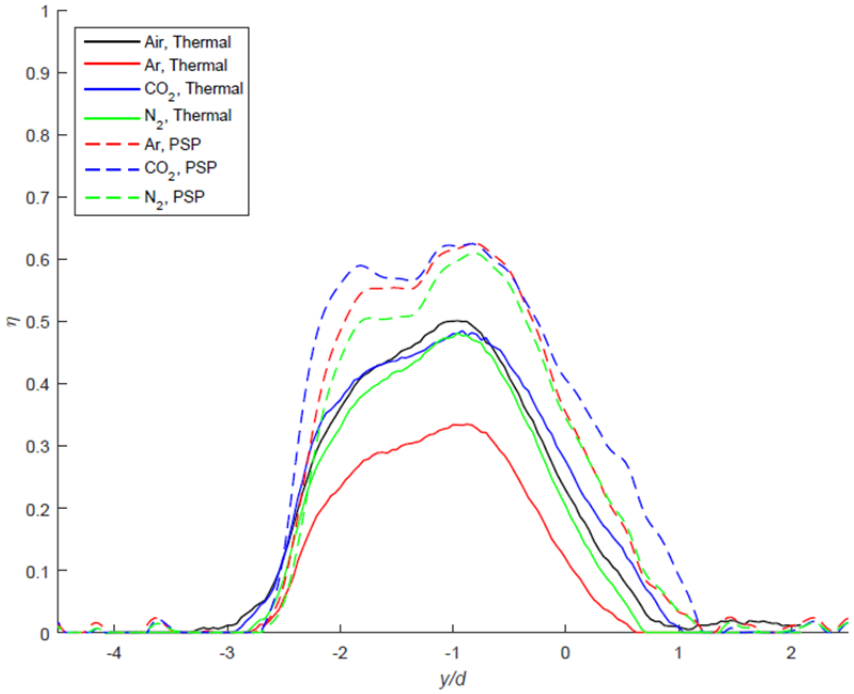

Figure 4.15. Spanwise adiabatic effectiveness profiles at x/d = 5.0, I = 0.5

Doubling the jet momentum to I = 1.0 resulted in the coolant flow rate parameter values tabulated in Table 4.11 and the contours shown in Fig. 4.16. As noted at I = 0.5, each gas produces a similar effectiveness profile at the matched I conditions—except for Ar, which maintained an ACR 60% that of the other jets. However, the PSP data suggests that the peak effectiveness location is near the bottom of the coolant jet trace while the IR data suggests that the peak effectiveness is near the center of the coolant trace—further indication that the thermal influence of the coolant jet is not necessarily collocated with the actual coolant jet. This phenomenon is shown in greater detail in Fig. 4.17 where the peak effectiveness location for the PSP cases was located further in the -y/d direction than the in the thermal cases, except for the Ar jet, which had similar peak locations between experimental techniques. Furthermore, the N_2 and Ar jets achieved their peak effectiveness at a greater y/d location than the CO_2 jet and also peak at a lower η value. When examined thermally, the CO_2, N_2, and air jets exhibited an

effectiveness peak near y/d = -1.5 relative to the peak at y/d = -1.9 for the Ar jet at x/d = 5.0. However, this difference may have been a result of thermal diffusion in the Ar jet as the larger thermal gradients would more readily diffuse through the lower c_P gas, smoothing out the spanwise profile. Despite the smoothing of the Ar jet—which is likely tied to the readiness that the Ar jet exchanges thermal energy with the freestream—matching the momentum flux ratio between gases appears to match the coolant jet placement and general shape of the coolant profile, regardless of the coolant density, while the ACR value at matched I conditions appears to scale the actual magnitude of the cooling effectiveness.

Table 4.11. Coolant Flow Rate Parameters at I = 1.0

	Thermal					PSP				
Coolant	M	$\boldsymbol{I}$	VR	ReR	ACR	M	$\boldsymbol{I}$	VR	ReR	ACR
Ar	1.22	**1.01**	0.83	1.05	0.63	1.21	**1.00**	0.83	1.03	0.63
CO_2	1.27	**0.99**	0.78	1.67	1.06	1.27	**0.99**	0.78	1.64	1.06
N_2	1.02	**1.00**	0.99	1.11	1.05	1.02	**1.00**	0.99	1.10	1.05
Air	1.04	**1.01**	0.97	1.09	1.04	--	--	--	--	--

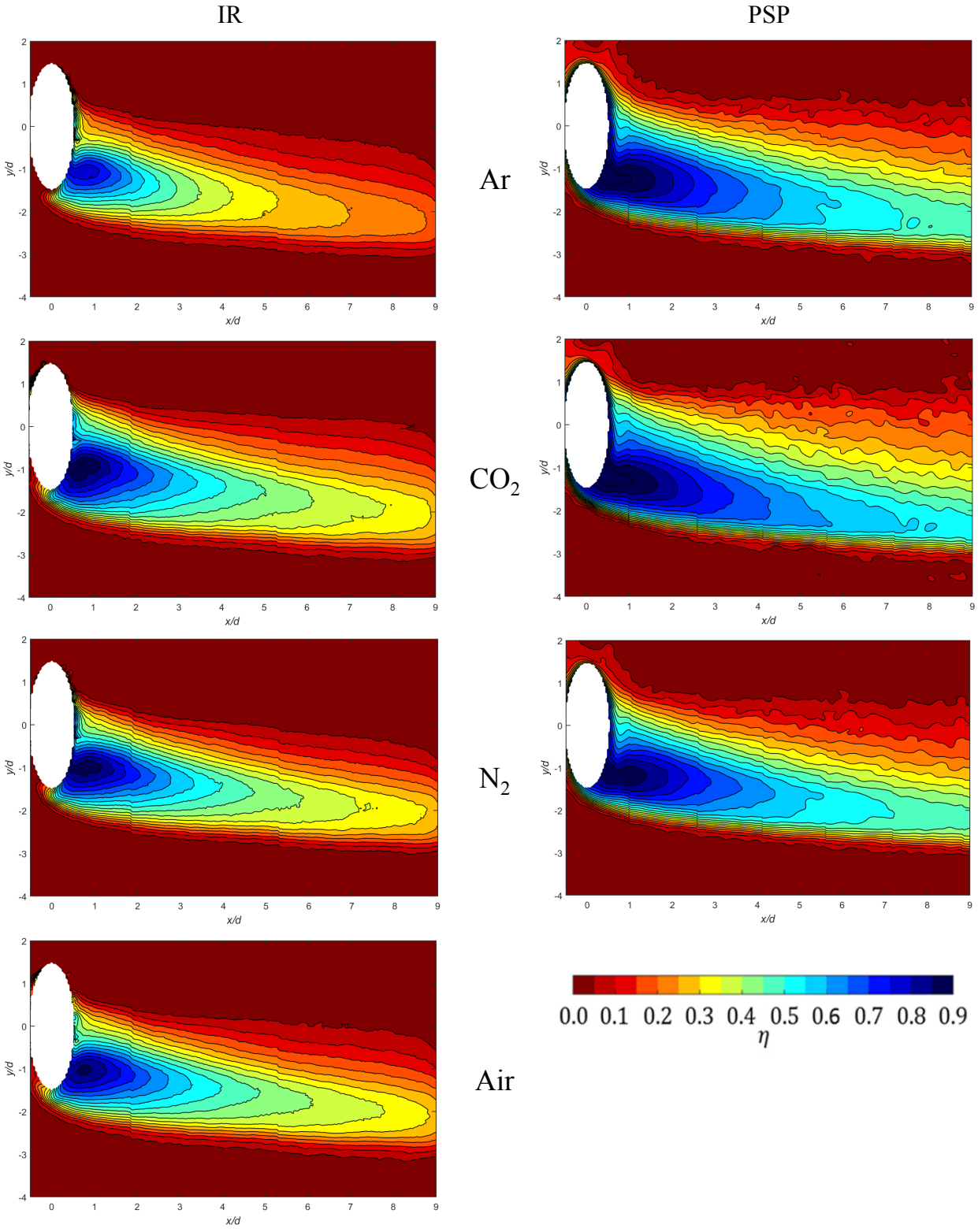

Figure 4.16. Adiabatic effectiveness contours at I = 1.0, IR (Left) and PSP (Right) methods

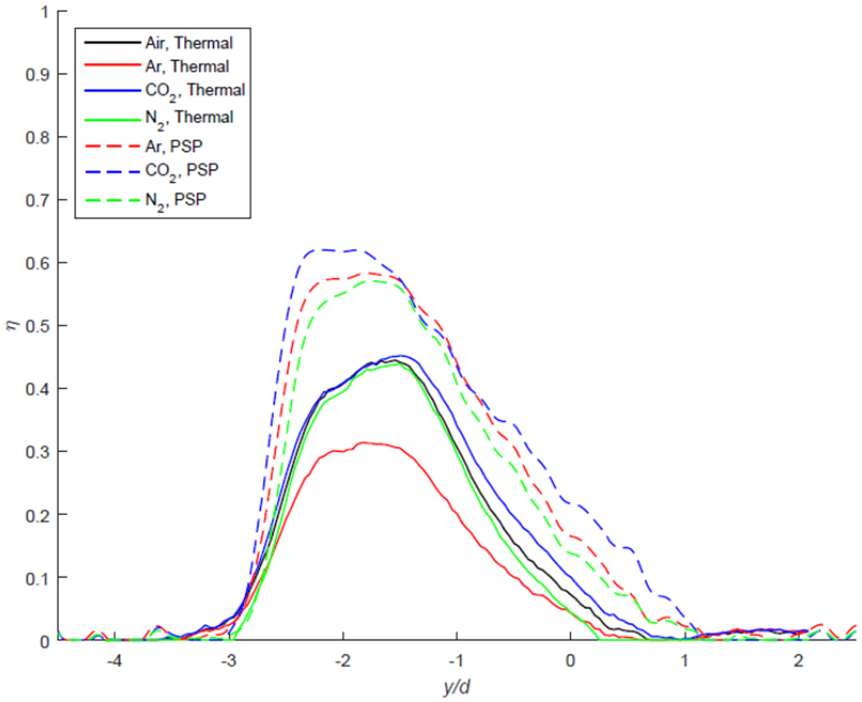

Figure 4.17. Spanwise adiabatic effectiveness profiles at x/d = 5.0, I = 1.0

In an effort to further characterize the influence of I on the η distribution, and to determine if the observed scaling qualities of I would apply to a high momentum jet, the momentum flux ratio was again doubled to I = 2.0. At these I conditions, the coolant flow rate parameters tabulated in Table 4.12 and the contours shown in Fig. 4.18 were observed. At these flow conditions, similar profile shapes were obtained regardless of coolant selection, though each PSP case exhibited the gradual lateral decrease in adiabatic effectiveness directly behind the cooling hole that is not visible using the thermal method. In addition, the jet effectiveness regions penetrated further in the -y/d direction when observed with PSP than with IR, likely due again to thermal diffusion near the bottom edge of the coolant jet impeding the penetration of the elevated effectiveness region. This phenomenon becomes more obvious during examination of the spanwise η profiles shown in Fig. 4.19 where the peak adiabatic effectiveness as observed with PSP was located approximately 0.2 hole diameters further in the -y/d direction than the IR

observed effectiveness regardless of the cooling gas used and the downstream location. Furthermore, the PSP cases exhibited an adiabatic effectiveness magnitude of approximately 0.1 at the same point where the thermal effects of the coolant jet had diffused away, indicating that while coolant was present at those locations, the coolant had likely equilibrated thermally with the freestream and no longer exhibited a cooling effect.

Table 4.12. Coolant Flow Rate Parameters at I = 2.0

	Thermal					PSP				
Coolant	M	$\boldsymbol{I}$	VR	ReR	ACR	M	$\boldsymbol{I}$	VR	ReR	ACR
Ar	1.72	**2.01**	1.17	1.48	0.89	1.71	**2.00**	1.17	1.45	0.88
CO_2	1.80	**2.00**	1.11	2.34	1.51	1.80	**2.01**	1.12	2.34	1.51
N_2	1.44	**2.00**	1.39	1.57	1.48	1.44	**2.01**	1.40	1.56	1.49
Air	1.47	**2.00**	1.36	1.56	1.47	--	--	--	--	--

In addition, the thermal experiments showed a similar sensitivity to the coolant jet ACR that was observed with the lower momentum jets with Ar exhibiting the lowest ACR value and lowest effectiveness magnitude. Furthermore, at these high momentum flux conditions, the jet Reynolds number does not appear to influence the effectiveness profile as severely as at the I = 0.25 condition, as the CO_2 jet produced a similar profile shape as the other cooling jets despite the approximately 50% greater jet Reynolds number. Finally, the trend of CO_2 exhibiting the greatest cooling effectiveness when evaluated using PSP persisted at these high momentum flux conditions.

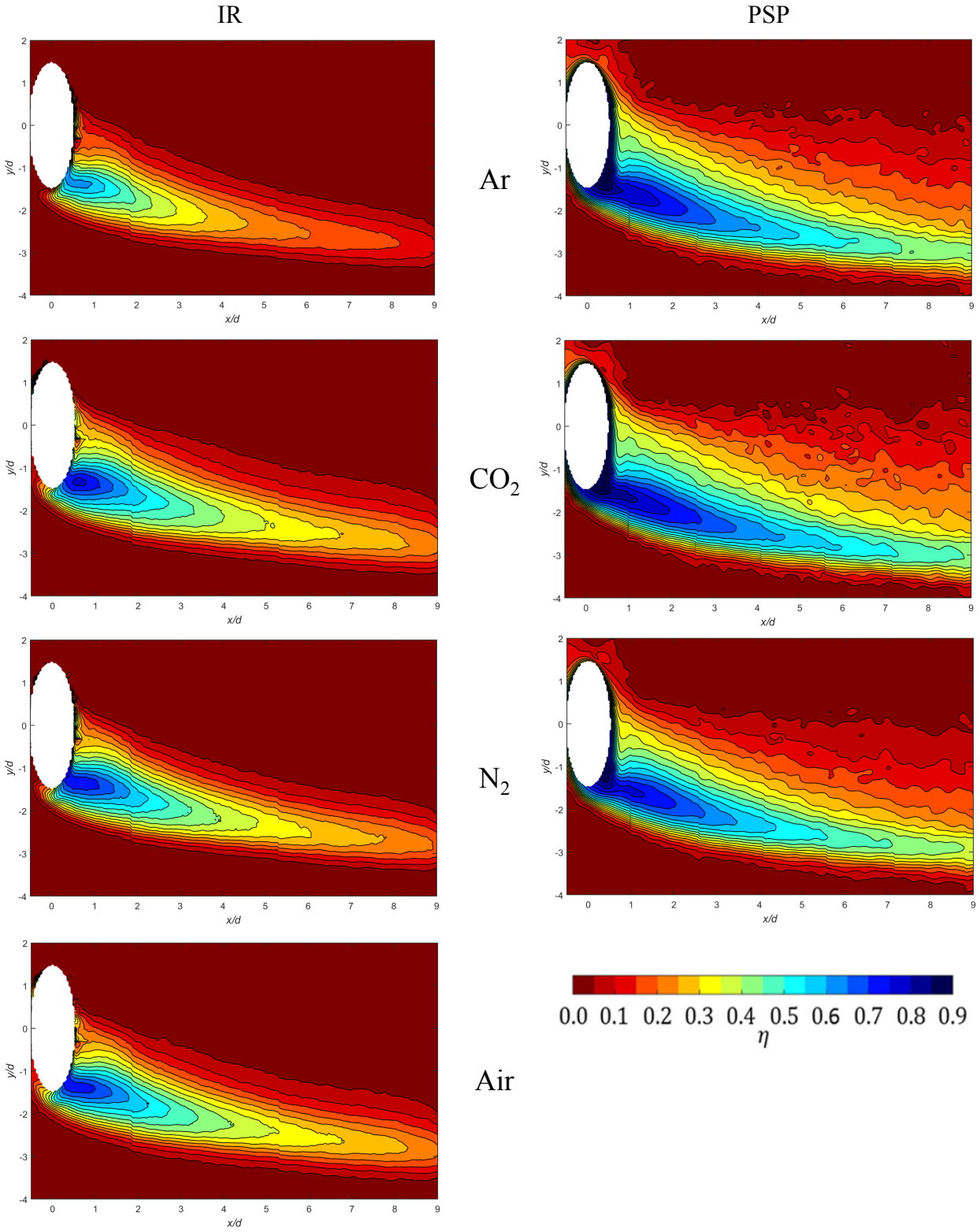

Figure 4.18. Adiabatic effectiveness contours at I = 2.0, IR (Left) and PSP (Right) methods

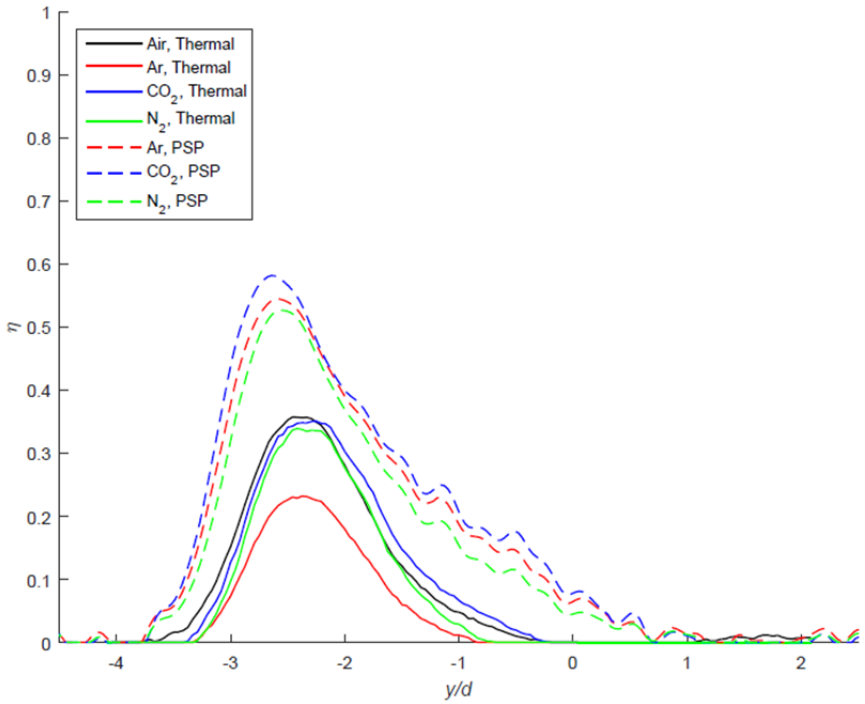

Figure 4.19. Spanwise adiabatic effectiveness profiles at x/d = 5.0, I = 2.0

4.1.5 Reynolds Number Ratio

Based on the hypothesized relationship between the coolant-to-freestream Reynolds number ratios (ReR) and key coolant jet effectiveness structures, matched ReR conditions were evaluated. Like M, ReR accounts for the mass flux of the coolant jet relative to the freestream, but also takes the dynamic viscosity ratio between the coolant and freestream into account. Fully developed adiabatic effectiveness contours were achieved at ReR = 0.5 for each gas except for CO_2 which still exhibited the finger patterns indicative of an underdeveloped cooling jet. The coolant flow rate parameter values at the ReR = 0.5 conditions are shown in Table 4.13, and like the matched M cases, the η contours—shown in Fig. 4.20—separate into two groups, where Ar, N_2, and air cases exhibit fully developed coolant jets with similar profile shapes at $I \approx 0.23$, and the CO_2 jet exhibits an underdeveloped coolant jet at I = 0.09. The similar I values between Ar, N_2, and air that resulted at these conditions were the result of the inclusion of the dynamic

viscosity in the coolant flow rate parameter. Though Ar has an elevated DR at these conditions, the dynamic viscosity ratio is also elevated (See Table 4.1) requiring a greater VR to achieve $ReR = 0.5$, increasing the jet momentum flux. On the other hand, CO_2 requires a relatively low VR compared to Ar, N_2, and air since the DR is elevated compared to all other gases and dynamic viscosity ratio for CO_2 is less than each other gas, resulting in a lower required flow rate—and momentum flux—to achieve $ReR = 0.5$. Detailed comparisons of the spanwise profiles are shown at x/d = 5.0 in Fig. 4.21. At this x/d location, the CO_2 jet exhibited a significantly different profile than the other gases with multiple effectiveness peaks. As a result of the severe difference between the CO_2 jet and the other gases at ReR = 0.5 conditions, the coolant ReR can be eliminated as an effective scaling parameter in terms of scaling density ratio, particularly when compared to the momentum flux ratio. However, ReR may be useful for predicting other flow structures, such as the observed coolant flow bifurcation patterns, though that analysis is beyond the scope of this research; particularly since matched I conditions offer only two different ReR values across the evaluated coolant gases and ReR appears to have a more subtle impact on the η distribution than ACR.

Table 4.13. Coolant Flow Rate Parameters at ReR = 0.5

	Thermal					PSP				
Coolant	*M*	*I*	*VR*	***ReR***	*ACR*	*M*	*I*	*VR*	***ReR***	*ACR*
Ar	0.58	0.23	0.40	**0.50**	0.30	0.59	0.24	0.41	**0.50**	0.31
CO_2	0.39	0.09	0.24	**0.50**	0.32	0.38	0.09	0.24	**0.50**	0.32
N_2	0.46	0.21	0.45	**0.50**	0.47	0.46	0.21	0.45	**0.50**	0.48
Air	0.47	0.21	0.44	**0.50**	0.47	--	--	--	--	--

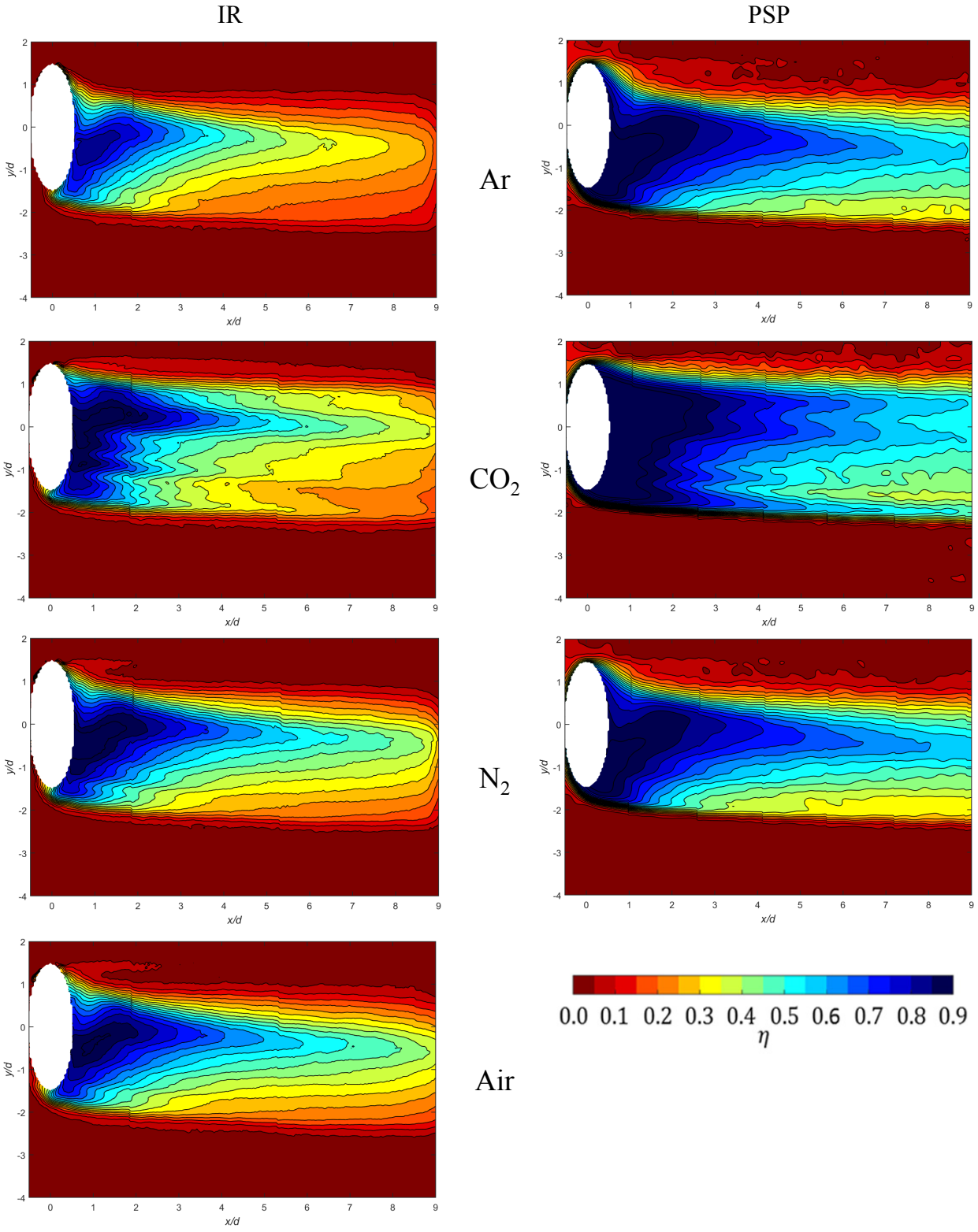

Figure 4.20. Adiabatic effectiveness contours at *ReR* = 0.5, IR (Left) and PSP (Right) methods

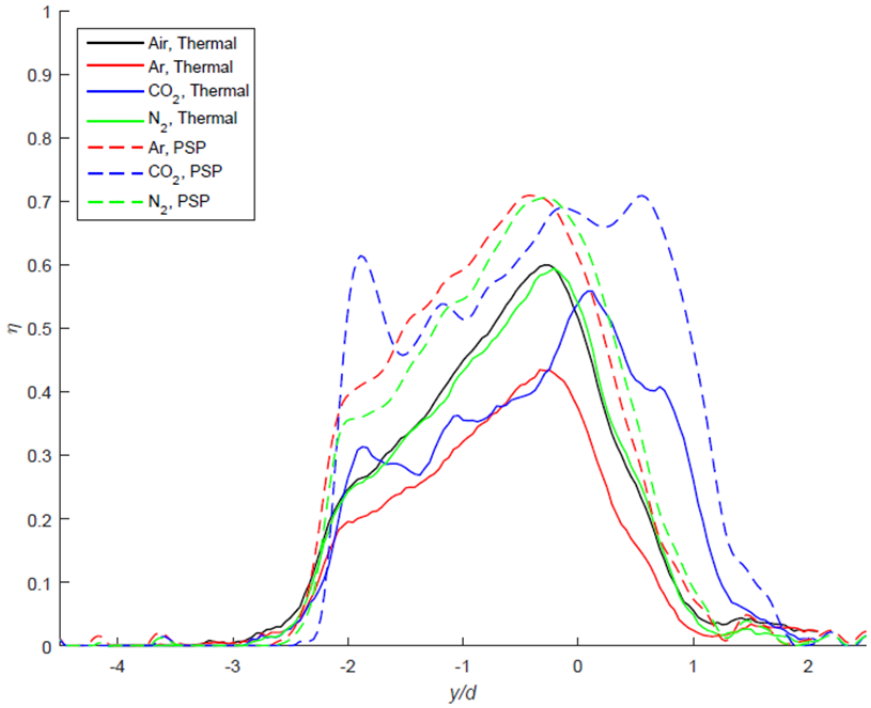

Figure 4.21. Spanwise adiabatic effectiveness profiles at x/d = 5.0, ReR = 0.5

4.1.6 Advective Capacity Ratio

Based on the results obtained at matched I conditions, matched ACR conditions were evaluated in order to determine whether ACR would be capable of properly predicting jet effectiveness magnitude. For simplicity, the first ACR condition evaluated was ACR = 1.0, and inspection of Table 4.14 reveals that at these conditions, the momentum flux ratio was near-matched at $I \approx 0.9$ for CO_2, N_2, and air, while the Ar cooling jet maintained a momentum flux ratio approximately 280% that of other gases since a large VR was required to offset the low c_P of the Ar coolant. As a result, the Ar jet was expected to exhibit a thin region of elevated effectiveness that was displaced further in the -y/d direction than the other coolant jets. Figure 4.22 shows the adiabatic effectiveness contours at ACR = 1.0 conditions. At these conditions, the CO_2, N_2, and air jets exhibit similar effectiveness contours, both in shape and magnitude, while the Ar jet is thin and displaced further in the -y/d direction. Figure 4.23 shows the spanwise

adiabatic effectiveness distributions for each gas at these conditions at x/d = 5.0. The CO_2, N_2, and air cases produced fairly similar spanwise effectiveness distributions when using the thermal method, but the CO_2 jet produced a region of elevated effectiveness with greater peak effectiveness than the N_2 jet when evaluated with PSP.

Table 4.14. Coolant Flow Rate Parameters at ACR = 1.0

	Thermal					PSP				
Coolant	M	I	VR	ReR	$\boldsymbol{ACR}$	M	I	VR	ReR	$\boldsymbol{ACR}$
Ar	1.93	2.53	1.31	1.66	**1.00**	1.93	2.54	1.32	1.65	**1.00**
CO_2	1.19	0.88	0.74	1.56	**1.00**	1.19	0.88	0.74	1.54	**1.00**
N_2	0.97	0.91	0.94	1.06	**1.00**	0.97	0.91	0.94	1.05	**1.00**
Air	1.00	0.93	0.93	1.06	**1.00**	--	--	--	--	--

In order to determine whether the trends observed at ACR = 1.0 applied at elevated flow rates, ACR = 2.0 conditions were evaluated, resulting in the flow rate parameters shown in Table 4.15. Most notably, to reach the ACR = 2.0 condition, the Ar jet required a flow rate corresponding to $I \approx 10.1$, resulting in the highly displaced and separated jet shown in Fig. 4.24. In addition to the highly separated Ar jet, the effectiveness contours produced by the CO_2 jets exhibited lines of constant η that extended to greater x/d locations than their air and N_2 counterparts. This phenomenon is more readily visualized in the spanwise effectiveness distributions shown in Fig. 4.25 where the CO_2 jet exhibited a peak effectivness approximately 0.05 greater than the air case at x/d = 5.0. It is unlikely that this deviation was due to an increased level of jet separation by the air jet since the air jet's momentum flux was only 5% greater than that of the CO_2 jet.

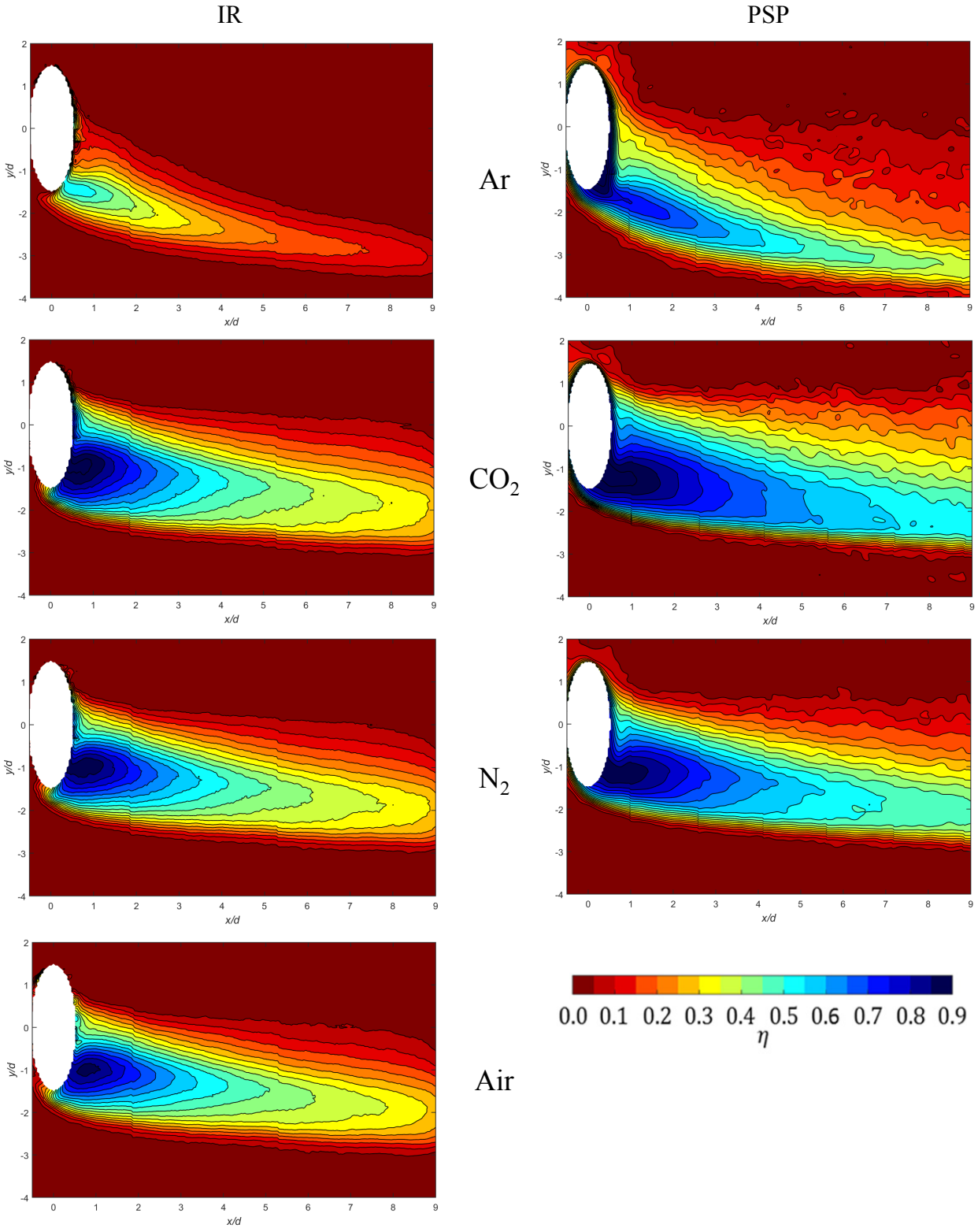

Figure 4.22. Adiabatic effectiveness contours at ACR = 1.0, IR (Left) and PSP (Right) methods

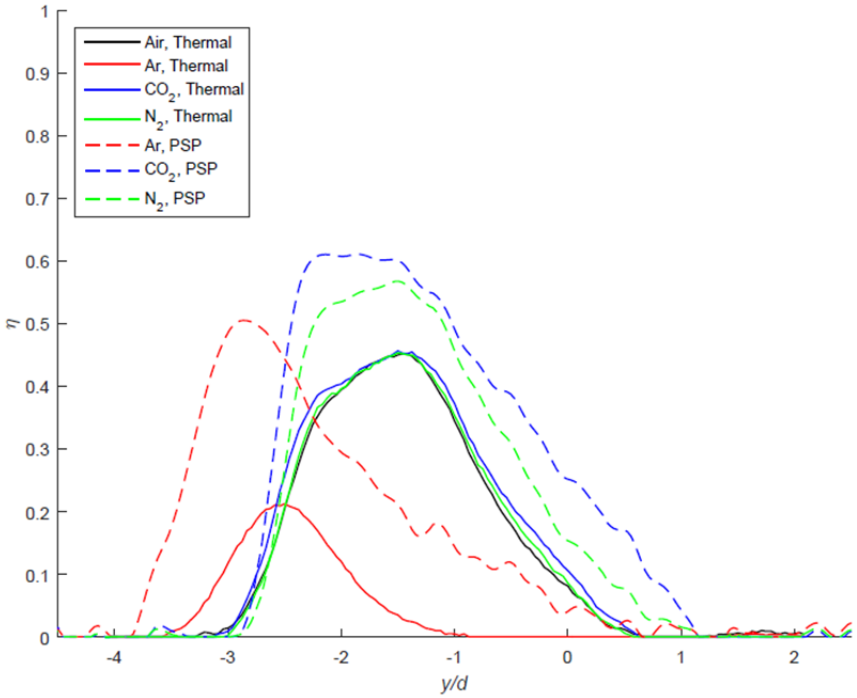

Figure 4.23. Spanwise adiabatic effectiveness profiles at x/d = 5.0, ACR = 1.0

Table 4.15. Coolant Flow Rate Parameters at ACR = 2.0

	Thermal					PSP				
Coolant	M	I	VR	ReR	$\boldsymbol{ACR}$	M	I	VR	ReR	$\boldsymbol{ACR}$
Ar	3.87	10.14	2.62	3.33	**2.00**	3.86	10.11	2.62	3.32	**2.00**
CO_2	2.39	3.50	1.46	3.14	**2.00**	2.39	3.53	1.48	3.11	**2.00**
N_2	1.94	3.62	1.87	2.13	**2.01**	1.94	3.63	1.87	2.11	**2.00**
Air	2.00	3.68	1.84	2.14	**2.00**	--	--	--	--	--

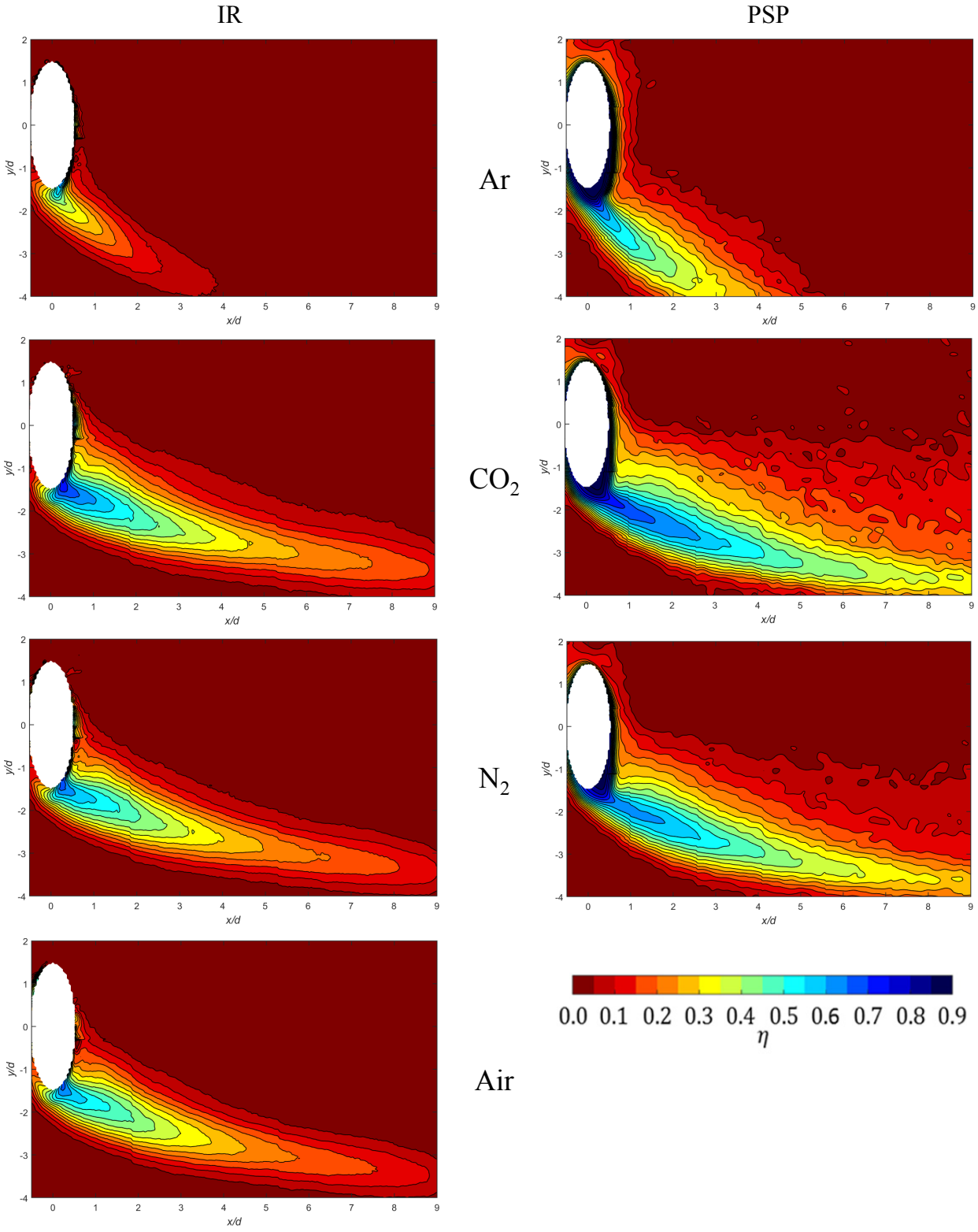

Figure 4.24. Adiabatic effectiveness contours at ACR = 2.0, IR (Left) and PSP (Right) methods

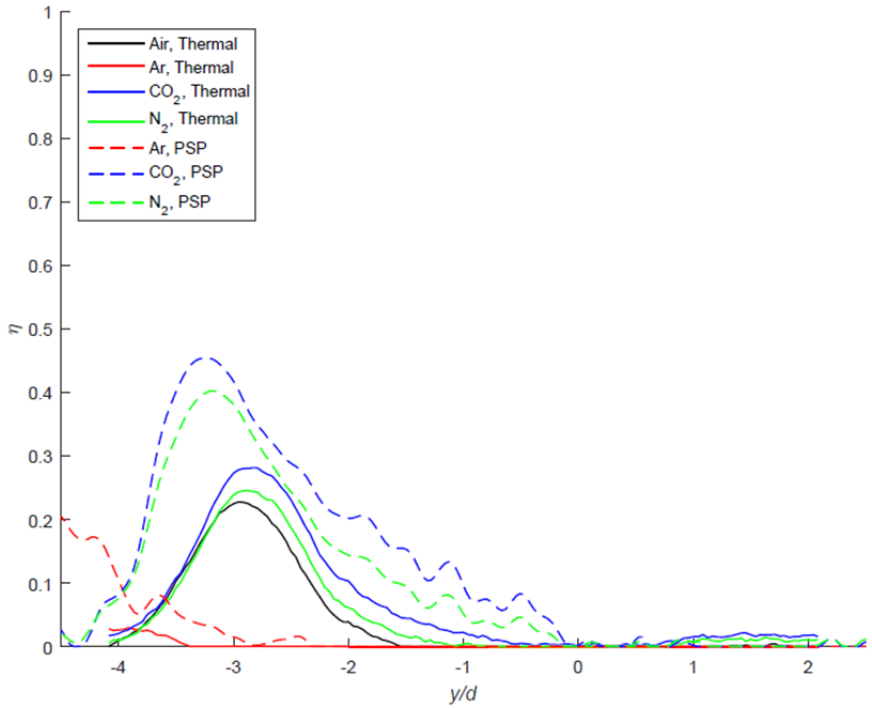

Figure 4.25. Spanwise adiabatic effectiveness profiles at x/d = 5.0, ACR = 2.0

The more likely cause of this deviation was that at these elevated flow rate conditions, the influence of gas mixing becomes more significant than at lower flow rates. The effects of coolant gas mixing with the freestream flow were discussed in terms of the specific heat in Section 2.4, based on the work of Jones [23]. As the coolant jet mixes with the freestream, the local fluid specific heat is both a function of the local fluid temperature as well as the local fluid composition. Furthermore, this process can be similarly applied for any fluid transport property. As a result, coolant-to-freestream property ratios are not constant throughout the span of the coolant jet. However, the physical phenomena that result in the possible increased influence of coolant and freestream mixing at these flow conditions are not readily apparent. Comparison of various matched ACR conditions, however, highlights the influence of these phenomena. Table 4.16 shows the coolant flow rate parameters that resulted from evaluating CO_2 and Air coolant jets at various matched ACR conditions. The results obtained from thermal experiments at these

conditions are shown in Fig. 4.26 at x/d = 5.0 for each tabulated ACR condition. At ACR = 1.0 and 1.5, the two gases produce similar profiles, while at other conditions, the CO_2 and air jets produced different effectiveness profiles. The ACR = 0.5 cases produced profiles to those shown in Fig. 4.13, corresponding to I = 0.25. At these conditions, the elevated coolant Reynolds number of the CO_2 jet was hypothesized to be the source of this discrepancy between the effectiveness profiles. As the flow rates increased to $ACR \geq 1.75$, however, the CO_2 and air jets produced similar effectiveness profile shapes, but the CO_2 jet produced greater effectiveness at each point in the profile, possibly due to the elevated CO_2 jet Reynolds number, which may inhibit jet mixing with the freestream, maintaining elevated effectiveness. This deviation between the CO_2 and air jets was not observed at the elevated I conditions discussed Section 4.1.4. However, this may have been a result of the relatively low maximum matched I conditions of I = 2.0 achieved over the course of matched I experimentation while matched ACR = 1.75 conditions resulted in I = 2.69 and 2.83 for the CO_2 and air jets, respectively, indicating that at matched I conditions greater than 2, matched ACR flows do not necessarily produce the same effectiveness magnitude.

Table 4.16. Coolant Flow Rate Parameters at Various Matched ACR Conditions

CO_2					Air				
M	I	VR	ReR	$\boldsymbol{ACR}$	M	I	VR	ReR	$\boldsymbol{ACR}$
0.60	0.22	0.37	0.79	**0.50**	0.50	0.24	0.47	0.53	**0.50**
1.19	0.88	0.74	1.56	**1.00**	1.00	0.93	0.93	1.06	**1.00**
1.80	1.99	1.11	2.34	**1.50**	1.51	2.10	1.39	1.60	**1.50**
2.10	2.69	1.28	2.75	**1.75**	1.75	2.83	1.62	1.86	**1.75**
2.39	3.50	1.46	3.14	**2.00**	2.00	3.68	1.84	2.14	**2.00**

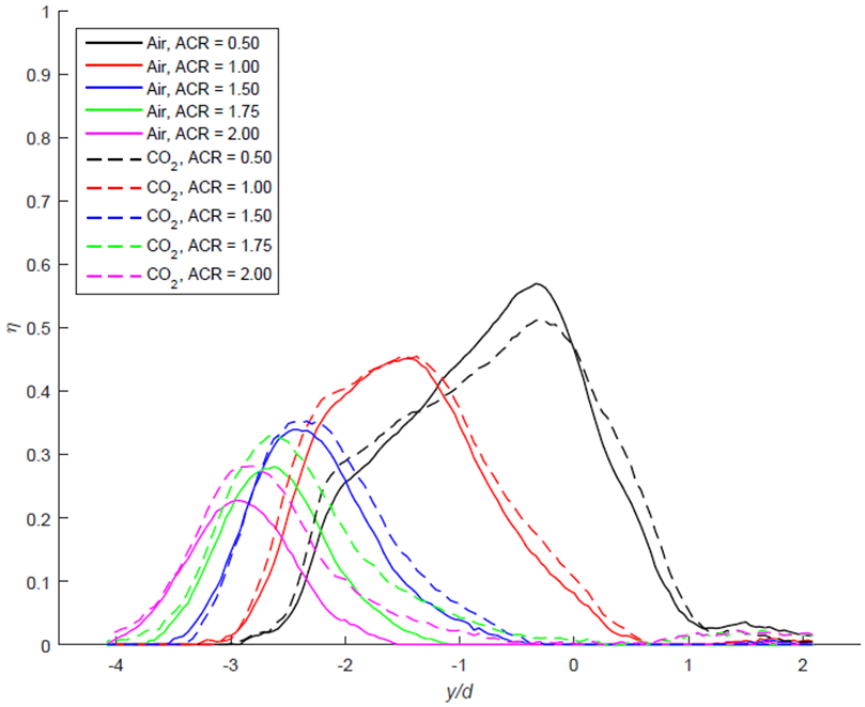

Figure 4.26. Spanwise adiabatic effectiveness profiles at x/d = 5.0 for CO_2 and air at various ACR conditions

The objective of matching the ACR values between the cooling gases was to determine whether the advective capacity ratio was able to scale effectiveness magnitudes between conditions. However, since the Ar jet was displaced from the other jets to the point of coolant jet separation, comparison of the Ar jet to the others was not possible. At matched $ACR \geq 1.75$, despite relatively matched I conditions, the CO_2 jets exhibited greater effectiveness than the air and N_2 jets. In order to fully characterize the merits of ACR on scaling adiabatic effectiveness magnitude, matched ACR experiments should be conducted at flow conditions that are not momentum dominated, such as on a flat plate with zero compound angle injection. The elimination of ACR as an ideal coolant flow rate parameter does not, however, diminish its importance as a flow rate parameter since ACR values achieved at matched I conditions up to I = 2.0 were shown to consistently scale jet effectiveness in IR experimentation.

4.2 Comparison of PSP and IR Methodologies

The second objective of this work was to determine whether the PSP technique is a valid substitution for thermal techniques. Since both PSP and IR methodologies were implemented and evaluated with matched geometries, coolant flow rate parameters, and experimental conditions, direct comparisons between the IR and PSP methods were made. Previous sections touched on some of the differences between adiabatic effectiveness distributions as observed with PSP and IR measurements, though a detailed discussion of hypotheses for why these phenomena were observed were not discussed. The most obvious difference between adiabatic effectiveness measurements obtained with the IR and PSP techniques was that the adiabatic effectiveness magnitude as observed using the PSP technique was greater than that of the companion IR measurement. This phenomenon is shown in Fig. 4.27 at I = 1.0 using N_2 as the coolant gas. Perhaps the most obvious difference between the effectiveness contours is that the η = 0.45 contour extends beyond x/d = 9.0 according to the PSP measurement, though the IR measurement indicates that this same contour does not extend beyond x/d = 5.0. Other significant flow features include the presence of a wide region where η > 0.05 at x/d = 9.0 that was observed with the PSP method, extending over the range -3.0 ≤ y/d ≤ 0.5 while the η > 0.05 region was confined to the range -3.0 ≤ y/d ≤ -0.9 using the IR technique at this position. Figure 4.28 shows the decay of the maximum adiabatic effectiveness, η_{max}, with respect to streamwise position, x/d, for both the thermal and PSP techniques at the previously discussed conditions, with each coolant gas. With each gas, the PSP technique exhibited greater peak effectiveness across the entire range 1.0 ≤ x/d ≤ 9.0.

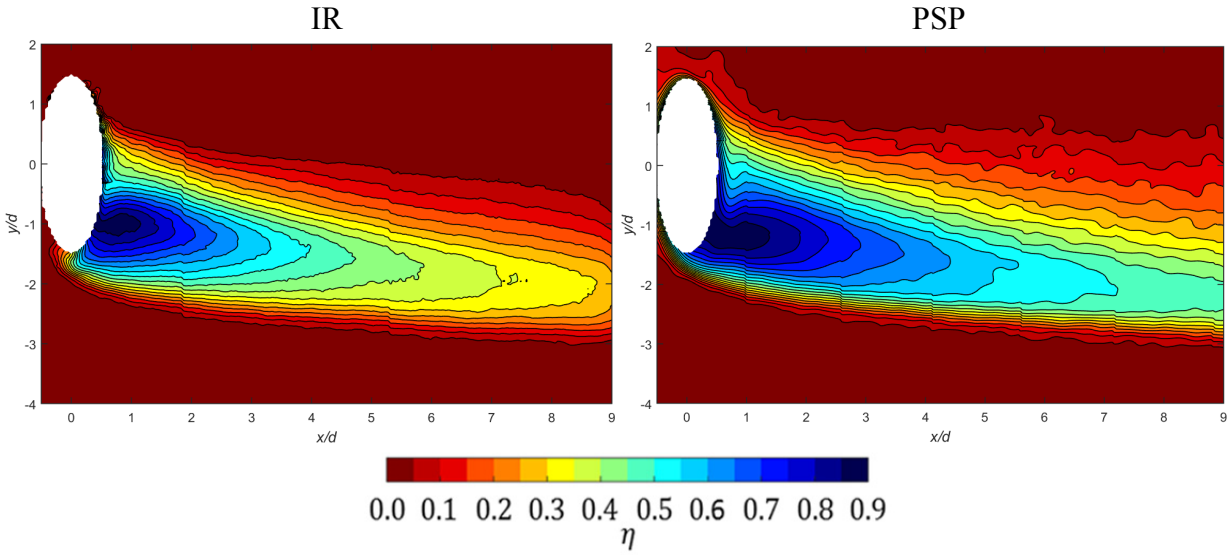

Figure 4.27. Adiabatic effectiveness contours at I = 1.0 for N_2 using IR (left) and PSP (right) techniques

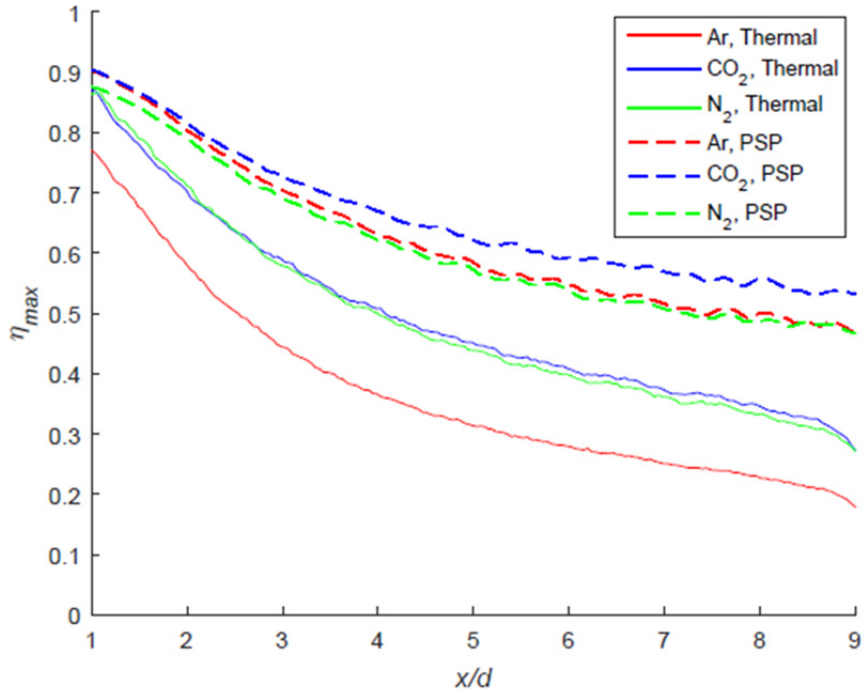

Figure 4.28. Downstream η_{max} decay for Ar, CO_2, and N_2 at I = 1.0, PSP and IR methods

This observed difference in coolant effectiveness between experimental techniques was likely due to the influence of an additional diffusional process that affects the adiabatic effectiveness as observed with thermal measurements, since the coolant jets each experience

mass, momentum, and thermal diffusion, though PSP adiabatic effectiveness is not sensitive to the latter process. In terms of particle kinetics, thermal energy can be transported by two primary mechanisms: diffusional transport of mass—where a particle carries its kinetic energy (expressed as temperature) from one location to another, and particle collisions—wherein thermal energy is transported from one particle to another through the conservation of momentum. As a result, the influence of warm (higher energy) freestream particles can be detected at the surface either by transmission of their thermal energy through the coolant plume through a series of collisions, or by penetrating the coolant plume to the surface; though since the fluid flows examined in this work were not rarefied, the likelihood of a particle from the freestream reaching the surface without encountering another particle is highly unlikely. This is not to say that freestream particles do not reach the model surface since the PSP technique relies on the penetration of freestream O_2 molecules through the anaerobic coolant plume to the surface in order to influence the radiative emission of the PSP coating. As a result, the binary PSP is not sensitive to the transfer of thermal energy that precedes the O_2 molecule as it approaches the model surface, rather only its impingement upon it, while the surface temperature measurements are influenced by the transfer of thermal energy from the freestream particles. Furthermore, the freestream O_2 molecules could be further delayed in reaching the surface if they were to enter and subsequently eject from the coolant plume without ever reaching the surface, while their thermal influence may still penetrate the coolant plume.

Further analysis of Fig. 4.28, in conjunction with Tables 4.1 and 4.11, reveals that the behavior and downstream decay of the peak effectiveness as observed using the PSP method may be influenced by the coolant jet binary diffusion coefficient as Ar and N_2 produced similar peak effectiveness and maintained binary diffusion coefficient ratios with the freestream of 0.90

and 0.94, respectively, while the more effective CO_2 jet maintained a binary diffusion coefficient ratio of 0.76. This decreased $\mathcal{D}_{AB,c}/\mathcal{D}_{AB,\infty}$ value could cause the CO_2 coolant jet to resist the penetration of O_2 molecules from the freestream, while the Ar and N_2 jets allow this process more readily. This effect was not seen readily observed when using the thermal method, where the less molecularly diffusive CO_2 jet performed similarly to the N_2 jet. Furthermore, as mentioned in Section 4.1.4, at these matched I conditions, the N_2 and CO_2 jets maintain similar ACR and produce similar peak effectiveness when evaluated with the thermal method, while the Ar jet, with a reduced ACR, exhibited reduced peak effectiveness, an effect that is not apparent with the PSP technique, where Ar performed comparably to N_2.

In addition to the observed elevated adiabatic effectiveness, the PSP technique also revealed additional flow structures that were not readily apparent using the IR technique. In particular, PSP evaluations revealed the presence of coolant jet bifurcation; evident at I = 0.5 with CO_2 coolant and shown again in Fig. 4.29. The bifurcated coolant jet manifests itself as a pair of effectiveness peaks located at $y/d \approx$ -1 and $y/d \approx$ -2 when evaluated using PSP. The effectiveness distribution obtained from the thermal method, however, only shows the effectiveness peak located at $y/d \approx$ -1, indicating that the lower peak observed with PSP is a relatively warm column of CO_2 that separated from the main CO_2 jet after exiting the coolant hole.

In an effort to avoid the uncertainties due to conduction that are present in thermal experimentation, the PSP technique suffers from measuring fundamentally different quantities in the coolant jet, namely evaluating the fluid composition on the model surface while thermal techniques evaluate the temperature of the model surface. Furthermore, by evaluating the fluid composition rather than the temperature on the surface, and because there is lateral conduction

through the coolant jet that is observable using IR methods, the thermal effect of the jet does not necessarily collocate with the regions of high coolant concentration. As a result, PSP cannot be treated as a perfect substitution for thermal adiabatic effectiveness measurements. However, PSP does have certain properties of merit, particularly in evaluating the influence of cooling geometries on the coolant distribution, especially when using engine hardware since complex geometries may prohibit the use of low thermal conductivity materials and the influences of multi-dimensional conduction may dominate the thermal interactions with the freestream. In addition, PSP techniques could be applied to investigate coolant flow effects, such as jet bifurcation and jet development since PSP yields a better appreciation for how the coolant is distributed on the model surface. Thermal methods, however, provide a better indication of the actual cooling influence distribution of a particular coolant jet.

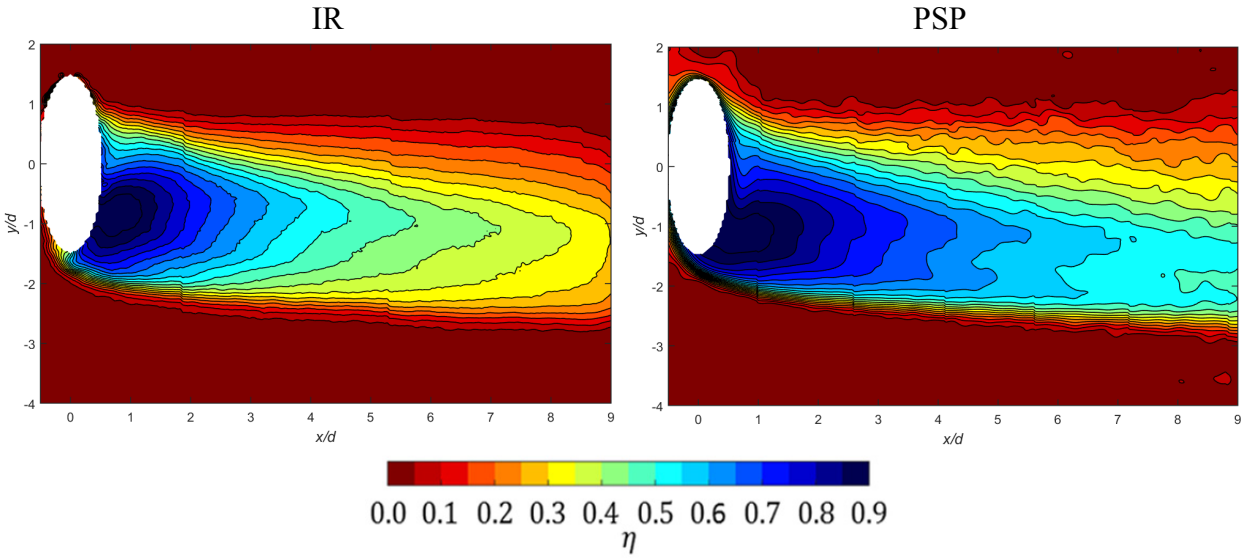

Figure 4.29. Adiabatic effectiveness contours at I = 0.5 for CO_2 using IR (left) and PSP (right) techniques

5. Conclusions and Recommendations

5.1 Conclusions of Research

The first objective of this research was to determine the influence of various flow rate parameters on the adiabatic effectiveness distributions on a film cooled leading edge. Characterization of coolant flow rate parameter effects provided information for the design of future experiments for this test geometry, as well as indicated the necessary conditions for meaningful comparisons between coolant gases. The second objective was to compare the adiabatic effectiveness results obtained from thermal and PSP experimentation to determine if the resultant effectiveness distributions were interchangeable for use in gas turbine heat transfer evaluations.

5.1.1 Coolant Flow Rate Parameter Effects

The influence of the coolant flow rate parameters was found to be primarily two-fold. First, the shape and location of the elevated effectiveness regions were found to be best predicted by the momentum flux ratio, I, likely because the compound angle injection examined in this study resulted in a momentum dominated flow field. The ability of I to match the shape and location of the elevated effectiveness regions was shown to be true regardless of the measurement technique, though the profile shapes as observed with PSP differed from those collected using the IR technique.

The second component of the scaling process, however, was linked to the advective capacity ratio, ACR, which was examined experimentally for the first time in this study. ACR was found to scale the magnitude of the cooling effectiveness, though scaling between the coolant gases was only able to be accomplished at matched I conditions since at matched ACR conditions, the coolant gases were not necessarily collocated. ACR was implemented to quantify

the ability of the coolant to absorb thermal energy from the freestream, rather than transferring it to the surface. As a result, low heat capacity coolants, such as argon, were found to produce decreased ACR and, subsequently, η values compared to the other coolants at matched I conditions when evaluated with the IR method. This phenomenon was not observed, however, when using PSP, since the thermal transport properties do not influence the mass diffusion process. This was particularly evident when comparing the PSP and IR results between Ar and N_2 jets which produced similar PSP results at matched I conditions, but the N_2 jet was more effective than the Ar jet when evaluated with the IR technique.

Though I and ACR were found to be the major contributors to the scaling process, the coolant-to-freestream Reynolds number ratio (ReR) was thought to influence the development of various coolant jet features, such as jet bifurcation and jet development, however, the influence of ReR may be more subtle than the uncertainty in the current methods allows for proper investigation.

5.1.2 Measurement Technique Comparison

The PSP technique resulted in a higher adiabatic effectiveness, regardless of cooling gas, than the thermal technique. This effect was attributed to the fundamental differences in the measurands for the two techniques. The thermal method relies on the temperature at the model surface while the PSP method measures the local composition of the fluid at the surface. The actual temperature at the surface, however, is influenced by three diffusional processes since the thermal effects of the freestream can penetrate the coolant plume without the coolant plume mixing with the freestream. As a result, the temperature of the surface approaches the freestream temperature at a greater rate than the surface fluid composition approaches the freestream composition. Furthermore, in high momentum flux flows, the maximum adiabatic effectiveness

as observed with PSP was displaced further in the $-y/d$ direction than when using the thermal technique, indicating that the PSP was not accurately describing the thermal influence of the coolant jet, but rather was describing the physical location and distribution of the coolant. As a result, PSP was found to show coolant distribution features that were not obvious when evaluated using thermal methods. For instance, jet bifurcation was more readily apparent when using the PSP method since the coolant distribution was not hidden by the thermal diffusion process. This finding results in another feature of mass transfer methods that is appealing in some situations—that the thermal transport properties of the freestream and coolants become decoupled from the system, allowing for evaluation of the flow physics in terms of inertial and mass transfer properties alone, which is useful for determining how the coolant is distributed on the model surface.

5.2 Significance of Research

The significance of this work is multi-faceted. First, in the leading edge region, the momentum flux ratio was found to best scale the effects of coolant-to-freestream density ratio in terms of the location and shape of the region of elevated adiabatic effectiveness, while ACR scales the effectiveness magnitude in thermal experiments, better informing future gas turbine film cooling experimentation. Furthermore, while choosing to use a mass transfer method rather than a thermal method may remove the uncertainty due to conduction into the model surface, information that may be critical to cooling flow evaluation may be lost, such as the location and intensity of the coolant jet's thermal influence. However, mass transfer methods do allow for the observation of flow effects that are subdued by thermal diffusion. Therefore, caution must be used in the application of results obtained from mass transfer experimentation to quantify actual gas turbine adiabatic wall temperature distributions. This is not to say that the PSP methodology

is invalid, but rather that it quantifies a fundamentally different measurand that is governed by fewer diffusion processes than the surface temperature, and is valid for determining coolant distributions and possibly for the comparison between film cooling schemes—especially with engine hardware where the uncertainties due to model conduction precludes the use of a thermal method. As applied to Department of Defense initiatives, this work is significant in that it provides information to improve room temperature—and low cost—gas turbine film cooling experimentation, which would ultimately result in the improvement of fielded turbomachines by increasing their performance, either with greater specific power output from elevated operating temperatures, or through the increase in machine life.

5.3 Recommendations for Future Work

There are multiple directions that future research can stem from this work. First and foremost, a similar study of coolant flow rate parameters conducted on a flat plate with axial coolant injection could isolate the influence of ACR on the adiabatic effectiveness as determined from thermal measurements. ACR effects could be isolated since the coolant jet dynamics with axial injection are not momentum dominated like the compound angled injection on a leading edge. Furthermore, by including a PSP complement, better understanding of the influence of ReR could be obtained.

The second study could be conducted either on a flat plate or with the leading edge model wherein the freestream and coolant temperatures are carefully controlled to tailor the coolant and freestream properties—or their ratios—in order to isolate their effects on the cooling behavior. Ideally, this would be accomplished with both PSP and thermal methods so as to investigate the influence of the various gas properties on the coolant distribution, as well as on the thermal influence of the jet. Such study would require a PSP compatible foam model, ensuring better

coolant temperature control that was afforded with the Corian leading edge. In addition to selectively matching coolant-to-freestream property ratios, selection of various coolant and freestream conditions could provide a wider variety of ACR values at matched I conditions and the influence of ACR could be further characterized with the IR method.

Finally, overall effectiveness measurements with foreign cooling gases would provide indication of whether the scaling attributes of I and ACR are applicable to scaling the effects of surface conduction, and whether the cooling gas properties have an influence on the cooling effect provided by coolant flow through the internal model geometry.

References

[1] Greiner, N.J., Polanka, M.D., and Rutledge, J.L., 2015, "Scaling of Film Cooling Performance from Ambient to Engine Temperatures," *Journal of Turbomachinery*, **137**(7), 071007.

[2] Bogard, D.G. and Thole, K.A., 2006, "Gas Turbine Film Cooling," *Journal of Propulsion and Power*, **22**(2), pp. 249-270.

[3] Rutledge, J.L., King, P.I., and Rivir, R.B., 2012, "Influence of Film Cooling Unsteadiness on Turbine Blade Leading Edge Heat Flux," *Journal of Engineering for Gas Turbines and Power*, **134**(7), 071901.

[4] Pietrzyk, J.R., Bogard, D.G. and Crawford, M.E., 1990, "Effects of Density Ratio on the Hydrodynamics of Film Cooling," *Journal of Turbomachinery*, **112**(3), pp. 437-443.

[5] Baldauf, S., Schulz, A., Wittig, S., 2001, "High-Resolution Measurements of Local Effectiveness From Discrete Hole Film Cooling," *Journal of Turbomachinery*, **123**(4), pp. 758-765.

[6] Rutledge, J.L., King, P.I., and Rivir, R., 2010, "Time Averaged Net Heat Flux Reduction for Unsteady Film Cooling," *Journal of Engineering for Gas Turbines and Power*, **132**(12), 121901.

[7] Williams, R.P., Dyson, T.E., Bogard, D.G., and Bradshaw, S.D., 2014, "Sensitivity of the Overall Effectiveness to Film Cooling and Internal Cooling on a Turbine Vane Suction Side," *Journal of Turbomachinery*, **136**(3), 031006.

[8] Sinha, A. K., Bogard, D. G., and Crawford, M. E., 1991, "Film Cooling Downstream of a Single Row of Holes With Variable Density Ratio," *Journal of Turbomachinery*, **113**(3), pp. 442–449.

[9] Ekkad, S.V., Han, J.C., and Du, H., 1998, "Detailed Film Cooling Measurements on a Cylindrical Leading Edge Model: Effect of Free-Stream Turbulence and Coolant Density," *Journal of Turbomachinery*, **120**(4), pp. 799-807.

[10] Ekkad, S.V., Ou, S., and Rivir, R.B., 2004, "A Transient Infrared Thermography Method for Simultaneous Film Cooling Effectiveness and Heat Transfer Coefficient Measurements from a Single Test," *Journal of Turbomachinery*, **126**(4), pp. 597-603.

[11] Goldstein, R.J. and Cho, H.H., 1995, "A Review of Mass Transfer Measurements Using Naphthalene Sublimation," *Experimental Thermal and Fluid Science*, **10**(4), pp. 416-343.

[12] Ammari, H. D., Hay, N., and Lampard, D., 1990, "The Effect of Density Ratio on the Heat Transfer From a Film-Cooled Flat Plate," *Journal of Turbomachinery*, **112**(3) pp. 444–450.

[13] Pedersen, D.R., Eckert, E.R.G, and Goldstein, R.J., 1997, "Film Cooling With Large Density Differences Between the Mainstream and the Secondary Fluid Measured by the Heat-Mass Transfer Analogy," *Journal of Heat Transfer*, **99**(4), pp. 620-627.

[14] Li, S.J., Yang, S.F., and Han, J.C., 2014, "Effect of Coolant Density on Leading Edge Showerhead Film Cooling Using the Pressure Sensitive Paint Measurement Technique," *Journal of Turbomachinery*, **136**(5), 051011.

[15] Narzary, D. P., Liu, K. C., Rallabandi, A. P., and Han, J. C., 2012, "Influence of Coolant Density on Turbine Blade Film-Cooling Using Pressure Sensitive Paint Technique," *Journal of Turbomachinery*, **134**(3), 031006.

[16] Crafton, J., Fonov, S. Forlines, R, and Palluconi, S., 2013, "Development of Pressure-Sensitive Paint Systems for Low Speed Flows and Large Wind Tunnels," *Fifty First AIAA Aerospace Sciences Meeting including the New Horizons Forum and Aerospace Exposition*, AIAA, Dallas, TX.

[17] Rutledge, J.L, and Polanka, M.D., 2014, "Computational Fluid Dynamics Evaluations of Unconventional Film Cooling Scaling Parameters on a Simulated Turbine Blade Leading Edge," *Journal of Turbomachinery*, **136**(10), 101006.

[18] Thole, K.A., Sinha, A.K., Bogard, D.G., and Crawford, M.E., 1992 , "Mean Temperature Measurements of Jets With a Crossflow for Gas Turbine Film Cooling Application," Proceedings of the Third International Symposium on Transport Phenomena and Dynamics of Rotating Machinery, ISROMAC-3, pp. 69-85.

[19] Albert, J.E. and Bogard, D.G., 2013, "Measurements of Adiabatic Film and Overall Cooling Effectiveness on a Turbine Vane Pressure Side With a Trench," *Journal of Turbomachinery* **135**(5), 051007.

[20] Bird, R.B., Stewart, W.E., and Lightfoot, E.N., 1960, *Transport Phenomena*, Wiley, New York, pp. 510-512, Chap. 16.

[21] Shadid, J.N. and Eckert, E.R.G., 1991, "The Mass Transfer Analogy to Heat Transfer in Fluids With Temperature-Dependent Properties," *Journal of Turbomachinery*, **113**(1), pp. 27-33.

[22] Kays, W., Crawford, M., and Weigand, B., 2004, *Convective Heat and Mass Transfer*, 4th ed., McGraw-Hill, Chaps. 18-20.

[23] Jones, T.V., 1999, "Theory for the Use of Foreign Gas in Simulating Film Cooling," *International Journal of Heat and Fluid Flow*, **20**(3), pp. 349-354.

[24] Eckert, E.R.G., Sakamoto, H., and Simon, T.W., 2001, "The Heat/Mass Transfer Analogy Factor, Nu/Sh, for Boundary Layers on Turbine Blade Profiles," *International Journal of Heat and Mass Transfer*, **44**(6), pp. 1223-1233.

[25] Rutledge, J.L., 2009, "Pulsed Film Cooling on a Turbine Blade Leading Edge," Ph.D. dissertation, Department of Aeronautics and Astronautics, Air Force Institute of Technology, Wright-Patterson AFB, OH.

[26] Touloukian, Y. S., Saxena, S. C., and Hestermans, P., 1970, *Thermophysical Properties of Matter*, **11**: *Viscosity. Nonmetallic Gases and Liquids*, IFI/Plenum, New York.

[27] Touloukian, Y. S., and Makita, T., 1970, *Thermophysical Properties of Matter*, **6**: *Specific Heat. Nonmetallic Gases and Liquids*, IFI/Plenum, New York.

[28] Touloukian, Y. S., Liley, P. E., and Saxena, S. C., 1970, *Thermophysical Properties of Matter*, **3**: *Thermal Conductivity. Nonmetallic Gases and Liquids*, IFI/Plenum, New York.

[29] Han, J.C. and Rallabandi, A.P., 2010, "Turbine Blade Film Cooling Using PSP Technique," *Frontiers in Heat and Mass Transfer*, **1**(1), 013001.

[30] Han, B., Goldstein, R.J., and Choi, H.G., 2002, "Energy Separation in Shear Layers," *International Journal of Heat and Mass Transfer*, **45**(1), pp. 47-55.

[31] Takahama, H., and Yokosawa, H., 1981, "Energy Separation in Vortex Tubes with a Divergent Chamber," *Journal of Heat Transfer*, **103**(2), pp. 196-203.

[32] Vincenti, W.G., Kruger, C.H., 1965, *Introduction to Physical Gas Dynamics*, Krieger, Malabar, Florida.

[33] Kline, S.J., and McClintock, F.A., 1953, "Describing Uncertainties in Single-Sample Experiments," *Mechanical Engineering*, **75**(1), pp. 3-8.

REPORT DOCUMENTATION PAGE

Form Approved
OMB No. 074-0188

1. REPORT DATE *(DD-MM-YYYY)*	**2. REPORT TYPE**	**3. DATES COVERED** *(From – To)*
24-03-2016	Master's Thesis	January 2015 – March 2016

TITLE AND SUBTITLE

Influence of Coolant Flow Rate Parameters in Scaling Gas Turbine Cooling Effectiveness

5a. CONTRACT NUMBER

5b. GRANT NUMBER

5c. PROGRAM ELEMENT NUMBER

6. AUTHOR(S)

Wiese, Connor J., Second Lieutenant, USAF

5d. PROJECT NUMBER

5e. TASK NUMBER

5f. WORK UNIT NUMBER

7. PERFORMING ORGANIZATION NAMES(S) AND ADDRESS(S)
Air Force Institute of Technology
Graduate School of Engineering and Management (AFIT/ENY)
2950 Hobson Way, Building 640
WPAFB OH 45433-8865

8. PERFORMING ORGANIZATION REPORT NUMBER

AFIT-ENY-MS-16-M-245

9. SPONSORING/MONITORING AGENCY NAME(S) AND ADDRESS(ES)
Air Force Research Lab, Turbine Engine Division, Turbomachinery Branch
Dr. Richard J. Anthony
1950 5th St
Wright Patterson AFB, OH 45433
(937) 255-0570
richard.anthony.4@us.af.mil

10. SPONSOR/MONITOR'S ACRONYM(S)
AFRL/RQTT

11. SPONSOR/MONITOR'S REPORT NUMBER(S)

12. DISTRIBUTION/AVAILABILITY STATEMENT
DISTRUBTION STATEMENT A. APPROVED FOR PUBLIC RELEASE; DISTRIBUTION UNLIMITED.

13. SUPPLEMENTARY NOTES
This material is declared a work of the U.S. Government and is not subject to copyright protection in the United States.

14. ABSTRACT
Rather than replicating engine temperature conditions, film cooling experiments often take place at room temperature. As a result, the fluid properties as well as coolant flow rate parameters cannot be simultaneously matched between the laboratory and the engine. The influence of various coolant flow rate parameters were evaluated for a simulated leading edge at Re = 60K. Both infrared thermography and pressure sensitive paint were used to evaluate the cooling flows of air, argon, carbon dioxide, and nitrogen. The momentum flux ratio was found to best scale the location and shape of the coolant effectiveness profile, while the advective capacity ratio scaled the effectiveness magnitude in thermal experiments. Furthermore, pressure sensitive paints were found to be insufficient one-to-one replacements for the thermal method.

15. SUBJECT TERMS
Film Cooling, Scaling, Pressure Sensitive Paint

16. SECURITY CLASSIFICATION OF:			**17. LIMITATION OF ABSTRACT**	**18. NUMBER OF PAGES**	**19a. NAME OF RESPONSIBLE PERSON**
a. REPORT	**b. ABSTRACT**	**c. THIS PAGE**			James L. Rutledge, AFIT/ENY
U	**U**	**U**	**UU**	141	**19b. TELEPHONE NUMBER** *(Include area code)* (937) 255-6565, ext 4734 (james.rutledge@afit.edu)